Synthesis and Characterization of Nitrogen-Doped Titanium Oxide Nanoparticles for Visible-Light Photocatalytic Wastewater Treatment

by

Mohammad Ali Pelaschi
M.Sc., Sharif University of Technology, 2011
B.Sc., Sharif University of Technology, 2008

A Dissertation Submitted in Partial Fulfillment
of the Requirements for the Degree of

DOCTOR OF PHILOSOPHY

in the Department of Mechanical Engineering

Supervisory Committee

Synthesis and Characterization of Nitrogen-Doped Titanium Oxide Nanoparticles for Visible-light Photocatalytic Wastewater Treatment

by

Mohammad Ali Pelaschi
M.Sc., Sharif University of Technology, 2011
B.Sc., Sharif University of Technology, 2008

Supervisory Committee

Dr. Martin B. G. Jun, Department of Mechanical Engineering
Co-Supervisor

Dr. Frank C.J.M. van Veggel, Department of Chemistry
Co-Supervisor

Dr. Rustom Bhiladvala, Department of Mechanical Engineering
Departmental Member

Dr. Peter Wan, Department of Chemistry
Outside Member

Abstract

Supervisory Committee
Dr. Martin B. G. Jun, Department of Mechanical Engineering
Supervisor
Dr. Frank C.J.M. van Veggel, Department of Chemistry
Co-Supervisor
Dr. Rustom Bhiladvala, Department of Mechanical Engineering
Departmental Member
Dr. Peter Wan, Department of Chemistry
Outside Member

TiO_2 nanoparticles are one of the most suitable materials for photocatalysis, specifically for water and air treatment and removal of a wide variety of organic pollutants such as dyes, aromatic compounds, and chlorinated aromatic compounds. Methods of synthesis of TiO_2 are generally categorized in two main classes of wet chemical, and dry methods. Wet chemical methods generally provide a better control over size, size distribution, and shape; all of which significantly affect photocatalytic performance of the produced nanoparticles. Despite its advantages over other semiconductor photocatalysts, wide band-gap of titania restrains its photocatalytic activity to only UV light, which only makes up to 5% of the light reaching surface of the earth. To induce visible-light activity, titania has been doped by different dopants, including transition metal-dopants such as Fe, and Co and non-metal dopants such as N, and C. Nitrogen has been shown to be a better dopant, providing a suitably placed energy state within the band-gap of TiO_2, and not suffering from issues related to transition-metal dopants such as low thermal and physical stability and high electron-hole recombination rates. To dope titania with nitrogen, one could add the nitrogen source together with other precursors during synthesis, referred to as wet chemical doping

methods, or anneal the synthesized titania nanoparticles under a flow of ammonia at high temperatures, referred to as dry doping methods. While different doping methods have been studied individually, the author maintains that there has been an absence of research comparing the effectiveness of these methods, on photocatalytic performance of *N*-doped TiO_2 within a consistent experiment. In this research TiO_2 nanoparticles were synthesized by a facile, inexpensive sol-gel method, and doping was done by wet chemical methods, dry methods, and a combination of both these methods. Visible-light photocatalytic activity of these nanoparticles was evaluated by their efficiency in degradation of methyl orange. The results show wet doping methods increase the efficiency of titania nanoparticles more than dry doping, or combination of both. Further investigation showed that the main reason for higher activity of wet chemically doped nanoparticles is due to their higher available surface area of 131.7 $m^2.g^{-1}$. After normalizing the available surface area, measured by the BET method, it was shown that a combination of wet chemical doping, and dry doping at 600 °C result in the most active nanoparticles, but high temperature dry doping severely decreases the surface area, lowering the overall efficiency of the product. Additionally, *N*-doped TiO_2 nanoparticles were synthesized using a simple hydrothermal method, in which the nitrogen source was used not only to dope, but also to control shape, size, size distribution, and morphology of the titania nanoparticles, and to induce aqueous colloidal stability. It was shown that addition of triethylamine during the synthesis, results in ultra-small, colloidally stable, cubic TiO_2 nanoparticles, while using triethanolamine results in formation of TiO_2 pallets, assembled into spherical, rose-like structures. The synthesized nanoparticles show impressive efficiency in visible-light removal of phenol, 4-chlorophenol, and pentachlorophenol,

achieving 100% degradation of a 100-ppm phenol solution in 90 min, more than 98% degradation of a 20-ppm 4-chlorophenol solution in 90 min, and 97% degradation of a 10-ppm pentachlorophenol in 180 min with 500 ppm loading of the catalyst in all cases. Moreover, synthesized nanoparticles showed no sign of deactivation after 5 consecutive runs, removing 4-chlorophenol, showing their reusability.

Table of Contents

List of Tables

List of Figures

Acknowledgments

I would like to express my sincere gratitude and appreciation to my supervisors Drs. Martin B.G. Jun and Frank C.J.M. van Veggel for all their help, support, insight, and precious lessons throughout my studies.

I would also like to thank my dear wife, Zahra Naeimi, whose presence, advice, and companionship has helped me through numerous difficulties.

I want to thank my friends Dr. Vahid Moradi and Dr. Ahmad Esmailirad for their advice and help, which has assisted me to overcome challenges regarding my research, but also for their camaraderie when facing difficulties.

Dedication

To my best fiend, the love of my life, my dearest Zahra: I owe it all to you. Without you none of this was possible. I cannot thank you enough.

To my precious baby girl, Ava: I hope my work inspires you and helps you reach your dreams. Your presence in our lives is the best thing that has happened to us.

Chapter 1: Introduction

1.1. Research Motivation

Currently, the development of the global industry is facing a strong challenge regarding production, and release of immense amounts of pollutants in waste water. Both air and water quality of metropolitan and industrial areas have declined severely. Enormous amounts of CO_2 are released into the earth's atmosphere and lots of toxic chemicals have found their way into our water sources.

Overcoming these challenges have been the focus of numerous studies and many solutions have been proposed. Amongst these solutions, photocatalysis has gained considerable attention. Employing the abundant, clean and sustainable energy of the sun, combined with use of photocatalyst materials, researchers have been able to eliminate many harmful compounds, polluting either air, water, or soil. Aside from having no reliance on another energy source except sunlight, another advantage of photocatalytic degradation of pollutants is the photocatalyst itself, which will not be consumed during the mentioned process.

Another advantage of photocatalysis is its non-selectivity and the ability to eliminate chemicals like chlorinated phenols, which could not be readily removed from water using conventional waste water treatment methods, specifically at lower concentrations. During photocatalysis, organic molecules are oxidized into smaller molecules, and eventually to CO_2 and H_2O. However, use of visible-light photocatalysis is not free of difficulties. Firstly, the photocatalyst should be able to perform under visible-light illumination, secondly, it should be physically and chemically stable, and finally, it should have enough chemical potential to be able to oxidize pollutant molecules.

Among different photocatalyst materials, TiO_2 has been the center of attention by researchers. It has been widely engineered for its different applications such as photocatalysis, self-cleaning glasses, and anti-fog coatings; but mostly TiO_2 has been investigated for environmental and energy purposes [1]. Moreover, it has been described as the most practical photocatalyst, which is due to its high chemical and physical stability, biocompatibility and its abundant resources [2]. It is reusable, does not degrade in harsh physical and chemical conditions, and is biocompatible and safe for the environment [3].

Titanium dioxide has a large band-gap, and suitable positioning of conduction band (CB), and valence band (VB) relative to other semiconductors, which makes it a potent oxidizer, and an appropriate compound for wastewater treatment [4, 5]. Other applications of TiO_2 include solar fuel generation[6, 7], photo disinfection [8, 9], self-cleaning glasses [10, 11], super-hydrophilic coatings [12] and water splitting [13].

Large band-gap of TiO_2 is considered beneficial, due to production of high energy photo-induced electron-hole pairs; however, a large band-gap in semiconductors means high energy photons are needed to excite electrons and create electron-hole pairs. For TiO_2, the band-gap energy is 3.2 eV; therefore, only photons with a wavelength shorter than 387 nm, can cause photo-excitation. Meaning, only photons in UV region could excite the electrons into the conduction band of TiO_2, which is specifically unfavourable for photocatalytic applications of TiO_2, because only about three percent of sunlight that reaches the surface of the earth is UV light [2, 3].

To enhance the efficiency of any photocatalyst, one needs to increase the number of photo-excited electrons, and prolong the life of excited electron-hole pairs by decreasing recombination [2]. In case of TiO_2, this could be done in a few general categories:

1. Visible-light excitation: the purpose of such work is to enable electron excitation by lower energy (specifically visible-light) photons; which is achieved by modifying the band-gap, creating a mid-gap by means of introducing a state of impurity or sensitization (e.g. doping, and plasmonic or dye sensitization).

2. Size and shape modification: considering the photo-excited electrons migrate to surface, it could be concluded that, more available surface area leads to higher number of excited electrons. Synthesis of nanoparticulate or nanostructured TiO_2 will notably increase surface to volume ratio, thus enhance photocatalytic properties of TiO_2. Moreover, several research articles have shown, that certain facets of TiO_2 have higher activity; knowledge of this phenomenon, has led to an intensive research on TiO_2 nanoparticles with tailored facets.

3. Using hetero-structured systems: TiO_2, coupled with various materials such as WO_3, CuO and even different polymorphs of TiO_2 in some cases has been reported to show enhanced photo-generated properties over bare TiO_2. However, in this case, any disadvantage of the coupled material (e.g. low thermal or chemical stability) could lower the efficiency of the system they are used in.

Doping with transition metals or non-metal dopants has been shown to induce visible-light photo-excitation of titanium dioxide. Dopant atoms create an energy state within the

band-gap of TiO_2, which allows excitation of electrons by photons of visible-light. This allows use of visible-light, as the energy source needed for photocatalysis, to excite electron-hole pairs of sufficient chemical potential, which increases the efficiency of a photocatalytic system using TiO_2 and sunlight.

Transition metals and non-metal dopants have been used to lower the required energy to excite electron-hole pairs in titanium dioxide. Metal dopants generally produce an energy state below the conduction band of TiO_2, while non-metal dopants create an energy state above the valence band. However, low thermal stability and increased charge carrier recombination are the main disadvantages of metal dopants.

Non-metal dopants have been shown to considerably enhance the visible-light activity of TiO_2 nanoparticles. Among these, nitrogen is regarded as the most suitable, due to suitable placement of the step it creates in the band-gap of TiO_2, and proximity of its size to oxygen, which creates less strain when incorporating in the structure. However, when dopant concentration increases, while visible-light absorption and electron-hole formation increases, to maintain charge neutrality, oxygen vacancies start to form within TiO_2. Formation of oxygen vacancies increases electron-hole recombination, lowering effectiveness of the photocatalyst. This means doping initially increases efficiency of a photocatalytic system, but after reaching an optimum, efficiency starts to decrease. Finding this optimum point helps one design an efficient photocatalytic system.

In this research dissertation, different methods of synthesis of *N*-doped TiO_2 nanoparticles were investigated. Synthesized *N*-doped TiO_2 nanoparticles were characterized using different characterization techniques such as electron microscopy, X-ray diffraction, and X-ray photoelectron spectroscopy. Furthermore, effect of

morphology, phase, dopant concentration, and adsorbed species on photocatalytic activity of synthesized nanoparticles were studied by visible-light treatment of aqueous solutions containing dyes, aromatic compounds, and chlorinated aromatic compounds, using the synthesized *N*-doped TiO_2 nanoparticles.

1.2. Dissertation Outline

This dissertaton starts with a brief explanation about motivation of the research, and a short background on how to induce, and improve visible-light photocatalysis in TiO_2, and why is TiO_2 a suitable photocatalyst for water treatment.

Chapter two is a review of previous work done in this field: a more in-depth explanation of relevant theories involved in visible-light photocatalytic wastewater treatment, different synthesis and doping methods of TiO_2, and results obtained by other researchers on degradation of different pollutants in aqueous solutions.

In chapter three, the author introduces a sol-gel synthesis method to produce *N*-doped TiO_2 nanoparticles, with different doping methods, and discusses the effect of doping technique and parameters on physical, and photocatalytic properties of *N*-doped TiO_2. Moreover, degradation of methyl orange dye, using synthesized nanoparticles and visible-light is investigated, changes in degradation efficiency based on synthesis parameters are discussed, and the results are compared to previous work done in this field, using a figure of merit.

Chapter four introduces a new hydrothermal approach towards synthesis of *N*-doped TiO_2 nanoparticles. It discusses the use of different compounds as the nitrogen source, not only for purpose of nitrogen doping and inducing visible-light absorption, but also as a tool to control size and size distribution, shape, and morphology of the synthesized *N*-doped

nanoparticles. A variety of morphologies, including nanocuboids, and flower like structures with nano-pallets of TiO_2 were produced. Finally, the produced *N*-doped TiO_2 were used for degradation of chlorinated phenols, and effect of their properties, and synthesis method on their activity was discussed in depth.

Chapter five is a summary contribution to the field, and possible future work suggested by the author.

1.3. Research contributions

My research is focused on synthesis of *N*-doped TiO_2 nanoparticles and studying effect of synthesis parameters on characteristics of the product, with an emphasis on visible-light photocatalytic properties. The main contributions of the dissertation are:

1. Studying facile, low-cost sol-gel synthesis method to produce *N*-doped TiO_2 using different doping techniques, and finding the optimal method of doping condition, dopant concentration, and synthesis parameters that contribute to highest visible-light photocatalytic efficiency in degradation of methyl orange dye. The author also provides a review of the results obtained by other researchers, compares them to the results presented in this manuscript, and discusses different results obtained by different synthesis parameters.

2. Introduction of a new hydrothermal synthesis method for production of *N*-doped TiO_2 nanoparticles. Using different nitrogen containing compounds as the source, it was shown that precursors could be used not only to control nitrogen content, but also to control morphology, size and size distribution, but above all to improve visible-light photocatalytic activity.

3. Study photocatalytic activity of synthesized *N*-doped TiO_2 nanoparticle on degradation of different pollutant compounds, including dyes, aromatic compounds, and chlorinated aromatic compounds like pentachlorophenol. Photocatalytic results were combined with characterization data to explain in detail the reason(s) for any possible improvements or decline in photocatalytic efficiency. Moreover, deactivation behaviour of highest performing sample on degradation of 4-chlorophenol were studied.

Chapter 2: Literature Review

2.1. Introduction

Titanium dioxide has three main polymorphs: rutile, anatase and brookite [14]. Table 2.1 lists the chemical structural properties of each polymorph. All three polymorphs consist of TiO_6^{2-} octahedral units, the difference being their arrangement through the unit cell. Rutile is the most stable at high temperatures or higher crystallite size, while anatase is more stable at small crystallite sizes (below 20 nm) [14].

Rutile and anatase have tetragonal unit cells, and brookite has orthorhombic structure. It worth mentioning that, there other polymorphs of TiO_2, such as TiO_2 (B), but aside from rutile and anatase, all polymorphs of TiO_2 are metastable and without special synthesis conditions and addition of mineralizers they will not form [14-16].

Table 2.1. Chemical properties of TiO_2 polymorphs [17].

Properties	Rutile	Anatase	Brookite
Crystal Structure	Tetragonal	Tetragonal	Orthorhombic
Lattice constant (Å)	$a = b =$ 4.5936 c = 2.9587	$a = b =$ 3.784 c = 9.515	a = 9.184 b = 5.447 c = 5.154
Molecule per unit cell	2	2	4
Volume/ molecule ($Å^3$)	31.2160	34.061	32.172
Density (g cm^{-1})	4.13	3.79	3.99

Anatase has a bandgap energy of 3.2 eV, while bandgap of rutile is 3.0 eV; which attributes to a decrease in number of photons capable of exciting electrons on anatase, however, several studies have shown, that anatase exhibits higher photocatalytic activity [18]. This phenomenon could be attributed to differences in charge separation and position of valence and conduction bands in anatase and rutile [19].

2.2. Synthesis of TiO_2 nanoparticles

Synthesis methods to produce TiO_2 nanoparticles could be broken down to one of the two main categories: wet chemical methods and gaseous methods. Wet chemical methods include sol-gel, hydrothermal and solvothermal; gaseous methods include chemical or physical vapour deposition, and sputtering [20].

Gaseous methods require high temperature to provide vapour or ions of precursors with great control over flow and temperature but needs complicated technology and consumes great amount of energy. On the other hand, wet chemical methods could be done by remarkably simpler and less expensive instruments since they are feasible at lower temperatures. Good control over size, shape, chemical structure and morphology are other features of wet chemical synthesis methods [14].

Various precursors are being utilized for synthesis of TiO_2 nanoparticles, including $TiCl_4$, TiF_4, titanium tetra-isopropoxide (TTIIP, $Ti(OCH(CH_3)_2)_4$), titanium butoxide, and titanium powder. Figure 2.1. shows the molecular structure of TTIP and titanium butoxide. Since $TiCl_4$ reacts intractably with water, and TiF_4 contains fluorides which are not environmental friendly, recently most of the published work on TiO_2 synthesis have used titanium alkoxides such as TTIP or titanium butoxide [14].

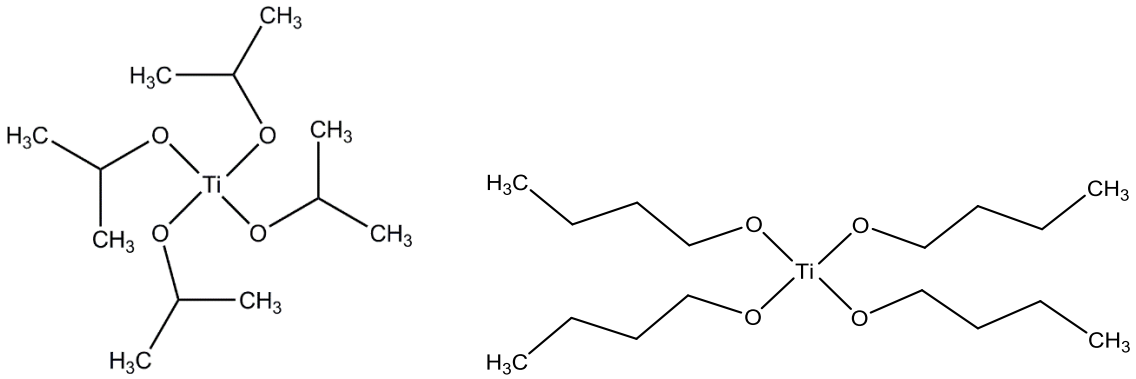

Figure 2.1. Molecular structure of TTIP (left) and titanium butoxide (right)

Controlling the shape of TiO_2 nanoparticles is another method of altering their photo-induced properties. It is shown that various facets of TiO_2 have distinct properties, such as surface energy and distance between constructing elements, which will change titanium dioxide's behaviour towards adsorption and charge separation. A TiO_2 nanocluster grown without any surface modification (i.e. no surfactant or controlling ligand present in synthesis) is comprised of about 97% (101) facets and 3% (001) facets as shown in Figure 2.2. This is due to (001) being the least thermodynamically stable facet, with highest surface energy, and (101) having lowest energy and being the most thermodynamically stable facets.

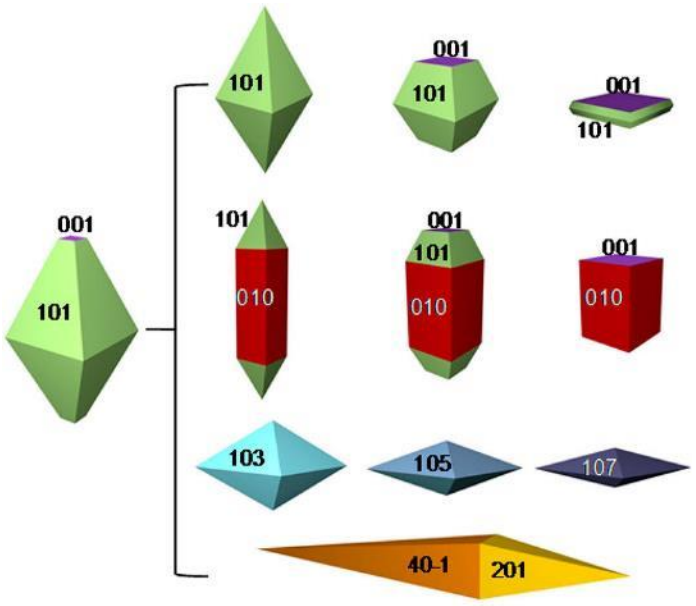

Figure 2.2. various facets of anatase made by alteration of equilibrium morphology [21].

By impeding growth on (001), or promoting growth on other facets, one can change the morphology of anatase nanoparticles as shown in Figure 2.2. For instance, by using a surfactant, which reacts with (001) and (010) facets, and allows growth over (101) facets, a cubic nanoparticle consisted of (010) and (001) facets form [21].

Synthesis of doped and co-doped TiO_2 nanoparticles have been also investigated intensively. Various synthesis methods are modified to alter the product to doped TiO_2. Dopants are usually categorized into two main groups of metals and non-metals. Examples of the former are Fe, Co and Ni, and of the later one can mention N, C and S. This doping process is either done by means of dry or wet processes [2].

Non-metal dopants have shown to enhance photo-induced properties of TiO_2 better than metal dopants. This has been attributed to better position of impurity state within the bandgap of TiO_2, increased charge separation and higher chemical and physical stability [2].

In this chapter several synthesis methods of TiO_2 are discussed, with examples of previous work done about each method, as well as efforts on synthesising doped TiO_2 nanoparticles. As it was mentioned earlier, since anatase shows dominant photocatalytic activity, synthesis and modification methods discussed here are emphasized on anatase.

2.2.1. Sol-gel Method

Over the years, the sol-gel method has been developed from a method only being capable of producing large micron sized particles, to the most feasible, facile and inexpensive approach of making TiO_2 nanoparticles [14]. It has widely been used to synthesize various photocatalysts including TiO_2 and many different variations of doped TiO_2 and $MTiO_3$ nanoparticles and thin films [22, 23].

In a typical sol-gel synthesis, usually a sol is made from TiO_2 precursor, which then forms a network of Ti-O bonds, which is called hydrolysis happen, in which the order depends to several factors including pH, presence of a mineralizer and temperature. These are usually followed by a heat treatment step to calcinate and increase crystallinity.

Upon contact of the titanium precursor with water, several chemical reactions take place, including hydrolysis, oxalation and alcoxolation (equation 2.1., 2.2., and 2.3.) [24], which lead to formation of TiO_2. The synthesis steps are summarized in a flowchart as presented in Figure 2.3.

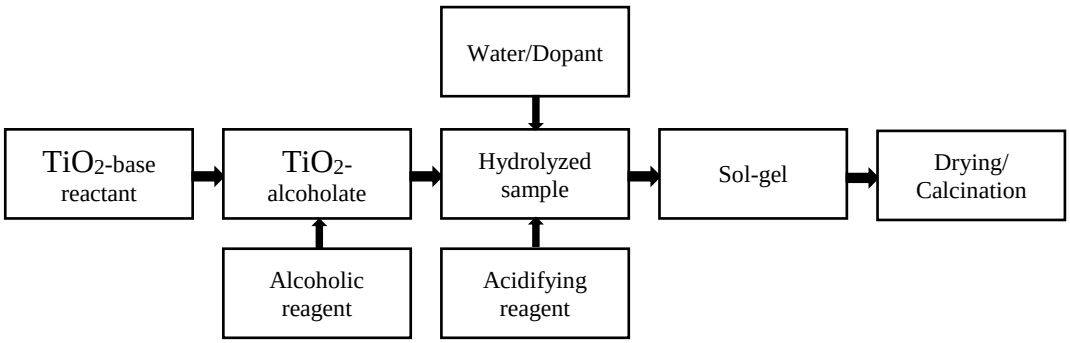

Figure 2.3 TiO_2 sol-gel synthesis steps.

$$Ti\text{-}OR + H_2O \leftrightarrow Ti\text{-}OH + ROH \quad \text{(hydrolysis)} \quad (2.1.)$$

$$Ti\text{-}OH + HO\text{-}Ti \leftrightarrow Ti\text{-}O\text{-}Ti + H_2O \quad \text{(oxalation)} \quad (2.2.)$$

$$Ti\text{-}OR + HO\text{-}Ti \leftrightarrow Ti\text{-}O\text{-}Ti + ROH \quad \text{(alcoxolation)} \quad (2.3.)$$

Altering synthesis conditions, including pH, water to Ti^{4+} ratio, hydrolysis temperature, initial concentration of precursor and calcination temperature will affect the synthesized nanoparticles [23]. It is shown that acidic conditions promote splitting of Ti-OR bonds, and if there is a sufficient ratio of water to Ti, the final products of reactions consist of mostly of Ti-OH groups; on the other hand, with alkaline conditions, condensation takes place at a higher rate, which results in higher content of Ti-O-Ti (oxo) groups [24].

Wang and Ying synthesized TiO_2 nanoparticles via sol-gel method and showed that high water to titanium ratio will result in ultrafine titania nanoparticles by increasing nucleation to growth ratio as shown in Figure 2.4. Calcination at 450 °C resulted in high

crystallinity particles while removing organics from the surface. Acidic pH was shown to lower crystallite size from 20 to 14 nm and narrow the size distribution [25].

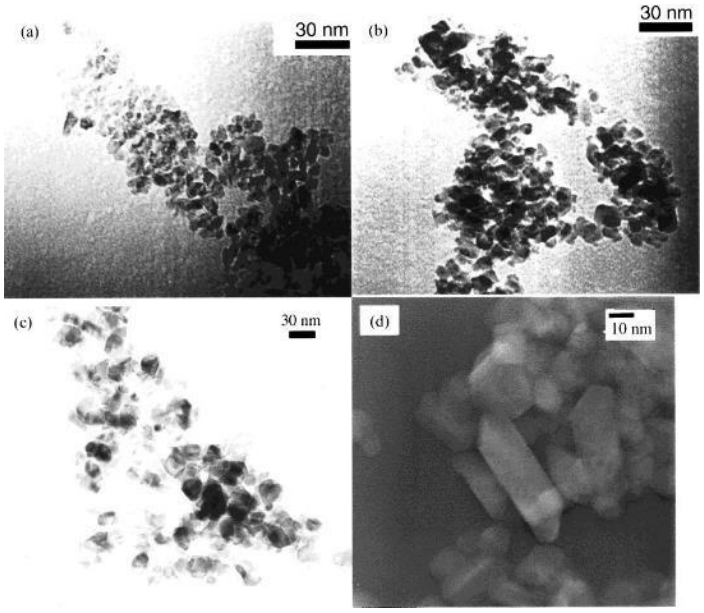

Figure 2.4 sol-gel synthesized nanoparticles of TiO_2 [25].

For a better control over hydrolysis and condensation steps, which would affect the final product, several researchers have tried using complexing ligands to reduce hydrolysis rate. Acetylacetonate, toluenesulfonic acid, myristic acid, ammonia and cetyltrimethylammonium bromide (CTAB) are examples of the mentioned chemicals [14]. Figure 2.5 shows an example of the effect of ammonium hydroxide on sol-gel synthesized TiO_2 nanoparticles.

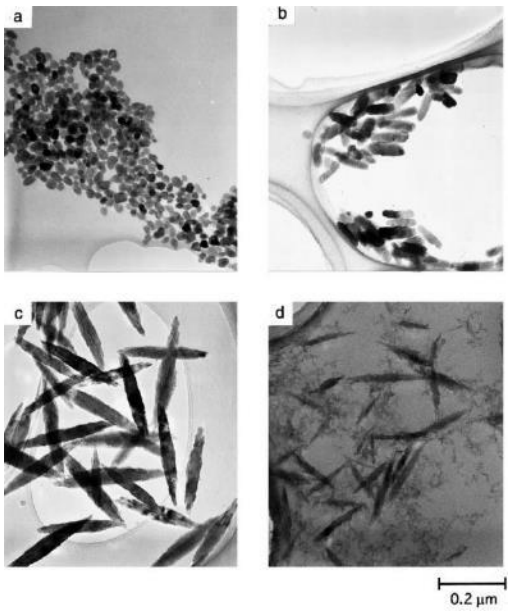

Figure 2.5 effect of ammonium hydroxide on sol-gel synthesized nanoparticles [14].

After discovery of visible-light activity of *N*-doped TiO_2 by Asahi [26], an intensive effort to produce *N*-doped TiO_2 was begun. Several researchers doped TiO_2 with nitrogen by high temperature reaction with an ammonia (NH_3) flow, however high temperature annealing increases particle size and causes severe agglomeration; therefore wet processes were developed to synthesize *N*-doped TiO_2 [2].

In a typical sol-gel synthesis of doped TiO_2, dopant is added to the Ti precursor before the calcination process. In case of *N*-doped TiO_2, ammonium hydroxide (NH_4OH), ammonium chloride (NH_4Cl), hydrazine, urea, guanidine hydrochloride, and triethylamine have been utilized as nitrogen source [2].

Livraghi et al. [27] synthesized *N*-doped TiO_2 nanoparticles by sol-gel method, using TTIP as Ti source, isopropyl alcohol as the medium and ammonium hydroxide as nitrogen source. Wang et al. [28] synthesized *N*-doped TiO_2 nanoparticles by first hydrolysing TTIP, then dissolving the sol in nitric acid, followed by addition of NH_3 to

reach an alkaline pH, which promotes condensation. Calcination at 350 °C to 650 °C produced *N*-doped anatase nanoparticles with sizes from 18 nm to 35 nm.

Jagadale et al. synthesized anatase nanoparticles with a new approach, which eliminates organics before annealing step and therefore allows for lower temperature or shorter time of annealing and reduces the carbon content of the final product [29]. After hydrolysis of TTIP with water, several steps of centrifuging, decantation and addition of DI water, hydrogen peroxide is added to the precipitated sol. The product is a transparent orange complex of peroxo titanate, which after drying at 100 °C and calcination at 300 °C, yields white TiO_2 powder [29]. Author also added ammonium hydroxide to the peroxo complex, which turns to a yellow powder of *N*-doped TiO_2.

2.2.2. Hydrothermal Method

Hydrothermal approach of synthesis provides high crystallinity and small nanoparticles. Since this method does not require a calcination step, it has fewer agglomeration problems (although not entirely dispersible, since there is usually an absent of surfactants).

Synthesis usually involves making titanium hydroxide medium, followed by treatment at temperatures between 150 °C and 250 °C, at high pressures. Factors like temperature, pH, presence of mineralizers and even stirring are reported to change morphology and phase [14].

Chemseddine and Mortiz reported a hydrothermal approach for synthesizing fine anatase nanoparticles in the presence of tetramethylammonium hydroxide as a controller of hydrolysis and condensation. Using tetramethylammonium hydroxide also altered the

growth rates in [101] and [001] crystallographic directions, which in term alters morphology as presented in Figure 2.6 [30].

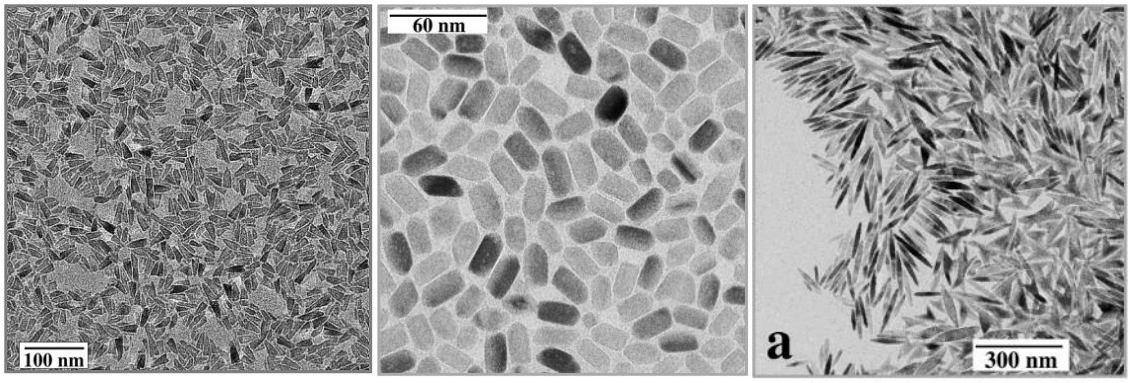

Figure 2.6 altering morphology of anatase by changing synthesis conditions [30].

Introducing NaOH, HF or alkali salts to synthesis medium was also shown to change the morphology. The presence of Na^+ promotes growth of nanotubes, and F^- promotes growth of anatase with cubic or palate morphology [14].

Liu, Yu and Jaroniec synthesized anatase with a variety of morphologies ranging from nanosheets to hollow micro spheres composed of nanosheets by changing the ratio of Cl^- to F^- in the synthesis medium [31].

Yang et al. synthesized anatase nanosheets with 64% (001) exposed facets using HF and 2-propanol, in which 2-propanol acts as both reaction medium and capping agent [32]. The synthesized nanosheets show remarkable photocatalytic activity compared to commercially available TiO_2. In this paper authors proved the adsorption of F on (001) facets by modeling the effect of such adsorption on energies of C and F 1s orbitals, which were coherent with data obtained from XPS.

Using hydrothermal approach to synthesize doped TiO_2 nanoparticles is also frequently attempted by researchers. Wang et al. [33] synthesized *N*-doped TiO_2 nanoparticles via a hydrothermal method using $TiCl_4$ as precursor and L-lysine as nitrogen source; after

annealing at 180 °C for 12 h fine nanoparticles of TiO_2 were produced. Urea, ammonium hydroxide and triethylamine are also utilized for synthesis of *N*-doped TiO_2 nanoparticles using hydrothermal method [2, 34].

2.2.3. Solvothermal Synthesis

Solvothermal synthesis is like hydrothermal method, with difference of using non-aqueous solvent. However, in some cases water is added, to promote and accelerate hydrolysis step. This method allows addition of a wide variety of surfactants and surface ligands, which were not necessarily practical in the hydrothermal method, to direct the growth direction and therefor the morphology of the synthesized nanoparticles [14].

Using organics that react with surface of nanoparticles, dispersibility will enhance dramatically, especially when dispersed in a non-polar solvent, which is a necessity in applications like formation of transparent coatings.

Another advantage of solvothermal synthesis of anatase is refraining from utilizing environmentally harmful compounds such as F^- to control the shape of nanoparticles, and replacing their role with organics such as oleic acid [35]. Dinh et al. reported using oleylamine (OM) and oleic acid (OA) to synthesize highly crystalline anatase nanoparticles with various shapes, as presented in Figure 2.7, by altering Ti:OA:OM ratio and synthesis temperature. Oleic acid slows down growth on (001) facets by binding selectively to these facets, while oleylamine binds to (101) facets and impedes growth on them.

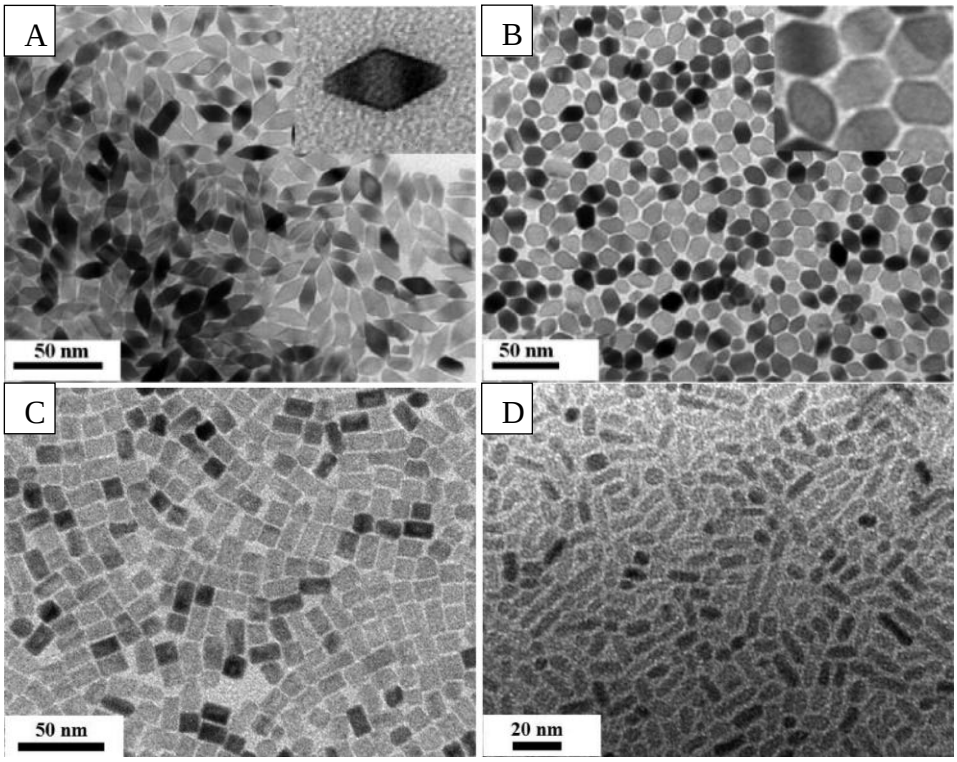

Figure 2.7 controlling morphology of anatase nanoparticles using oleic acid and oleylamine. Ti:OA:OM ratios: A: 1:4:6, B: 1:5:5, C:1:6:4, D: 1:7:3 [35].

2.3. Doping TiO_2 nanoparticles

As mentioned previously, although the relatively large band-gap of TiO_2 is advantageous for many applications, it prevents absorption of visible-light photons, therefore restricting the photocatalytic activity of titania to UV light. This is one of the major drawbacks of using TiO_2 nanoparticles. There has been a lot of effort to extend the absorption of TiO_2 to visible region; amongst them, band-gap engineering has gained more attention recently [7]

Doping with anions (non-metals), cations (metals) and co-doping using both has been investigated. Asahi proposed three possibilities for band-gap engineering of TiO_2 nanoparticles as presented in Figure 2.8 [26]. The band-gap can be modified by doping,

which will either shift the conduction band (CB) lower or the valence band (VB) higher; another possibility would be creation of a state of impurity within the band-gap of TiO_2.

Generally, substitutional doping of transition metals will introduce a lower energy state in the band-gap of TiO_2, which is in coordination with part (a) of Figure 2.8. Various transition metals such as V, Cr, Mn and Fe have been doped into TiO_2 nanoparticles, showing a state between 1.9 - 3 eV below CB. Disadvantageous of transition metal doping are the low thermal stability and the increase of charge carrier recombination in the final products [2].

Doping with anions, will create a state above the VB of TiO_2 and increase visible-light sensitivity. N, F, C, S, P, B and I are some of the examples of investigated anion dopants. It was shown that based on the position of energy states of various anions relative to the VB of TiO_2, N doping would be the best choice to engineer the band-gap of TiO_2. The only anion which would create a better visible-light sensitization is S, however because of its larger size, it wouldn't be doped effectively inside TiO_2 [2, 26, 36].

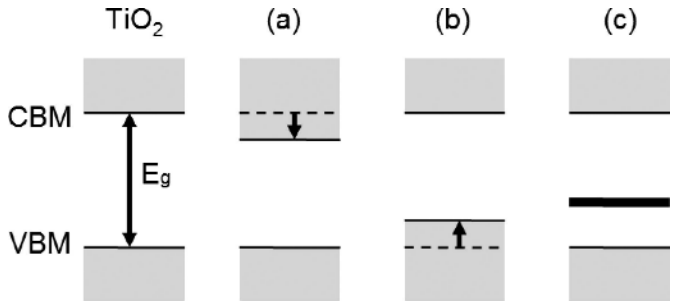

Figure 2.8. band gap modification, a: lower shift of CB, b: higher shift of VB and c: impurity state [2].

2.4. Photocatalytic applications of TiO_2

Photocatalysis and its application in degradation of pollutants is potentially a clean, safe, and environmentally friendly process. Several photocatalysts have been studied by researchers including ZnO, WO_3, CdS and TiO_2. Amongst these materials, TiO_2 has been shown by many studies to be the most suitable candidate because of its high photocatalytic efficiency (~10%), suitable band edge position (Figure 2.9), inertness, abundance, nontoxicity and biocompatibility, and physical and chemical stability [2, 3, 37].

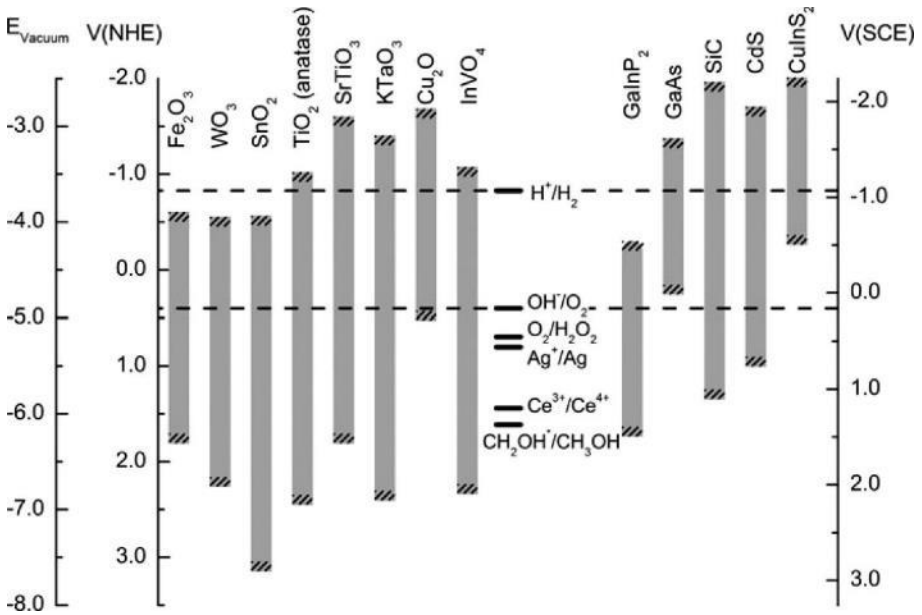

Figure 2.9 band edge position for various photocatalysts vs NHE[1] and SCE[2] [2].

TiO_2 based photocatalytic degradation of pollutants (water/air treatment) has several major advantages including:

4. Contrary to most water/air treatment processes, degradation is not selective, and does not create environmentally hazardous by products;

[1] Normal hydrogen electrode

[2] Standard hydrogen electrode

5. Capable of performing oxidation and reduction reactions simultaneously;
6. High adaptability to various reactor systems;
7. Effective degradation of pollutants with low reactivity (e.g. linear alkanes) or low concentration (ppb range) [38].

Photocatalysis is the process that involves absorption of photons by a molecule or substrate, which produces highly reactive electronically excited states that include electron-hole pairs. Semiconductors have a void energy region within their electronic states, which in contrast to metals, impedes recombination of photo-excited electron-hole pairs. This void energy region which extends from the top of valence band to the bottom of the conduction band is called the band-gap [39]. Photocatalytic activity of TiO_2 is facilitated by creation of photo-generated electron-hole pairs. When a photon with higher energy than the band-gap energy of TiO_2 are able to excite electrons from valance band to conduction band, which leaves a positive hole on the valence band [2].

After photoexcitation, there is a time window of a few nanoseconds for the excited charges, to undergo transfer to adsorbed species. One possible event would be migration of electrons and holes to the surface of semiconductor particle, and their transfer to adsorbed species. This process is more efficient if the species are pre-adsorbed [2, 39, 40]. Upon charge transfer, an electron from the adsorbed specie could combine with the photo-generated hole, resulting in oxidation of electron donor specie, while the photo-generated electron could reduce the adsorbed specie. Aside from reacting with adsorbed species, photo-generated electrons and holes could recombine with each other, either on the surface of the semiconductor (surface recombination) or within it (volume recombination), as presented in Figure 2.10.

In TiO_2, band edge positions (Figure 2.9) are such that the photo-generated holes in the valence band are strong oxidizers capable of oxidizing many organic molecules and splitting water due to their high negative potential (related to NHE[3]). Valence band of TiO_2 is located at a potential of ~2 V relative to the normal hydrogen electrode, which makes it a stronger oxidising agent than MnO_4^-.

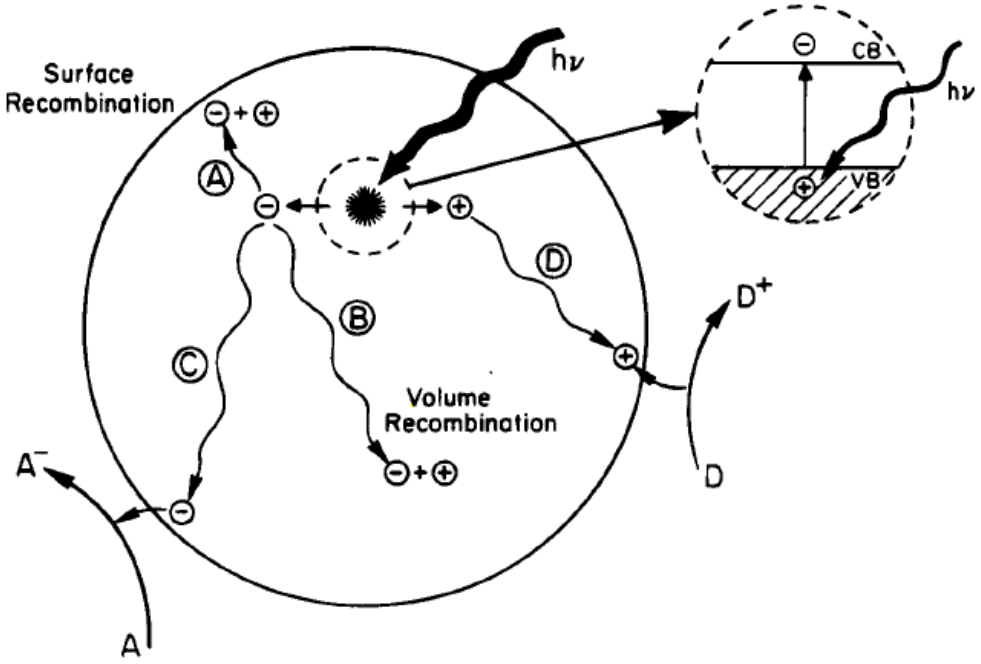

Figure 2.10 photo generation of electrons and holes and de-excitation events [39].

2.5. Mechanism of photocatalytic degradation of organics using semiconductors

There are two explanations proposed to describe the mechanism of photocatalytic degradation (photo mineralization) on the surface of a TiO_2 or any semiconductor in general. First mechanism is based on direct absorption of photo-induced electron-hole pairs to adsorbed organic molecules, which will be reduced by electrons or oxidized by

[3] Normal hydrogen electrode

holes. The other theory predicts oxidation of an OH^- ion by positive holes, which creates hydroxyl radicals. Figure 2.11 shows hydroxyl radical and OH^- ion. Hydroxyl radicals are very reactive and subsequently oxidize organic molecules and become OH^- ions. Further theoretical and empirical studies have been supportive of the second theorem (hydroxyl formation) [39, 41].

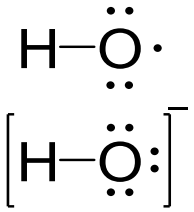

Figure 2.11 Hydroxyl radical and OH^- ion.

Upon adsorption, H_2O molecules react with bridging oxygen atoms of TiO_2 and photo-induced holes, which creates two hydroxyl radicals. In case of hydrocarbons, carbon atom could be oxidized from C^{4-} up to C^{4+}. Table 2.2 shows different oxidation states of carbon in various hydrocarbon structures.

Table 2.2 oxidation states of carbon

Oxidation Number

Carbon's oxidation number	Example	Family of Hydrocarbons
4-	CH_4	
3-	C_2H_6	Alkane
2-	C_2H_4	Alkene
1-	$R\text{-}CH_2OH$	Primary alcohol
0	C_4H_6	Alkyne
1+	R-COH	Aldehyde
2+	R-CO-R'	Ketone
3+	R-COOH	Carboxylic acid
4+	CO_2, CCl_4	

To conserve the electrical neutrality of the whole system, and to eliminate charge buildup, after consumption of holes, photo-induced electrons should react as well. Electron will transfer to oxygen, which is an electron acceptor, making superoxide O_2^- (Figure 2.12) [41].

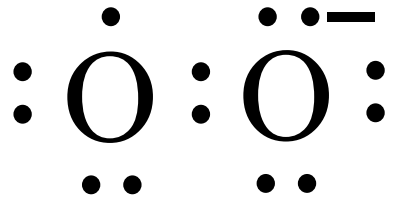

Figure 2.12 Structure of superoxide (O_2^-).

The rate of reaction is controlled by reduction rate of O_2 or H_2O, since several articles have stated that the speed of this step is lower than the oxidation step by photo-induced holes. Proposed possible reactions are presented in equations 2.4 to 2.9 [42]. A schematic of the mentioned chemical reactions on the surface of TiO_2 is shown in Figure 2.13.

$$O_{2(ads)} + e^- \rightarrow O_{2(ads)}^{-\bullet} \quad (2.4)$$

$$O_{2(ads)}^{-\bullet} + e^- \rightarrow O_2^{2-} \quad (2.5)$$

$$O_{2(ads)}^{-\bullet} + H^+ \rightarrow HO_2^{\bullet} \quad (2.6)$$

$$2HO_2^{\bullet} \rightarrow H_2O_2 + O_2 \quad (2.7)$$

$$H_2O_2 + O_2^{-\bullet} \rightarrow 2OH + O_2^- \quad (2.8)$$

$$H_2O_2 + OH^{\bullet} \rightarrow HO_2^{\bullet} + H_2O \quad (2.9)$$

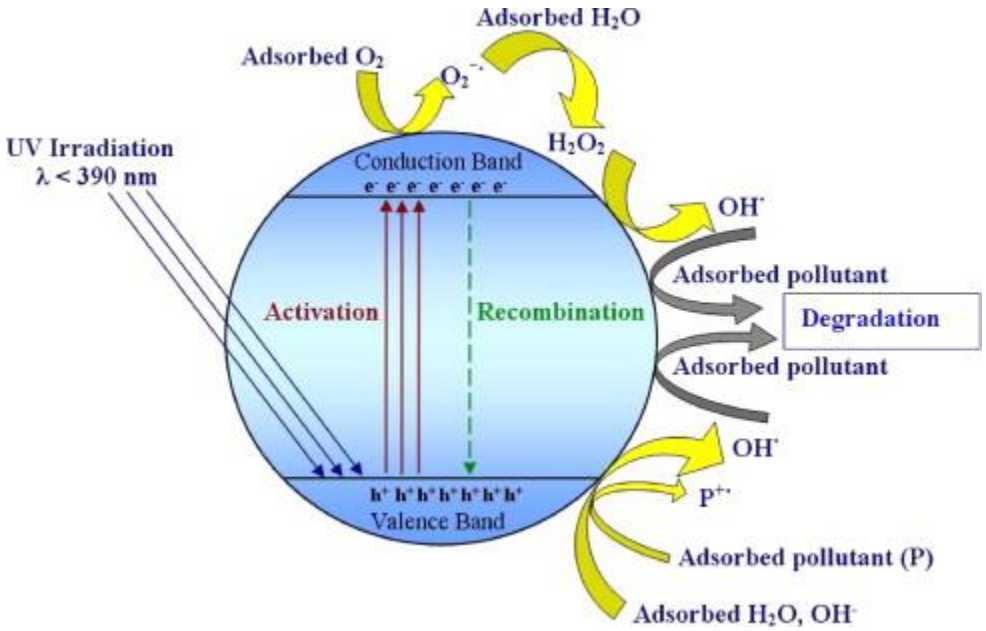

Figure 2.13 Proposed mechanism of photocatalytic activity of TiO_2 [43].

2.6. Review of work on photocatalytic degradation of organic molecules using TiO_2

As mentioned before, extensive research has been done on the photocatalytic degradation of organics using TiO_2. Phenolic compounds are one of the most studied materials in photocatalytic degradation, due to their vast applications in industry and their adverse properties such as being highly toxic, carcinogenic and chemically stable. Another intensively studied compound is methyl orange, which is often used as model dye. Dyes are present in many aspects of our daily life, and in industrial waste water (e.g. textile industry), while being mainly carcinogenic and damaging to environment and wild life [43-46].

Gue et al. studied mechanism of degradation of phenol in aqueous medium using a mixed phase TiO_2 sample with particle size of 20-30 nm and a UV light source. Figure 2.14 shows the proposed mechanism of photo degradation of phenol [45].

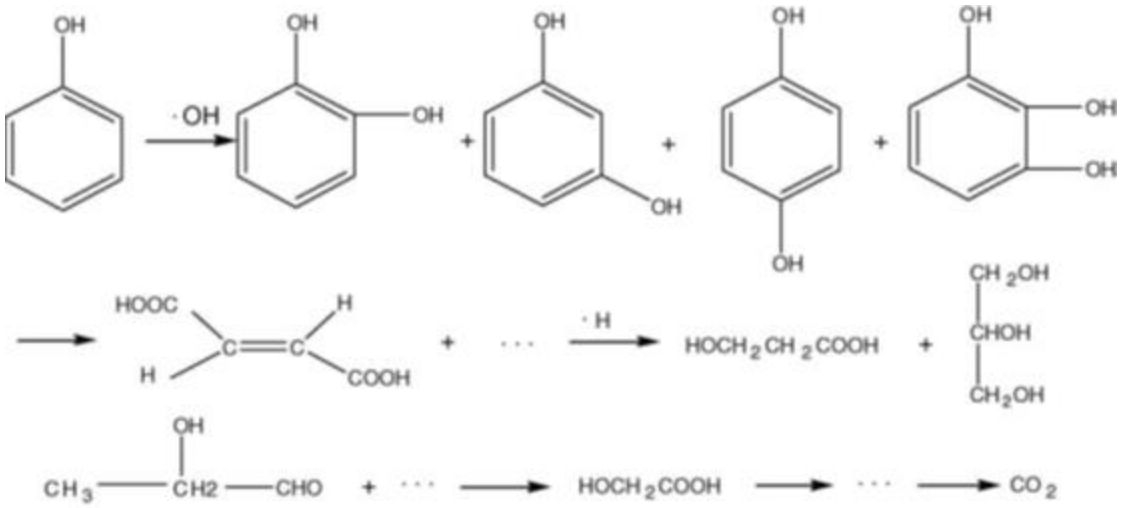

Figure 2.14 Proposed mechanism of photo degradation of phenol using TiO_2 [45].

It was also shown that $H^{\bullet}$ plays an important role in degradation of phenol alongside $OH^{\bullet}$. Several bi-products were detected after 12 hours of reaction under UV light including 2-hydroxy-propaldehyde, hydroxy-acetic acid, 3-hydroxy-propyl acid, glycerol, catechol, (E)-2-butenedioic acid, resorcinol, hydroquinone and 1,2,3-benzenetriol [45].

For degradation of methyl orange, Yu et al. proposed that both the photo-generated electron-hole pairs, and $OH^{\bullet}$ could attribute to degradation process. It was shown that in low concentrations of methyl orange (below 1.6×10^{-4} M), the degradation is mainly due to hydroxyl radicals whereas in higher concentrations, methyl orange is directly oxidized by photo-generated electrons [44].

Lachheb et al. reported photocatalytic degradation of dyes, using TiO_2 under UV light. They reported total mineralization and not only decolourization, which converts the dye molecules to CO_2 and water, and form of sulfate from sulfur and N_2 or ammonium from nitrogen. This process not only decolourizes the dye polluted water, but also makes it detoxified [47].

Rashed et al. studied degradation of methyl using TiO_2 nanoparticles under a 1000 W tungsten halogen light source [48]. The TiO_2 nanoparticles were dispersed in methyl orang aqueous solution. Figure 2.15 shows UV-Vis spectra of methyl orange solution for samples taken on various points in time. The intensity of absorbance peak caused by methyl orange is decreasing over time. Equation 2.10 is used to calculate the percentage of degradation from intensity of absorbance peak.

$$Degradation\ \% = \left[1 - \frac{A_t}{A_0}\right] \times\ 100 \qquad (2.10)$$

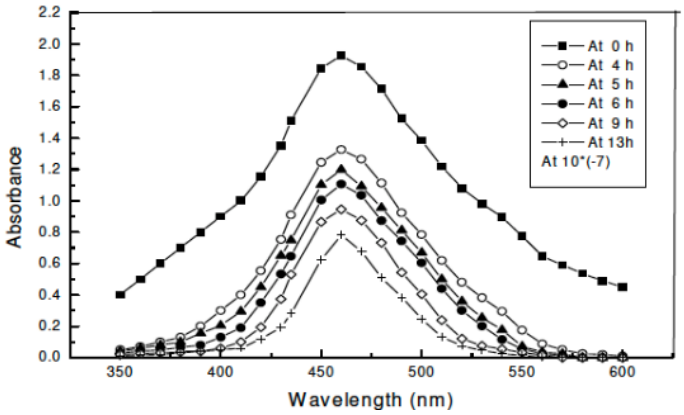

Figure 2.15 Photocatalytic degradation of methyl orange using TiO_2 over time, figure shows absorption spectrum of methyl orange solution after being exposed to light with different durations [48].

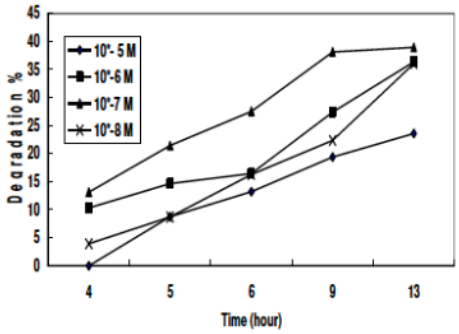

Figure 2.16 Effect of time on degradation percentage of methyl orange.

Yang et al. utilized sol-gel synthesized TiO_2 nanoparticles to degrade methyl orange under a 125 W high pressure mercury lamp. They also investigated the effect of pH and

presence of H_2O_2. Figure 2.17 shows their results, stating that addition of hydrogen peroxide, and decreasing pH increase degradation efficiency [49].

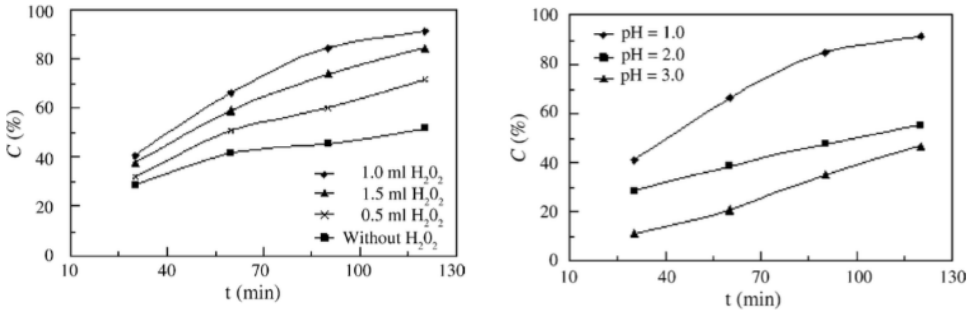

Figure 2.17 Effect of different conditions of photocatalytic degradation of methyl orange left: presence of H_2O_2 and right: pH [49].

2.6.1. Degradation of pollutants using visible-light responsive TiO_2

First non-metal doped visible-light responsive TiO_2 was made by Asahi et al., which reported preparation of $TiO_{2-x}N_x$ films using sputtering method. While under UV light both undoped and doped samples showed similar photocatalytic activity on degradation of methylene blue, *N*-doped samples were shown to be more active when visible-light was used. Figure 2.18 shows light absorption properties of TiO_2 samples and the formation of CO_2 over time, which can be attributed to degradation of methylene blue [26].

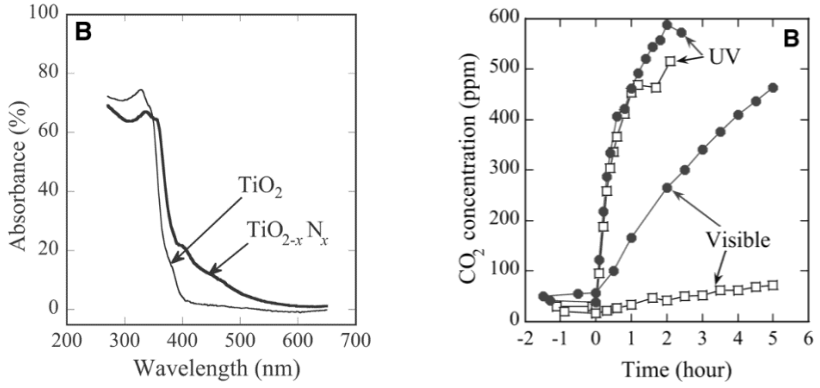

Figure 2.18 Left: absorption properties of TiO_2 vs. $TiO_{2-x}O_x$. Right: formation of CO_2 over time from degradation of methylene blue using TiO_2 (open square) and $TiO_{2-x}O_x$ (solid circles) [26].

After publication of this report, numerous researchers worked on degradation of pollutants using doped TiO_2. While N is still considered the best non-metal dopant [36], other dopants such as B, C, F and S have also been studied. There has also been some research on using two or more dopants on the same sample, which F, N co-doped system was shown to be one of the most beneficial and advantageous doping systems.

Yang et al. used a solvothermal method to synthesize *N*-doped TiO_2 nanoparticles using ethylenediamine as nitrogen source. Figure 2.19 shows the effect of different nitrogen source starting concentration on degradation process (ethylenediamine concentration increases from sample TON-1 to TON-4), which shows there is an optimum for doping and after reaching this point activity decreases [50].

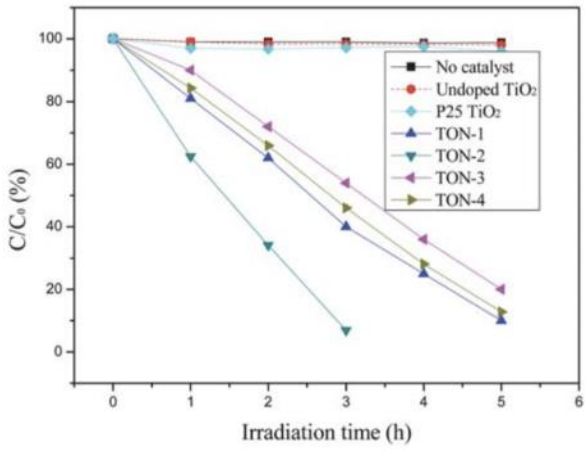

Figure 2.19 degradation percentage of methyl orange using TiO_2 [50].

Chapter 3: The influence of nitrogen doping process on physical properties and visible-light photocatalytic water treatment performance of TiO_2 nanoparticles

3.1. Abstract

N-doped TiO_2 nanoparticles were successfully synthesized using the sol-gel method with different doping techniques such as wet chemical methods, dry methods and a combination of both. Non-ambient X-ray diffraction was performed to study the effect of nitrogen doping on phase and phase transformation of TiO_2. It has been shown that the presence of nitrogen increases the anatase-rutile phase transformation from 530 °C to 635 °C, and at higher annealing temperatures, keeps anatase as the dominant phase. Analysis by X-ray photon-electron spectroscopy and diffuse reflectance UV-Vis spectroscopy pointed out the successful nitrogen doping, while providing the ability to distinguish quantitatively different nitrogen species. Three nitrogen species with binding energies of 396 eV, 400 eV and 402 eV were observed, which are attributed to substitutional N, NO_x and NH_x, and chemisorbed γ-N_2, respectively. Results of visible-light induced photocatalytic degradation of organic pollutant methyl orange was used to study photocatalytic activity of synthesized nanoparticles. The results demonstrate significant improvement of the visible-light-induced photocatalytic activity, as compared with previous studies and the undoped sample, which is caused by narrowing the band-gap energy of TiO_2 and thus extending its absorption window into the visible region. The sample doped by the wet chemical method had the highest photocatalytic activity. Doping by high temperature ammonia, results in higher dopant concentrations; and subsequently increases visible-light absorption, which initially increases photocatalytic

activity. however, due to decrease of surface area at high annealing temperatures, and formation of defects which act as recombination centers, photocatalytic activity decreases by annealing at temperatures more than 500˚C.

3.2. Introduction

Inadequate access to clean water has been a universal problem due to population growth and release of municipal and industrial wastewater into fresh water sources. Pollution, combined with water scarcity, even in areas that previously were presumed water rich, has called for an intensive attention to efficient, low cost, and low energy water treatment research on a global scale [51, 52].

Among different approaches towards water treatment, photocatalysis has gained considerable attention, due to relying only on sunlight as energy source, simultaneous (catalytic) oxidation and reduction and effectiveness of treatment of minute amounts of pollutants, as well as pollutants with low reactivity. Moreover, photocatalysis minimizes the use of chemicals, thus potentially lowering environmental impact [5, 53, 54].

Photocatalytic treatment of water using TiO_2 nanoparticles has been investigated intensively, mainly due to superior physical and chemical properties of TiO_2 as a photocatalyst, compared to other semi-conductors such as large band-gap, and suitable positioning of conduction band (CB) and valence band (VB) that enables degradation of organic, as well as inorganic pollutants [3, 4, 14, 55, 56]. On the other hand, the large bandgap of TiO_2 (3.2 eV) limits its photocatalytic activity window to absorption of wavelengths in the UV region or shorter. only 3% of sunlight reaching the surface of the earth is UV, accordingly for a more effective photocatalyst system, which still employs TiO_2, one should shift the absorption spectrum of TiO_2, and consecutively its

photocatalytic activity region to visible-light, yet have the CB and VB, or sub-bandgap impurity states, still positioned to act as reduction and oxidation sites, respectively [2].

Amongst the polymorphs of TiO_2, anatase has shown to be the better photocatalyst [18]; however, other polymorphs of TiO_2 like rutile and brookite have also shown to be capable photocatalysts [57-60]. Moreover, shape of nanoparticles, which influences their outer facets, affects photocatalytic activity. It has been shown that presence of (001) facets increases the photocatalytic activity of TiO_2 nanoparticles [31, 61].

Doping TiO_2 nanoparticles, or altering its bandgap by creating states of impurity within its bandgap has been one of the main methods utilized to achieve visible-light responsivity [62]. Dopants are mainly divided in two main groups: anions, i.e. non-metals like N, C[63], F[64] and S[65, 66], and metals, i.e. metal cations such as Fe, and Co[67], Cr[68], Mo[69], and V[70]. Each category has a different effect on the bandgap of TiO_2; non-metal dopants create a state above the valence band of TiO_2, while metal dopants generate an energy level below the conduction band of TiO_2, thus, in both cases, making visible-light responsive TiO_2[71-73]. Another possibility for visible-light reactivity by anion doping is band-gap narrowing, caused by alteration of the valence band of TiO_2 towards higher energy levels [74, 75].

The low thermal stability of transition metal doped TiO_2, and the fact that such dopants act as recombination sites of the photo-induced electron-hole pairs, lowering the lifetime of photo-generated electron-hole pairs have shifted the interest to non-metal dopants [76]. Moreover, it has been shown in case of doping with some metals such as Zn, doping can have an adverse effect on the photocatalytic activity of TiO_2 [77].

Asahi et al. have shown that nitrogen has the highest potential for increasing visible-light sensitivity by studying the density of states (DOS) of various doped TiO_2. The reason being suitable positioning of energy levels of nitrogen, between band edges of TiO_2, compared to other anions such as S, F and C [26]. Moreover, proximity of nitrogen's size to oxygen facilitates incorporation of nitrogen in the structure of TiO_2.

Doped TiO_2 nanoparticles have been synthesized by wet chemical methods such as sol-gel [29, 78, 79], hydrothermal [33, 34, 80], solvothermal [81-83], as well as other methods like mechanochemical [84] and chemical vapor deposition [85]. In addition, it has been shown that relative to the method of doping, different nitrogen species such as substitutional and interstitial nitrogen or nitrogen oxide moieties, could exist within the doped TiO_2 [36]; and these different nitrogen species would affect the physical and photo-active properties of doped TiO_2. Doping during the hydrolysis step of wet chemical methods, results mainly in interstitial nitrogen species; while doping during the annealing step in a flow of ammonia gas, or by nitrogen sputtering produces mainly substitutional nitrogen or nitrogen oxide moieties [86-89].

The amount of doped nitrogen in TiO_2 has a conflicting effect on the photocatalytic activity. It has been shown that nitrogen doping would reduce photocatalytic activity under UV light compared to undoped TiO_2 [90-92]. However, under visible-light, while undoped TiO_2 is not active, doped TiO_2 nanoparticles show activity. Visible-light induced photocatalytic activity increases gradually in conjunction with nitrogen content, but after reaching an optimum, starts to decrease [93]. This has been attributed to production of oxygen vacancies to maintain overall charge neutrality when large amounts

of nitrogen are doped into TiO_2. Oxygen vacancies then act as recombination centers lowering photocatalytic activity [2].

So far, various articles have studied *N*-doped TiO_2 nanoparticle, and have investigated the effect of synthesis and nitrogen doping conditions, such as type of precursor on nitrogen species, and resulting photocatalytic activity of synthesized nanoparticles [94-97]. However, diversity of experimental methods, including synthesis and doping conditions, and characterization techniques (especially photocatalytic activity measurements procedures), have made comparison of the results far from straightforward. A good research article on this matter is the work done by Lo Presti et al., who investigated the effect of different dopants on properties of *N*-doped TiO_2. However this article focuses on wet chemical synthesis methods and does not cover other doping methods [98]. Thus, the presence of an article that investigates different doping techniques of TiO_2 nanoparticles, with varying dopant amounts, while utilizing a consistent practice of characterization of synthesized nanoparticles is still desirable and consequently the subject of this work.

I report the effect of wet-chemical synthesis methods of doping TiO_2, using a modified sol-gel technique, as well as doping TiO_2 nanoparticle by high temperature ammonia gas exposure, and a combination of both these techniques. Synthesized *N*-doped TiO_2 nanoparticles were shown to possess different nitrogen species, with varying amounts, based on the doping method and conditions. Doping conditions also altered the crystalline structure and phase of the synthesized *N*-doped TiO_2 nanoparticles. To study the photocatalytic activity of the synthesize nanoparticles, degradation of methyl orange under visible-light was performed. To compare the efficiency of synthesized

nanoparticles to previous work, we place our results in the context of recent results obtained by other researchers with focus on photocatalytic degradation of organic compounds using *N*-doped nanoparticles; the most promising results are presented in Table 3.1. To consider all the significant factors that affect photocatalytic degradation efficiency of different studies, the results obtained by each research group are normalized by means of converting the reported degradation in the articles to figure of merit equation 3.1, according to [99]:

$$FM\ (kW\ h\ m^{-3}) = \frac{P \times t \times 1000}{V \times \log \frac{C_0}{C_f}} \quad (3.1)$$

Where P is the power consumption of the applied light source (kW), t is reaction time (h), V is the volume of treated water (L), C_0 is the initial and C_f is the final concentration of the contaminant. Although this model considers the most influential parameters involved in photocatalytic treatment of pollutants, there remain other factors such as type of the light source, not reflected in the model. However, this model provides a proper tool to compare effectiveness and efficiency of different catalysts and is the common figure of merit in the field.

It is worth mentioning that *N*-doped TiO_2, and TiO_2 in general have a much more diverse spectrum of applications, including photo disinfection, self-cleaning glasses, super hydrophilic coatings and water splitting, which are not discussed in this article [21, 100-103].

Table 3.1. Comparison of previous work on degradation of methyl orange using *N*-doped TiO_2

Synthesis method	Pollutant concentration (ppm)	Catalyst concentration (ppm)	Degradation %	Time (min)	Light source	Power (W)	Filter (nm)	Vol (ml)	Figure of Merit (kW h m^{-3})
Sol-gel[104]	18	2,800	83	240	Hg	450	≥420	350	6,682.9
Sol-gel[105]	20	Thin film	37	300	W halogen	1000	≥420	80	311,473.0
Hydrothermal[33]	15	1,000	45	120	Xe	500	≥400	50	77,030.5
Sol-gel[106]	10	400	60	120	Hg	300	≥400	50	30,155.3
Sol-gel[107]	20	Thin film	60	480	Hg	500	≥400 ≤700	50	201,035.3
Coprecipitation[108]	20	1,000	90	120	Hg	200	≥350 ≤450	100	4,000.0
Hydrothermal[80]	10	1,000	80	120	Xe	1000	≥400	50	57,227.1
Sol-gel[109]	10	4,000	80	360	Hg	125	≥420	30	35,766.9
Coprecipitation[91]	100	1,000	59	240	Xe	450	≥420	20	232,428.3
Sol-gel[92]	10	1,000	68	240	Xe	300	≥400	100	24,249.8
Sol-gel[110]	5	10,000	95	300	W lamp	400		50	30,744.9
Hydrothermal[111]	30	1,000	74	360	Xe	400		10	410,237.7
Sol-gel[112]	6.5	4,000	20	540	Xe	300	400	5	5,572,179.6
Solvothermal[113]	32.7	500	70	45	Xe	500	420	100	7,171.8
Hydrothermal[114]	10	1,000	55	180	W lamp	400	420	100	34,603.3
Hydrothermal[115]	20	100	12	150	Xe	500	400	100	225,154.9
Sol-gel[116]	5	1,000	88	360	W halide	200		200	6,515.9
Hydrothermal oxidation of TiN by H_2O_2[117]	20	100	10	150	Xe	500	400	200	136,589.7
Sol-gel[118]	50	1,000	67	120	Xe	300	400	200	6,230.7

3.3. Experimental Section

Titanium(IV) *iso*propoxide (TTIP) 97% was purchased from Aldrich, hydrogen peroxide, ammonium hydroxide and anhydrous ethanol were purchased from VWR. Anhydrous ammonia gas was purchased from Praxair. Doubly deionized water (DI; >18 MΩ) was used throughout. All materials were used without further purification.

3.3.1. Synthesis of TiO_2 nanoparticles

Pure titanium dioxide (A-TiO_2), and three types of *N*-doped samples were synthesized using a simple sol-gel method. Nitrogen doping was done either during hydrolysis (B-TiO_2), during calcination (C samples) or both during hydrolysis and calcination (D samples).

To synthesize the undoped sample, a 0.5 M solution of TTIP in anhydrous ethanol was made; to this solution was added a 2 M solution of water in ethanol with the same volume under vigorous stirring. The produced sol was aged for 60 min, then was three times washed by DI water. Next, 20 mL of a 50 vol% solution of H_2O_2 in water was added to the sol, forming a clear orange titanium peroxo gel. This gel was aged for 24 h, followed by drying at 80 °C for 12 h and annealing at 350 °C for 4 h.

B-TiO_2 sample was made in accordance to A-TiO_2 samples, but before the drying step, 10 mL of ammonium hydroxide was added to the peroxo, which makes a yellow gel. This gel was then dried at 80 °C for 12 h and was annealed at 350 °C for 4 h.

To make the C samples, the undoped sample, A-TiO_2 was annealed in a tube furnace under a flow of ammonia and argon (60/40 flow ratio), at 400 °C, 500 °C, 600 °C and 700 °C for 1 h. The D samples were made with the same procedure using B-TiO_2 nanoparticles, then was annealed under a flow of ammonia and argon (60/40 flow ratio), at 400 °C, 500 °C, 600 °C and 700 °C. The flow was set to desired ratio

using a flow meter. Table 3.2 shows the list of synthesized TiO_2 nanoparticles and their synthesis conditions regarding nitrogen doping.

Table 3.2. List of synthesized TiO_2 samples

Sample Name	Doping Method	Ammonia presence at hydrolysis	Ammonia exposure temperature (°C)
A-TiO_2	Undoped	No	NA
B-TiO_2	During hydrolysis	Yes	NA
C400	During calcination	NO	400
C500		NO	500
C600		NO	600
C700		NO	700
D400	During hydrolysis and calcination	Yes	400
D500		Yes	500
D600		Yes	600
D700		Yes	700

3.3.2. Characterization of synthesized nanoparticles

X-ray powder diffraction (XRD) was performed using a PANalytical Empyrean X-ray diffractometer with copper-based X-ray source, operating at 45 kV and 40 mA and the analysis was done using HighScore Plus 4.1. Hitachi HF-3300V scanning transmission electron holography microscope (STEHM) was utilized in scanning electron microscopy (SEM) imaging, and transmission electron microscopy (TEM) mode to observe size, shape and morphology of synthesized nanoparticles. Lambda 1050 ultraviolet-visible (UV-vis) spectrometer with integrating sphere accessory was used to perform diffuse reflectance measurements for characterizing light absorption properties of the synthesized nanoparticles. Cary 100 UV-Vis spectrometer was utilized to observe the absorption spectra of pollutant solutions. Perkin Elmer Spectrum One FT-IR was utilized to investigate the presence of organic species on the surface of synthesized nanoparticles. Omicron & Leybold MAX200 X-ray Photo-electron Spectrometer (XPS) was used to measure elemental binding energies, which

is used to find the type of nitrogen species, present on the surface. To fit the XPS data, XPSPeak 4.1 software was used. The background for each sample was determined by the Shirely method [119]. Origin 9.1.0 was used to analyze the data and for graphing. To measure surface area, a Quantachrome Autosorb-1, Brunauer, Emmett and Teller Instrument (BET) instrument was utilized, using nitrogen as the adsorbing gas. After drawing the BET adsorption plot, the volume of the adsorbed monolayer was calculated from equation 3.2.

$$V_m = \frac{1}{M + I} \quad (3.2)$$

Where M is the slope and I is the intercept of the BET plot. Surface area of the sample was calculated using equation 3.3.

$$S = \frac{V_m . N . a}{V . m} \quad (3.3)$$

Where N is Avogadro's number (6.022 x 10^{23} mol^{-1}), a is the cross section of the adsorbate (0.162 nm in this case), V is the volume of 1 mol of adsorbate gas at standard temperature and pressure (24,000 mL mol^{-1}), and m is the mass of the sample used for the measurement in grams [120].

3.3.3. Photocatalytic activity measurement

The degradation of methyl orange under visible-light was used to observe the photocatalytic activity of the synthesized nanoparticles. A Cermax PE300BUV Xenon arc lamp (300 W) was used as the light source, which was placed 10 cm above the samples. A UV cut off filter was utilized with a band pass of 400 nm. For all experiments, a 200 mL solution of methyl orange in DI water with concentration of 20 mg L^{-1} was used; to which 0.2 g of catalyst was added. All samples were stirred with a magnetic stirrer for 15 min with no light to reach adsorption−desorption equilibrium. Several samples where then taken periodically after the light source was

turned on, followed by filtering through a 0.2 μm membrane filter. These samples were analyzed with UV-Vis spectrometer to find out the concentration change of methyl orange (see SI), relative to the initial solution in each period.

3.4. Results and Discussion

Figure 3.1 shows images of the synthesized powders. Undoped sample, A-TiO_2, is white, while the sample that is doped during hydrolysis step by addition of ammonium hydroxide to the sol, B-TiO_2, has a yellow color. Annealing the undoped sample under ammonia exposure (C samples), results in a yellow powder at 400 °C, green powder at 500 °C and 600 °C and a black powder at 700 °C. Annealing B-TiO_2 sample under ammonia exposure at 400 °C and 500 °C, increases the saturation of the sample's yellow color, while by annealing at 600 °C and 700 °C, black samples are produced.

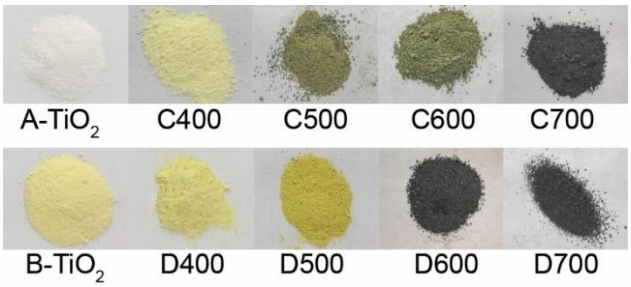

Figure 3.1. Picture of synthesized samples. A is undoped sample, B is doped during hydrolysis, C400-700 powders are doped by annealing undoped sample under ammonia flow, D400-700 samples are made by exposing B-TiO_2 samples to ammonia at different temperatures (doped both during hydrolysis and annealing).

Figure 3.2 shows the XRD pattern of synthesized samples. From the XRD patterns, the average crystallite size of samples were calculated, using Debye-Scherrer equation, which is proven to give a reliable estimate of average crystallite size [121]. The results are presented in Table 3.3. One can conclude from the peaks that

increasing the annealing temperature, enhances crystallinity (intensity of peaks increases) and crystallite size of the samples (peak width decreases).

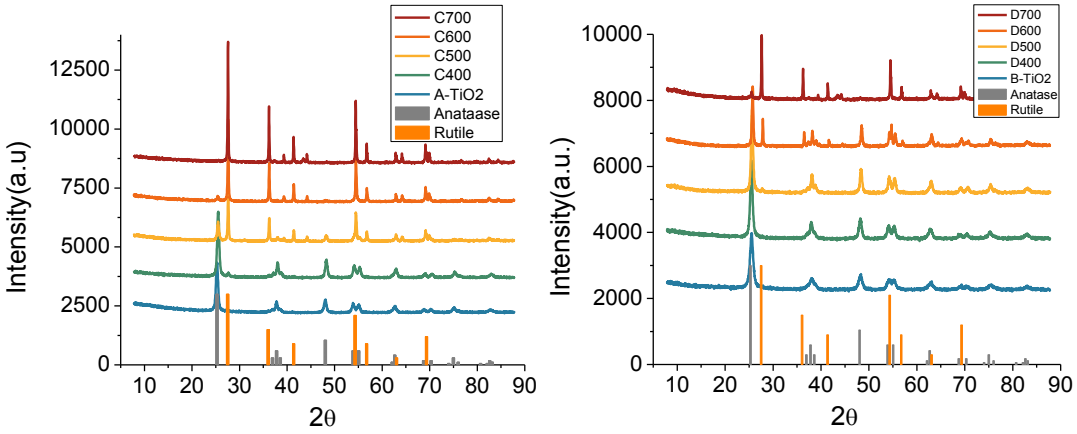

Figure 3.2. XRD Pattern of TiO_2 samples; left: A-TiO_2 and C samples, bottom: B-TiO_2 and D samples. Each figure contains the reference peaks of anatase (PDF code 00-004-0477) and rutile (PDF code 04-006-2536) with their relative intensities.

To determine the available surface area, BET analyses were performed on all synthesized samples; the results of which are shown in Table 3.3. In each set of samples, while annealing temperature increase, the surface area decreases, with a sever diminish of surface area when annealing at 700 °C.

Table 3.3. Average crystallite size obtained from XRD pattern of samples using Debye Scherrer equation

Sample name		A-TiO_2	C400	C500	C600	C700	B-TiO_2	C400	C500	C600	C700
Doping method		undoped	Ammonia exposure during calcination				During hydrolysis	During hydrolysis and ammonia exposure during calcination			
Crystallite size (nm)	Anatase	16	17	19	27	-	11	15	18	27	36
	Rutile	-	22	38	40	50	-	-	27	45	53
Surface area (m^2 g^{-1})		77.6	44.28	30.2	22.04	1.71	131.7	75.08	35.78	3.262	3.07

It is noteworthy that the presence of ammonium hydroxide in the hydrolysis step decreases average crystallite size, leading to increase of surface area. Also, by comparison of XRD patterns of C and D samples one can conclude that the presence

of ammonium hydroxide during hydrolysis, causes the anatase/rutile phase transformation to happen at higher temperatures. To investigate this phenomenon, two samples of titanium dioxide were made following the procedure for samples A-TiO_2 and B-TiO_2, without the final calcination step. Dried powders where heated from 200 °C to 725 °C in 15 °C increments and 10 min of rest time, followed by diffraction measurement after each step. The results are presented in Figure 3.3.

For the undoped sample, by annealing from 200 °C to 515 °C, crystallinity of anatase phase, peak width, and therefore average size increase gradually. At 530 °C, the first representative peaks of rutile appeared in the sample, and further annealing increased the intensity of this peak, while decreasing the intensity of anatase peaks, which followed by complete disappearance of anatase peaks at 695 °C.

For the doped sample, however, crystallinity and average crystallite size were increased by annealing from 200 °C to 630 °C, while only anatase phase was detected. At 635 °C, the first signs of rutile phase were observed, and annealing in higher temperatures gradually increased the intensity of rutile phase. However, after reaching 725 °C and 10 min rest in this temperature, much of the sample, judging by relative intensities of the main peaks of anatase and rutile, is comprised of anatase.

Moreover, the authors think that the lack of formation of the rutile phase leads to larger grains of anatase in D-TiO_2 samples, in contrast to formation of smaller rutile particles in C-TiO_2 samples, which causes D600 sample to have a much lower surface area compared to C600. For the complete set of results please see supporting information.

Aside from affecting the anatase/rutile phase transformation temperature, nitrogen doping also seems to alter the kinetic of this transformation. The B-TiO_2 sample showed a much slower rutile/anatase transformation rate upon annealing, which led to

major anatase phase even after annealing at 725 °C, while in case of the undoped sample, rutile forms at 530 °C and the transformation is complete at 680 °C. This could be due to internal strain that substitutional/interstitial nitrogen forces to the structure. Since the unit cell of anatase has a lower density and is more stretched towards the c axis, it would be more receptive towards strain caused by doped nitrogen, making it the favorable phase of *N*-doped TiO_2 [122].

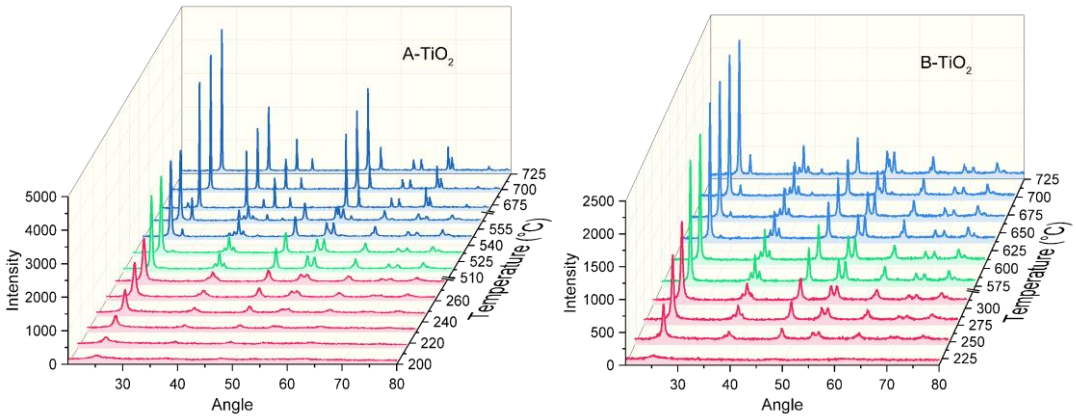

Figure 3.3 Non-ambient XRD measurements of undoped (A-TiO_2) and doped (during hydrolysis, B-TiO_2) samples. The graph on the left has breaks from 280 °C to 510 °C and from 570 °C to 665 °C, and the graph on the right has a break from 325 °C to 570 °C. For both plots: red part shows beginning of crystallization, green part shows the increase in crystallinity of anatase phase, blue part indicates formation of rutile.

Figure 3.4 shows TEM images of synthesized nanoparticles. Individual particles are observed within larger agglomerates, which is a disadvantage of sol-gel method. Images show particles with sizes smaller than 20 nm and of different shapes. Particles are mostly imperfect octahedrons; however cubic particles are also observable. By measuring the d-spacing, it was found out that the cubic particles have (001) and (100) facets, while octahedrons have (110) and (001) facets on the outside.

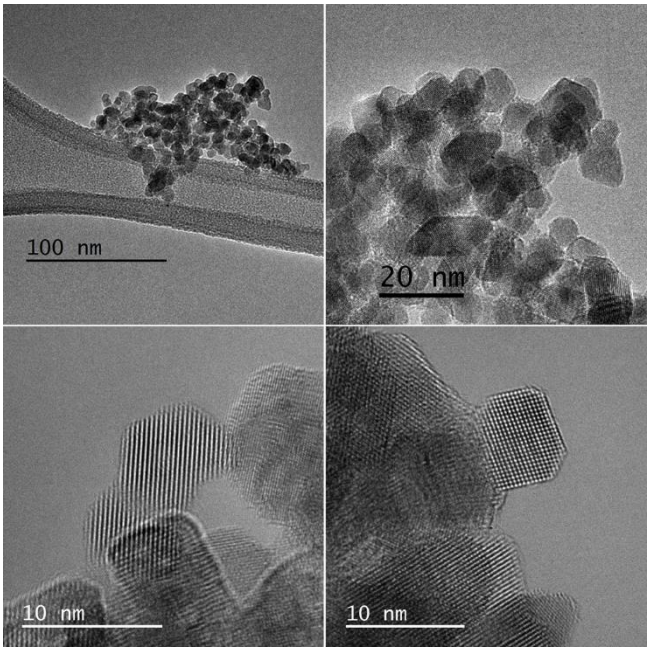

Figure 3.4. TEM image of sample C500; synthesized undoped, then annealed under ammonia flow at 500 ˚C for 1 hour.

Figure 3.5 shows SEM images of C400 and C700 samples obtained by using secondary electron detector in STEM mode. From these images, size and size distribution of the nanoparticles has been increased by annealing at 700 °C. The agglomerates at 700 °C, are consisted of small particles, mixed with (relatively) much larger ones.

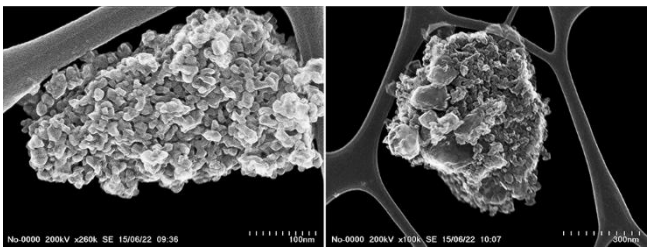

Figure 3.5. SEM image of samples D400 (top) and D700 (bottom).

FT-IR transmission spectra of synthesized samples are shown in Figure 3.6. The inset is obtained by normalizing each sample's data on a 0-1 scale and is representative of wavenumbers between 3000 cm^{-1} to 4000 cm^{-1}, which were not detectable from the main plots. The peak around 1625-1630 cm^{-1} is attributed to bending of H_2O (δ H_2O), and the peak at 3400 cm^{-1} is from O–H stretching vibration.

The other peak, which is present in all samples regardless of their annealing temperature is located at 2354 cm^{-1} and represents adsorbed CO_2. The absence of CH, C=O, C-O and C-N peaks, shows successful elimination of carbon species, present in the utilized precursors.

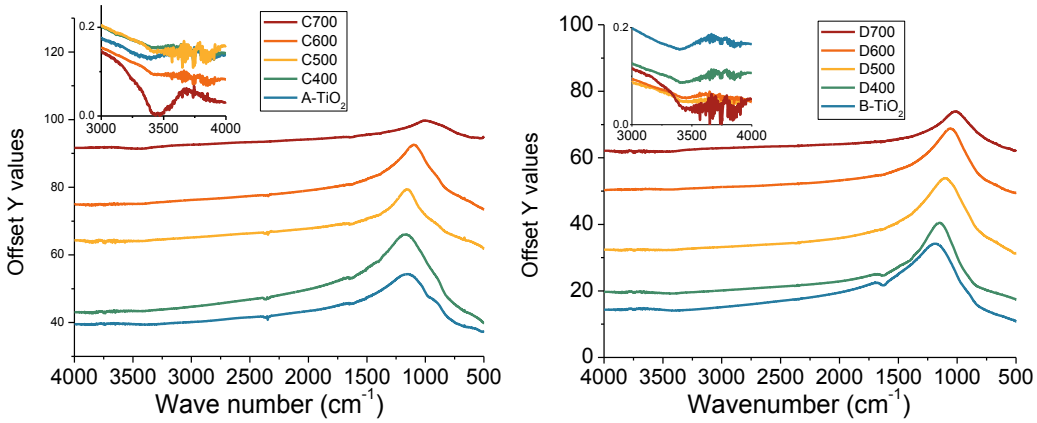

Figure 3.6. FT-IR spectra of left: A-TiO_2 and C samples, right: B-TiO_2 and D samples. The inset is the normalized part of the same data, for wavenumbers between 3000 cm^{-1} to 4000 cm^{-1}.

Figure 3.7 shows XPS spectra of N1s binding energy range of all synthesized samples, plus the fitted curves for each sample. To find dopant percentages, peak area of nitrogen and titanium were measured and corrected by their relative sensitivity factors. Information about N1s peaks, doping percentage and nitrogen species for each sample are presented in

Table 3.4. Survey XPS spectra of all samples are represented in the ESI.

Predictably, no peak was found within the N1s XPS result of the undoped sample (A-TiO_2). For sample B-TiO_2, which is synthesized by wet chemical methods, one peak was observed at 401.9 eV, which was attributed to chemisorbed γ-N_2 (*i.e.* Ti–O–N–N) [26, 123]. By annealing this sample under ammonia flow at 400 (sample D400) and 500 °C (sample D500), the peak at 401.9 eV vanishes, and a new peak appears at

~400 eV. This peak could represent NO_x (*i.e.* Ti–O–N–O) or NH_x species [26, 123]. The same type of nitrogen species appears after annealing the undoped sample at 400 (sample C400) and 500 °C (sample C500) with almost the same quantity (1.7 and 1.19%). This shows that the nitrogen that was doped in the structure by wet chemical method of synthesis will be gone after annealing at 400 °C and new nitrogen species will appear in the structure. However, Figure 3.7 shows that the amount of nitrogen in the structure is higher when the sample was annealed under ammonia flow at 400 °C, compared to annealing at 500 °C. Annealing under ammonia flow at higher temperatures results in two distinct nitrogen species with XPS peaks centered around 396 eV and 402 eV. The peaks located around 396 eV, are attributed to substitutional N and are a characteristic of nitrogen doping using dry methods [2, 26].

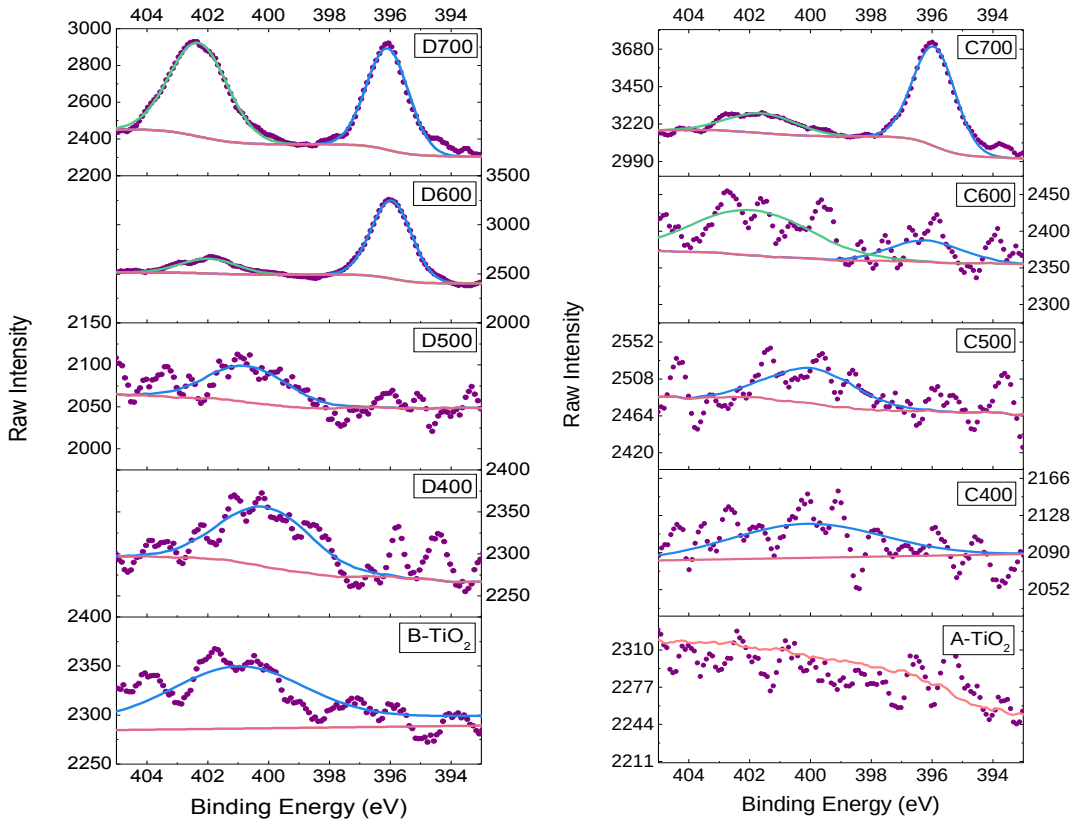

Figure 3.7. XPS N1s spectra of synthesized samples. Backgrounds were found using XPS peak software, and the Shirley method.

Table 3.4. Peak information extracted from XPS spectra of samples presented in Figure 3.7.

Sample name	Peak Centre (eV)	N species	N: Ti ratio (%)	Sample name	Peak Centre (eV)	N species	N: Ti ratio (%)
A-TiO_2	NA	-	-	B-TiO_2	401.9	Chemisorbed γ-N_2	3.1
C400	400.1	NO_x or NH_x	1.7	D400	400.1	NO_x or NH_x	2.0
C500	399.9	NO_x or NH_x	1.2	D500	400.7	NO_x or NH_x	1.1
C600	396.2	Substitutional N	0.7	D600	396.0	Substitutional N	14.4
	401.9	Chemisorbed γ-N_2	3.1		402.0	Chemisorbed γ-N_2	3.8
C700	395.9	Substitutional N	17.1	D700	396.1	Substitutional N	12.2
	401.6	Chemisorbed γ-N_2	5.5		402.3	Chemisorbed γ-N_2	15.4

As discussed in the introduction section, an increase in the nitrogen content of *N*-doped TiO_2 leads to production of oxygen vacancies, and subsequently Ti^{3+} species in samples to preserve overall charge neutrality. Evidence of such phenomenon was observed from Ti 2p XPS peaks of samples doped in high temperatures in Figure 3.8 XPS result of all samples contains peaks at 459.0 eV and 464.6 eV, which are attributed to Ti^{4+}. On peaks at 457.7 eV and 462.0 eV, which represent Ti^{3+} species are observed for samples with a nitrogen content of 18.2% or more.

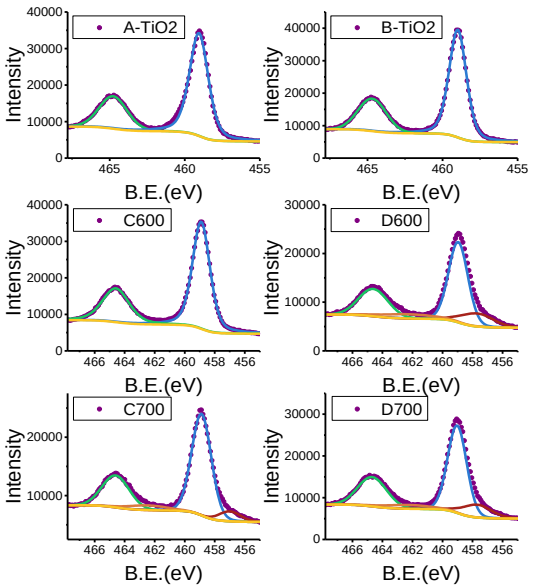

Figure 3.8. Ti 2p XPS spectra of samples. Peaks at 495.0 eV and 464.6 eV are attributed to Ti^{4+}, while peaks at 457.7 eV and 462 eV represent Ti^{3+} species that are to

preserve charge neutrality when nitrogen content increases in the structure of *N*-doped TiO_2.

Diffuse Reflectance absorption measurements were done using the 150 mm sphere accessory of the UV-vis spectrometer, with a Spectralon reference.

Figure 3.9 shows the absorption spectra of samples. Spectra of the undoped sample (A-TiO_2) is placed in both graphs for comparison. While in the undoped sample absorption increases from 450 nm, doped samples show absorption at about 550 nm.

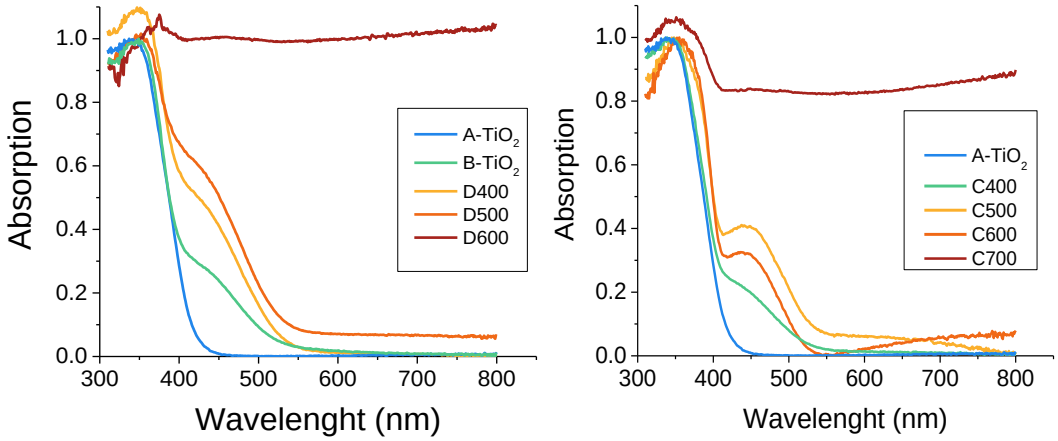

Figure 3.9. Absorption spectra of synthesized nanoparticles.

From absorption spectra, bandgap of synthesized nanoparticles was measured. For this purpose, maximum of the absolute value of the first derivative of absorption spectra graph was measured, which represents the inflection point of the absorption spectra and its local maximum slope as shown in

Figure 3.10. The obtained wavelength energy represents the band-gap energy of the synthesized nanoparticles. The differential reflectance method has been suggested for highly crystalline semi-conductor samples, in contrast to Tauc plot method, which was originally performed for less crystalline, or amorphous materials [124-126]. For the undoped sample, one maximum was calculated at 389 nm, thus the band-gap was measured to be 3.2 eV. For B-TiO_2 sample as well as C and D samples however, two maximums were calculated at 389 nm and 485 nm, which corresponds to 3.2 eV and

2.6 eV. It is noteworthy that this method of finding the bandgap energy could be performed even for black samples, which absorb all the visible spectrum.

Absorption spectra of doped samples show two types of behavior of the samples too. This could be related to presence of undoped nanocrystals, and therefore coexistence of un-doped and doped material, with band-gaps of ~3.2 eV and 2.6 eV respectively. Moreover, because samples that were doped above 600 °C are black, very strong absorption in visible spectrum was of course observed. Additionally, it can be seen a red shift happens on the larger peak's position from ~380 nm to 390 nm, as annealing temperature increases. This is due to formation of rutile in these samples, which has a lower energy band-gap.

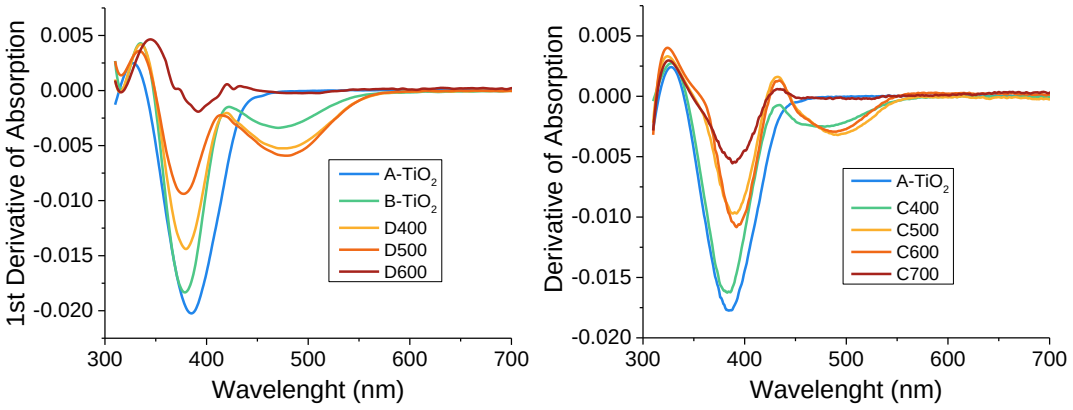

Figure 3.10. First derivative of diffuse reflectance absorption data.

Photocatalytic activity of synthesized nanoparticles was measured by degradation of methyl orange solution over UV filtered light for 2 h. For all measurements, 200 mL of 20 ppm methyl orange solution and 1000 ppm catalyst was used. The results are presented in Figure 3.11, which shows that undoped sample, as well as samples doped with ammonia flow at 600 °C and 700 °C are not photocatalytically active under visible-light. This is interesting since these samples (excluding undoped sample) have the highest visible-light absorption of all samples and virtually absorb all the visible spectrum.

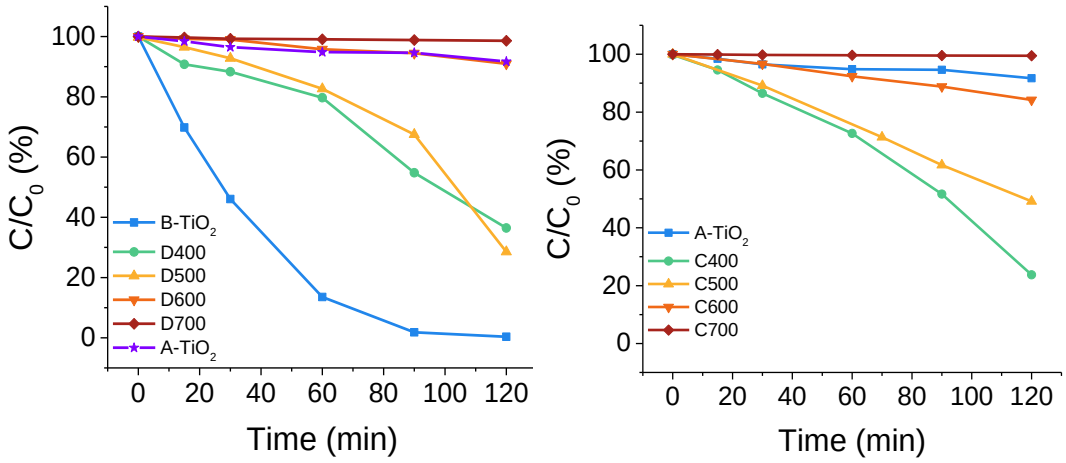

Figure 3.11. Photocatalytic efficiency of samples for degradation of Methyl orange under visible-light.

Results obtained from Figure 3.11, alongside the best results among articles reviewed in Table 3.1, which use the sol-gel method are presented in Table 3.5. Degradation is converted to figure of merit ($kW.h.m^{-3}$) to provide ability to compare the results to other articles' results. It can be seen, that photocatalytic activity has been improved noticeably compared to other sol-gel samples that are represented in Table 3.1.

The lack of photocatalytic activity for undoped sample is simply absence of UV light and the large band-gap of undoped TiO_2, which is the main motivation of doping; moreover, it shows that photocatalytic activity of the samples has not been affected by photosensitization due to presence of the dye molecules, and UV-light has been filtered effectively. On the other hand, inactivity of doped samples that are annealed at higher temperatures under ammonia flow, could be due to an increase in electron-hole recombination rates, through creation of oxygen vacancies at high temperatures by ammonia, which act as recombination sites. Another reason for decrease in photocatalytic activity could be due to decrease of surface area.

To compare the effect of these to phenomenon, achieved degradation of each sample was divided by its surface area, which gives degradation per m^2 of available catalyst surface. The results show an increase in degradation per m^2 of surface as doping temperature, and consequently dopant concentration increase, which means the decline in degradation efficiency is due to decrease in surface area (see ESI). However, degradation per m^2 decreases when reaching doping temperatures of 600 for sample C600, which could be due to excessive amounts of doped nitrogen, leading to formation of oxygen vacancies, increasing recombination rates and lowering degradation efficiency. Another explanation could be formation of rutile, which is shown to have a lower photocatalytic activity compared to anatase [18].

Table 3.5. Results for degradation of methyl orange using synthesized *N*-doped samples. Concertation of methyl orange was 20 ppm, solution volume was 200 mL, and 1 g/L of catalyst was used.

Sample	Degradation (%)	Degradation per m^2 of surface ($\%.m^{-2}$)	Figure of Merit ($kW.h.m^{-3}$)
A-TiO_2	8.3%	0.53%	79,823
C400	76.2%	8.61%	4,806
C500	50.9%	8.42%	9,728
C600	15.8%	3.58%	40,167
B-TiO_2	99.7%	3.78%	1,222
D400	63.6%	4.23%	6,843
D500	71.5%	9.99%	5,510
D600	9.0%	13.84%	7,2990
Wei et al.[108]	90%	73.41%	4,000

Amongst all samples, B-TiO_2 has the highest photocatalytic activity, which is interesting since this sample has one of the lowest amounts of doped nitrogen. Photocatalytic activity of this sample shows significant improvement, compared to previous studies listed in Table 3.1, while other doped samples (C400, C500, D400, D500-TiO_2) show good degradation, their activity is rather lower than B-TiO_2. This could be due to several factors, including increase of size and therefore reduced

surface area, diminish of anatase phase, which is more potent photocatalytically, and finally, because of increase of oxygen vacancies that act as recombination sites.

Samples C400, C500 and D400, all share the same nitrogen species, with binding energy of 400 eV, which was attributed to NO_x or NH_x; while no other type of nitrogen was observed in the XPS data. Photocatalytic activity of these samples is contrary to the claim by Asahi et al. [2] that this type of nitrogen is not necessarily contributing to the visible-light photocatalytic activity. In addition, one can conclude that the combination of doping during hydrolysis and calcination (D samples) results in less photocatalytically effective *N*-doped TiO_2, in comparison to doping only during calcination (C samples). The reason for this phenomenon could be the phase of samples, and their surface areas, and their more suitable nitrogen content.

3.5. Conclusions

N-doped titanium dioxide nanoparticles were synthesized using sol-gel method. Nitrogen was doped in TiO_2 either during hydrolysis step, during calcination, or a combination of both methods. The effect of different doping methods on photocatalytic properties of TiO_2 nanoparticles, as well as, their phase was investigated. It was shown that presence of ammonia in the hydrolysis step decreases crystallite size and lowers crystallite growth rate at high temperatures. Moreover, using ammonia during the hydrolysis, significantly increases the anatase/rutile phase transformation temperature and shifts it from 550 °C to 635 °C, which causes the nanoparticles to be mostly anatase even after annealing at 725 °C.

All synthesized *N*-doped TiO_2 nanoparticles were photocatalytic active under irradiation with visible-light. Samples that were doped during hydrolysis showed the highest activity relative to other synthesized nanoparticles, as well as a significant improvement compared to the results obtained by other articles, which were reviewed

in this report. By increasing the ammonia exposure temperature, photocatalytic activity started to decrease, and after annealing at 700 °C no significant activity was measured. This was attributed to a decreasing surface area, phase transformation from anatase to rutile, and presence of oxygen vacancies that form at higher temperatures from reaction of decomposed ammonia and TiO_2 acting as recombination sites. Higher photocatalytic activity of samples that were doped only during hydrolysis, in comparison to other samples, was associated to small crystallite size (lowest of all samples) and high surface area, while having good crystallinity and low number of oxygen vacancies in the structure.

Overall it was concluded that to obtain the highest photocatalytic activity of sol-gel synthesized TiO_2 nanoparticles, doping with nitrogen should take place during the hydrolysis step. Further annealing with ammonia flow, would only increase particle size, and create oxygen vacancies that act as recombination sites, thus, lowering the photocatalytic activity of synthesized nanoparticles.

3.6. Supporting information

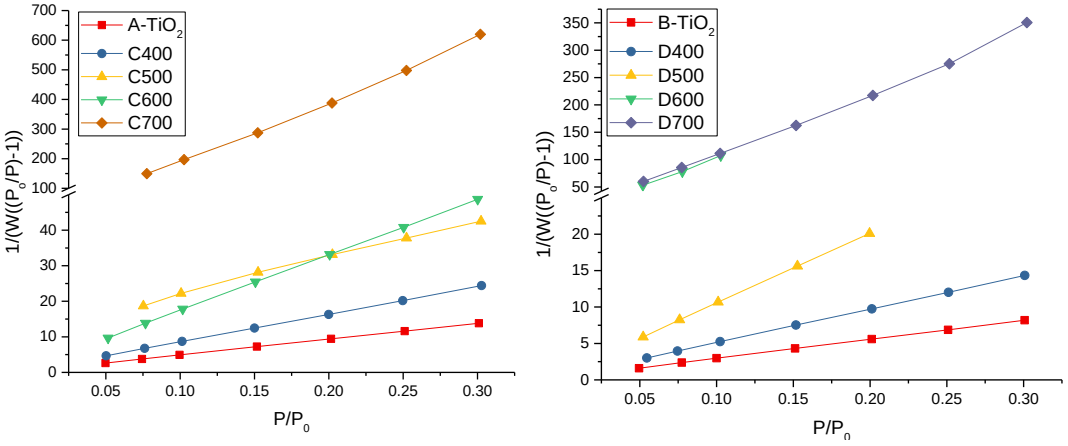

Figure S3.1 BET plot of synthesized samples.

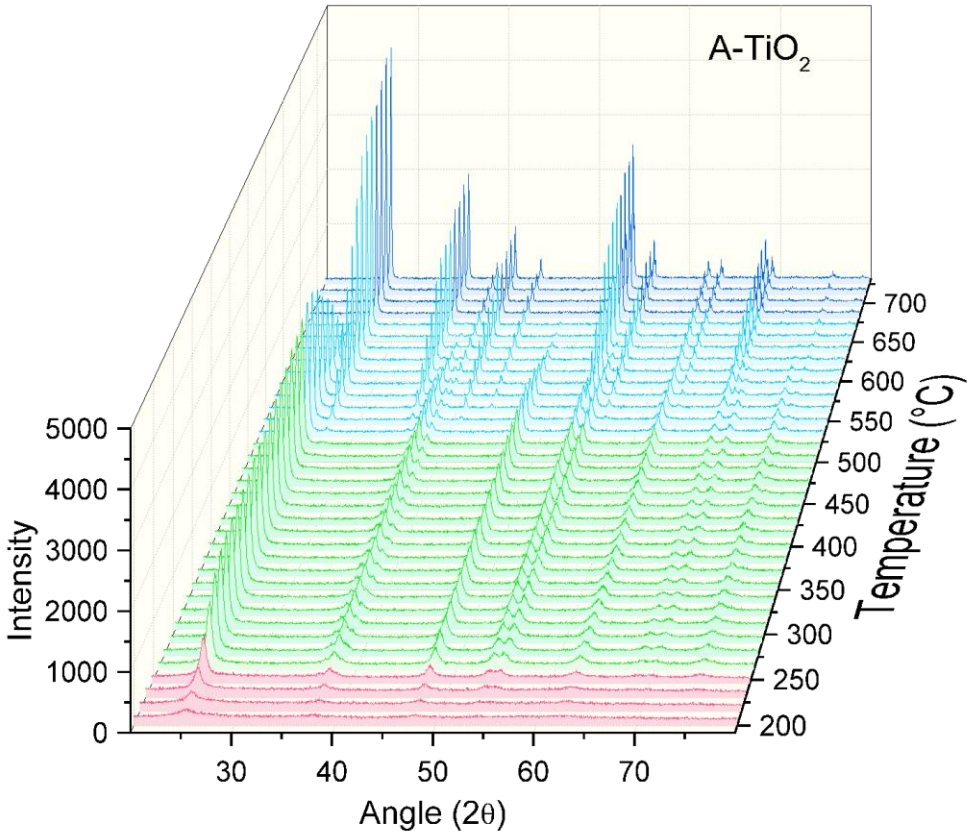

Figure S3.2 Non-ambient XRD pattern of sample A-TiO_2, heated from 200 °C to 725 °C in 15 °C increments, with 10 min rest at each temperature. Red part shows beginning of crystallization, green part shows the increase in crystallinity of anatase phase, cyan part marks the beginning of formation of rutile phase, blue part indicates completion of rutile formation (no anatase remained).

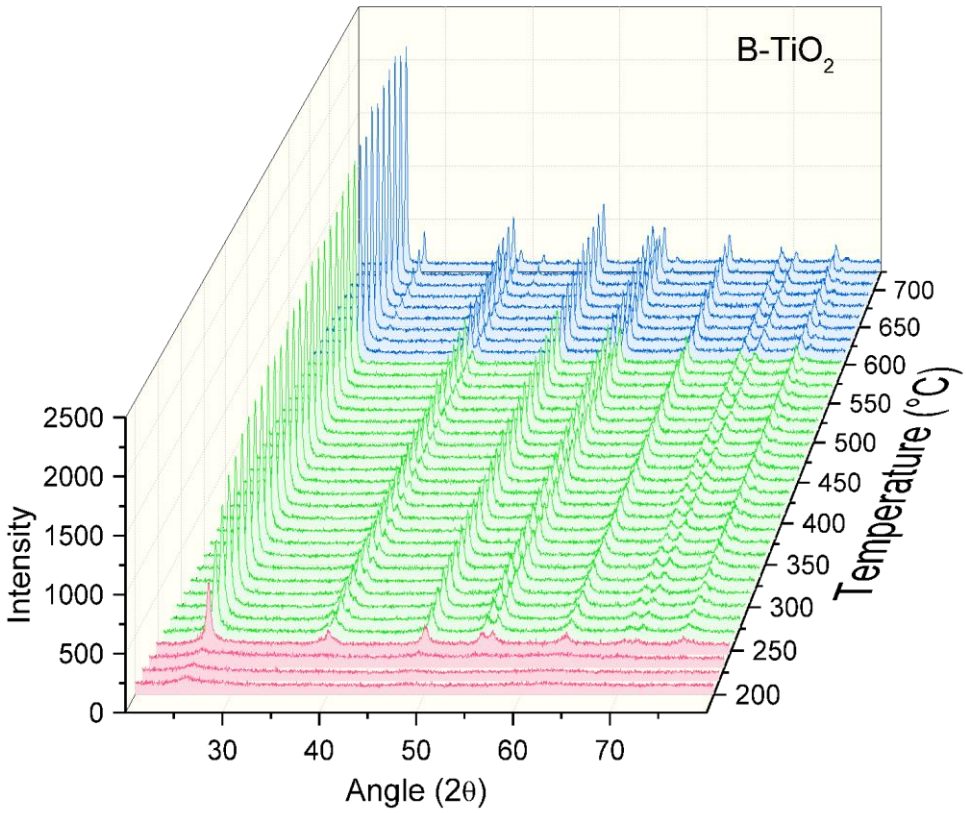

Figure S3.3 Non-ambient XRD pattern of sample B-TiO_2, heated from 200 °C to 725 °C in 15 °C increments, with 10 min rest at each temperature. Red part shows beginning of crystallization, green part shows the increase in crystallinity of anatase phase, blue part marks the beginning of formation of rutile phase.

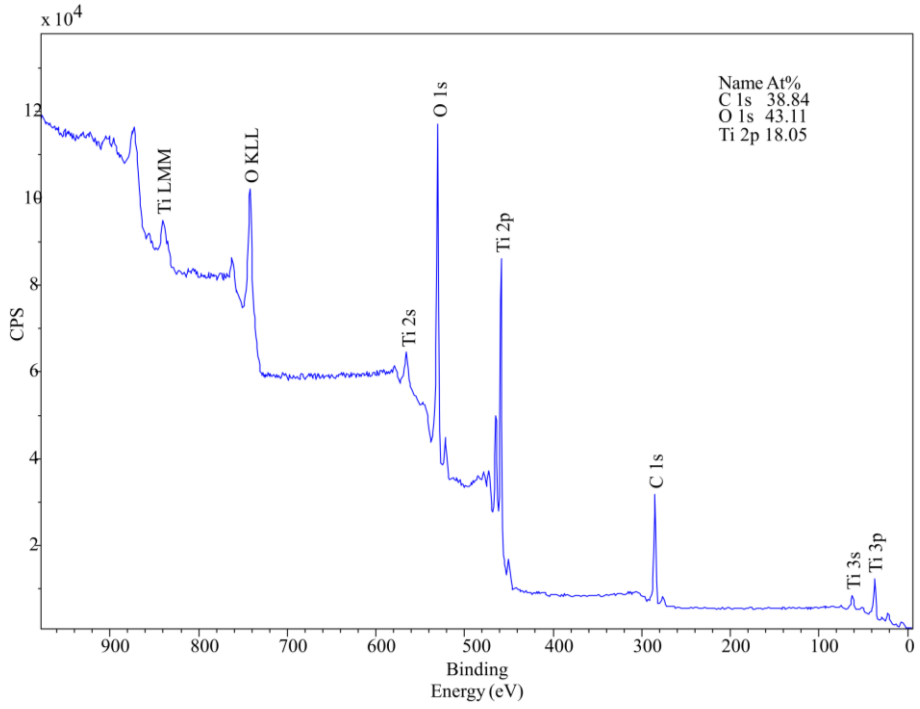

Figure S3.4 XPS survey spectrum of sample A-TiO_2.

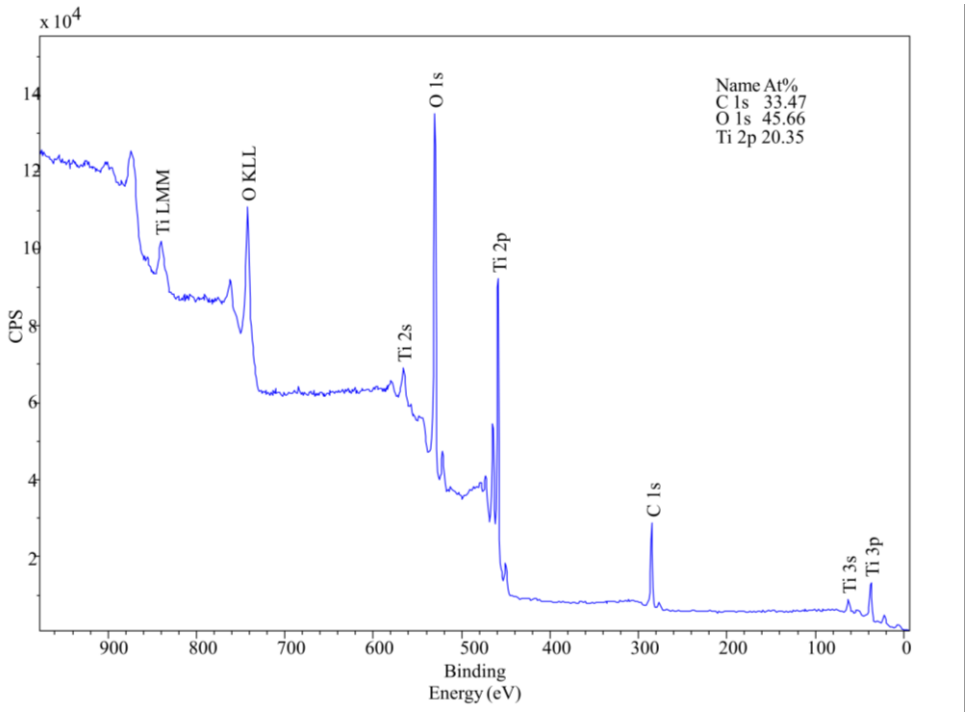

Figure S3.5 XPS survey spectrum of sample B-TiO_2.

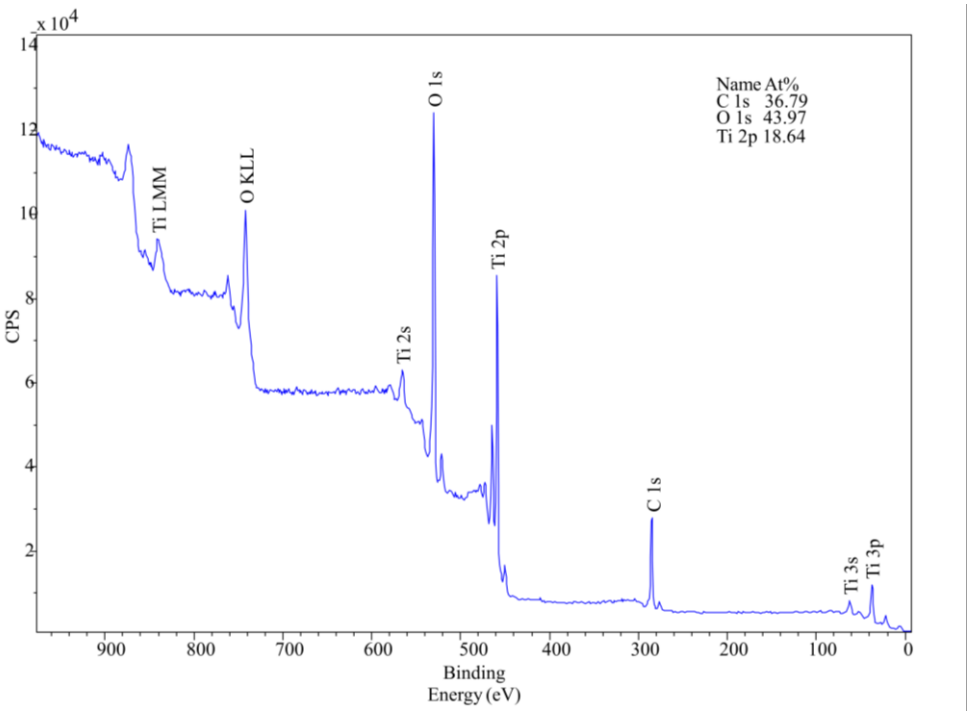

Figure S3.6 XPS survey spectrum of sample C400.

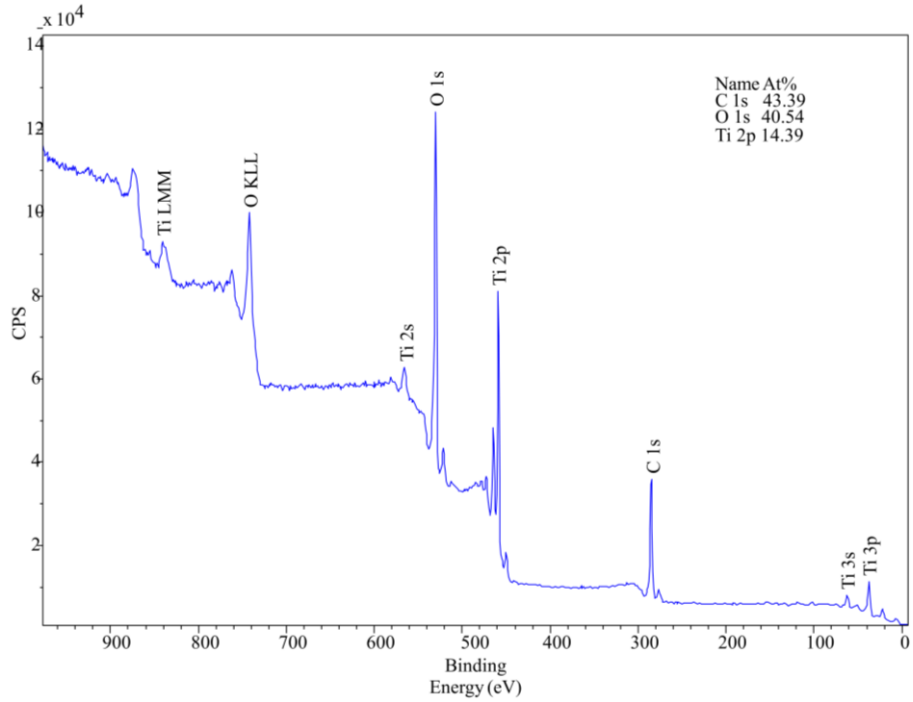

Figure S3.7 XPS survey spectrum of sample C500.

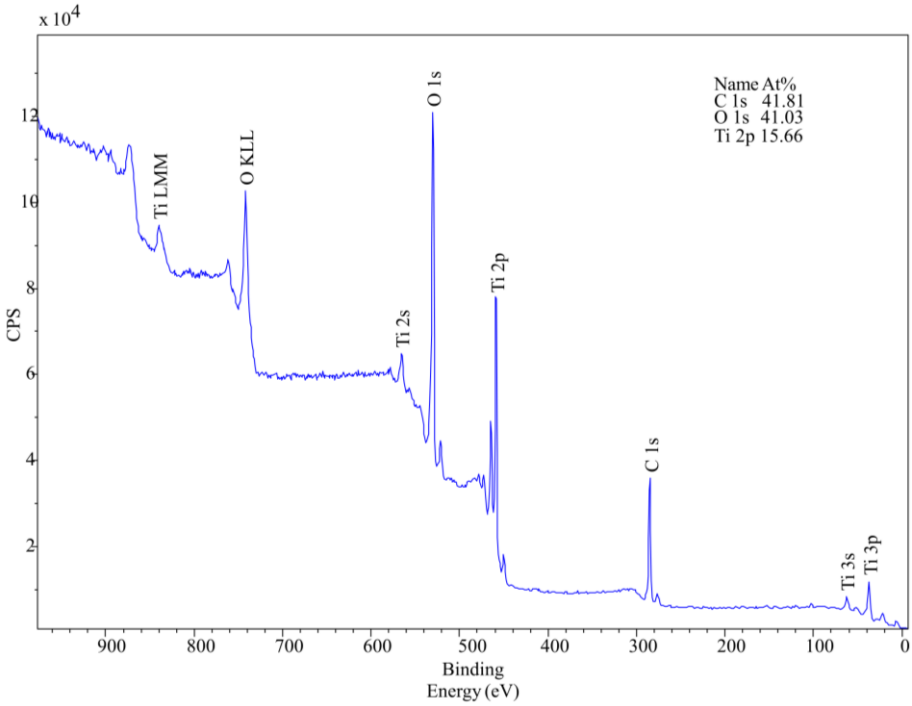

Figure S3.8 XPS survey spectrum of sample C600.

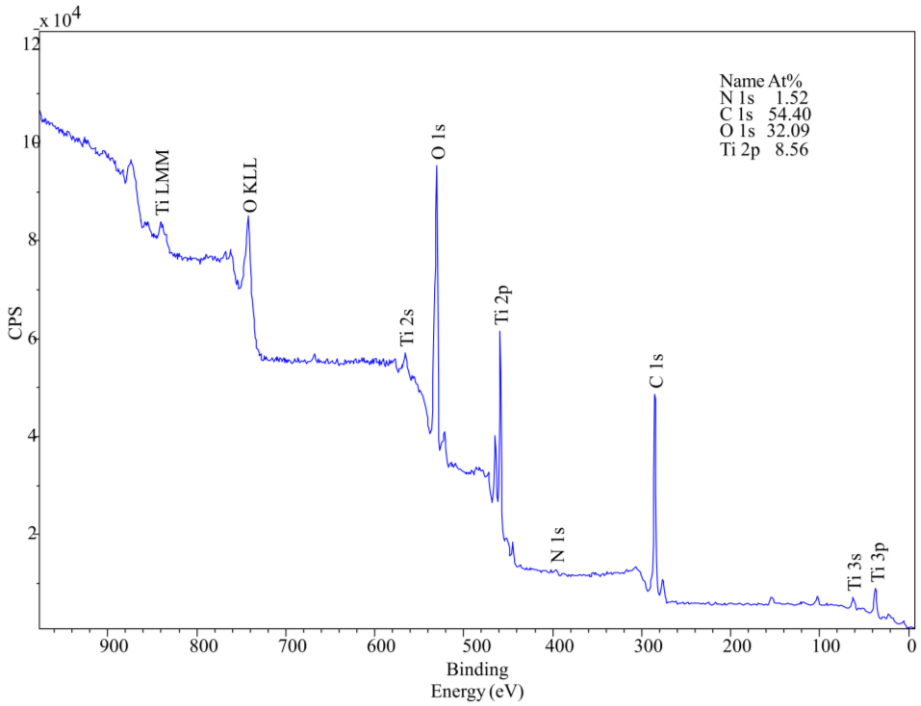

Figure S3.9 XPS survey spectrum of sample C700.

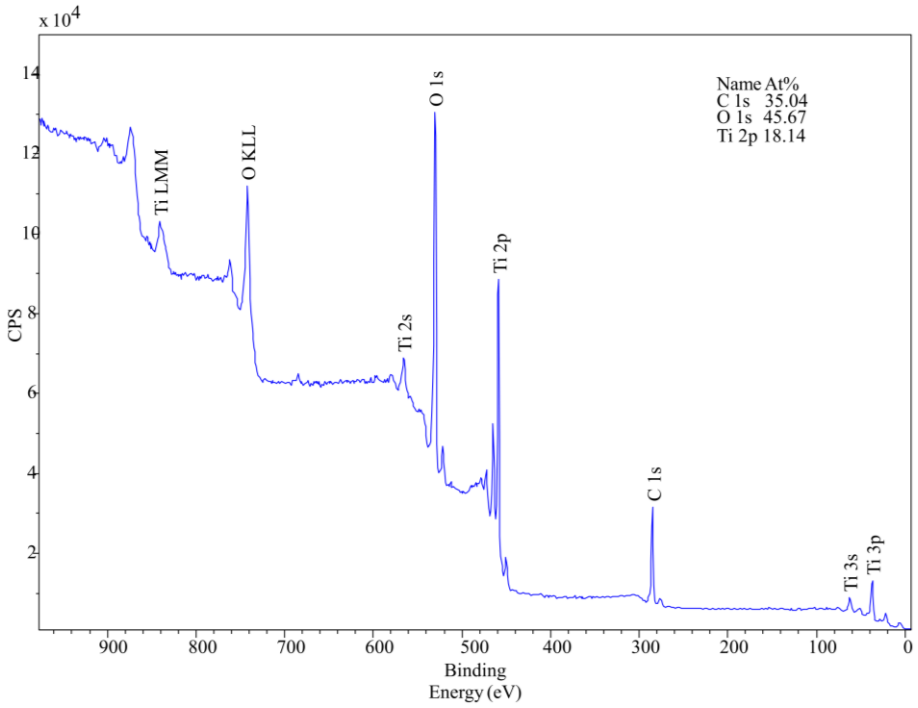

Figure S3.10 XPS survey spectrum of sample D400.

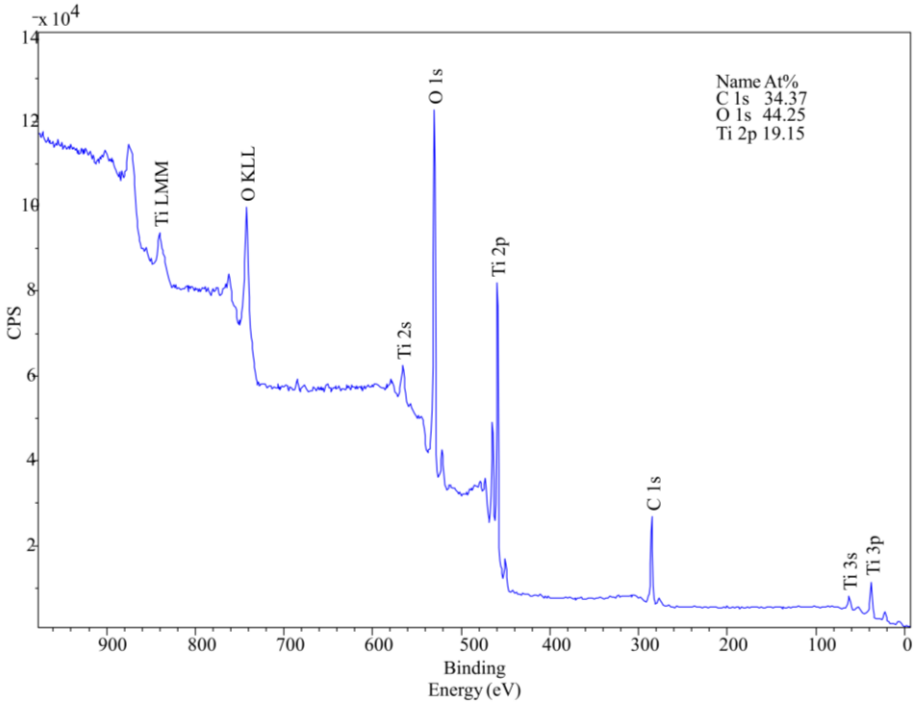

Figure S3.11 XPS survey spectrum of sample D500.

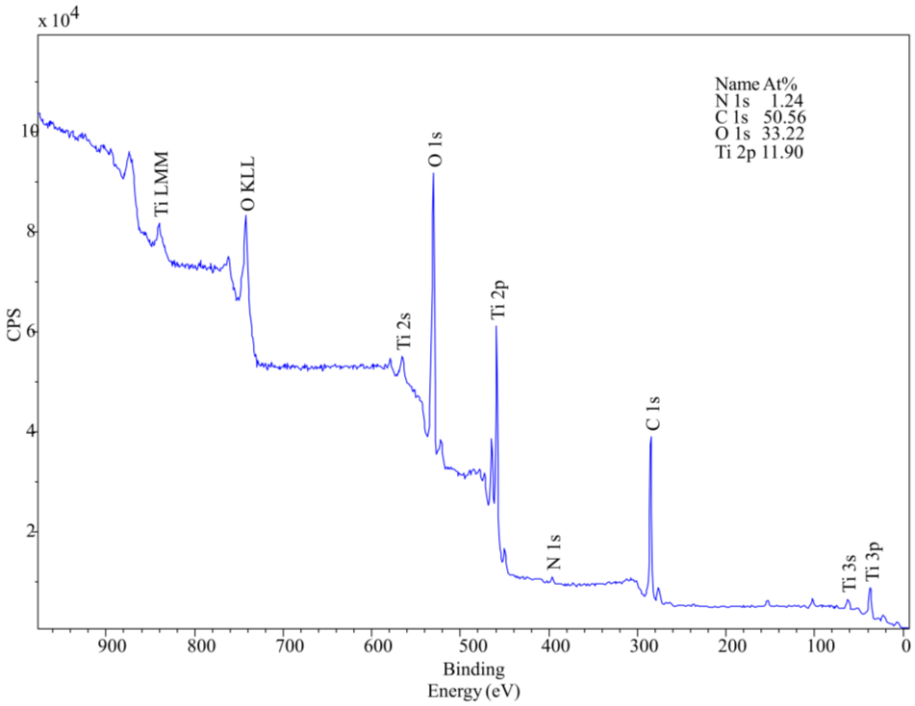

Figure S3.12 XPS survey spectrum of sample D600.

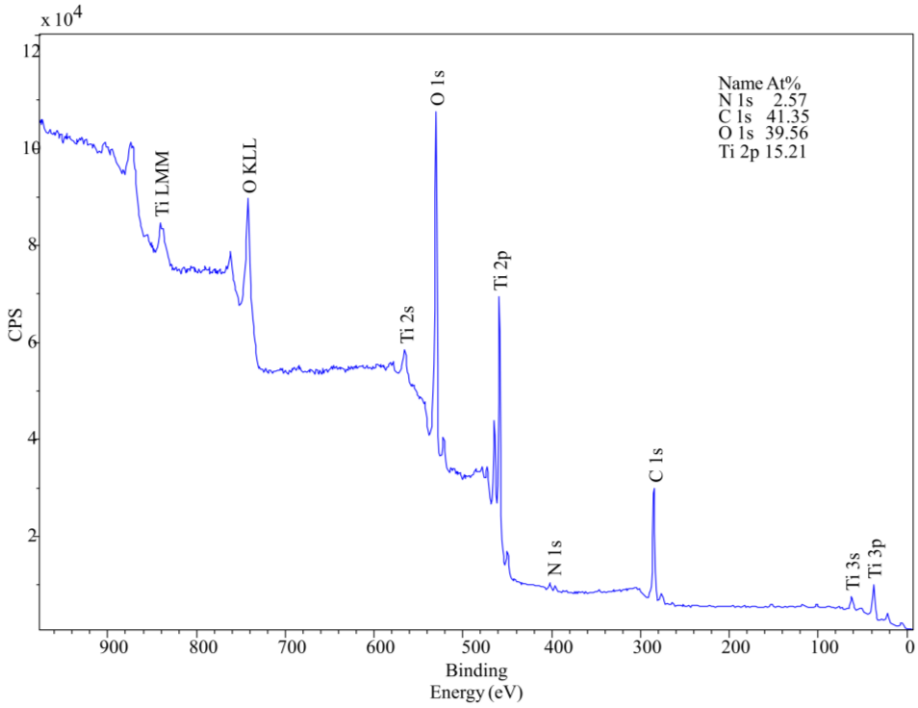

Figure S3.13 XPS survey spectrum of sample D700.

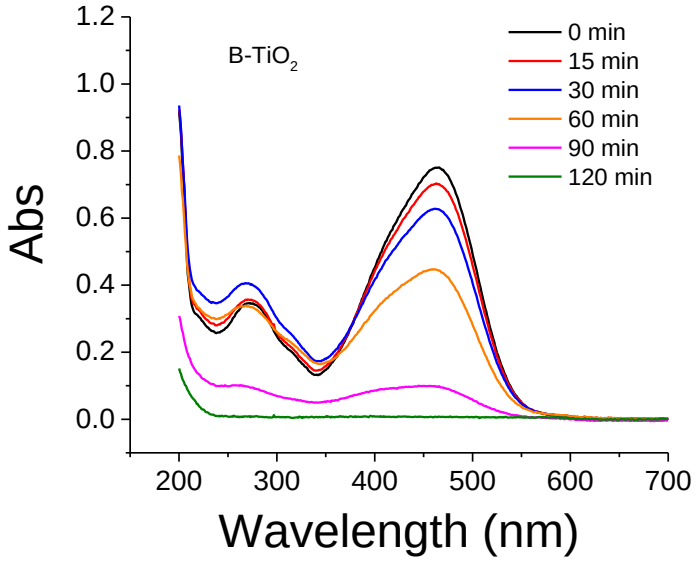

Figure S3.14 UV-Vis spectrum of methyl orange solution during the treatment by B-TiO_2, showing gradual diminish of methyl orange's characteristic peak.

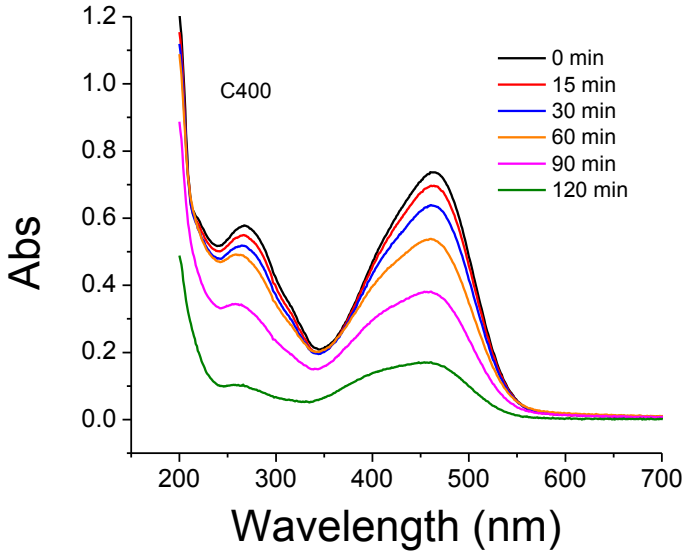

Figure S3.15 UV-Vis spectrum of methyl orange solution during the treatment by C400, showing gradual diminish of methyl orange's characteristic peak.

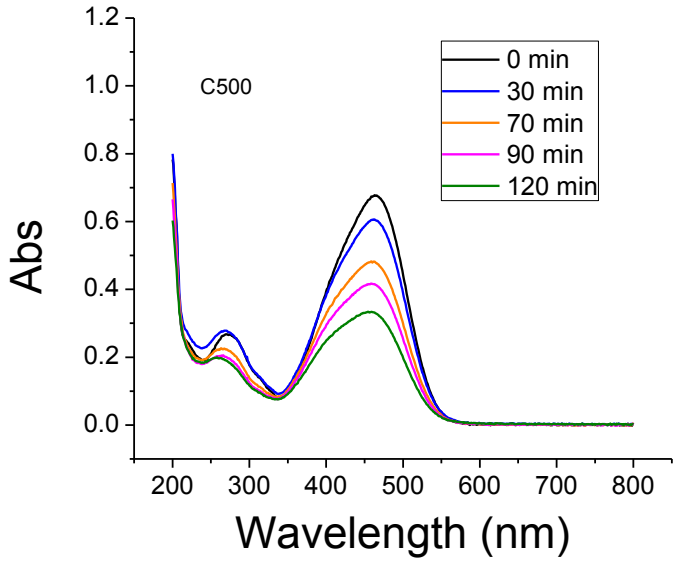

Figure S3.16 UV-Vis spectrum of methyl orange solution during the treatment by C500, showing gradual diminish of methyl orange's characteristic peak.

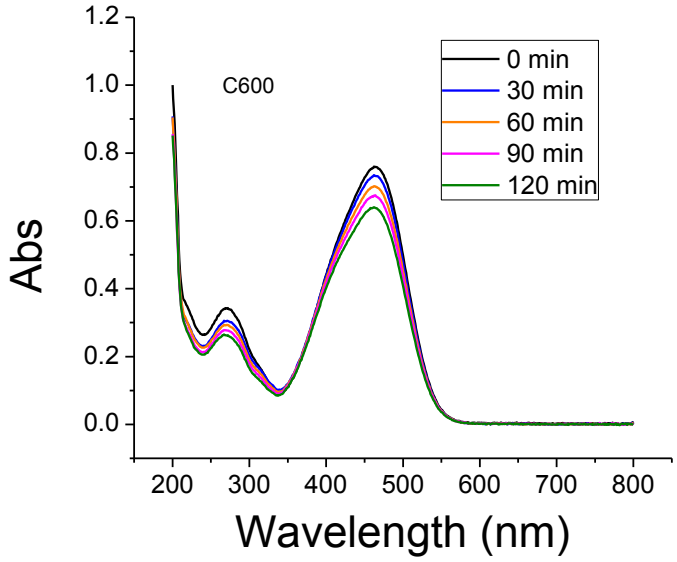

Figure S3.17 UV-Vis spectrum of methyl orange solution during the treatment by C600, showing gradual diminish of methyl orange's characteristic peak.

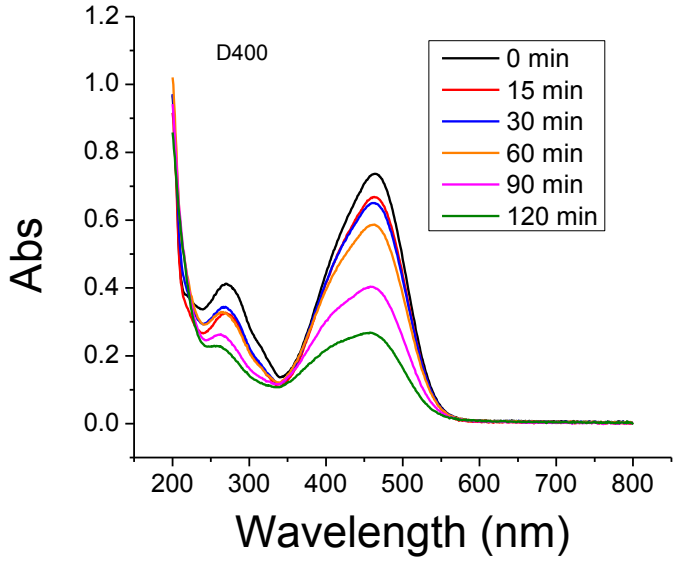

Figure S3.18 UV-Vis spectrum of methyl orange solution during the treatment by D400, showing gradual diminish of methyl orange's characteristic peak.

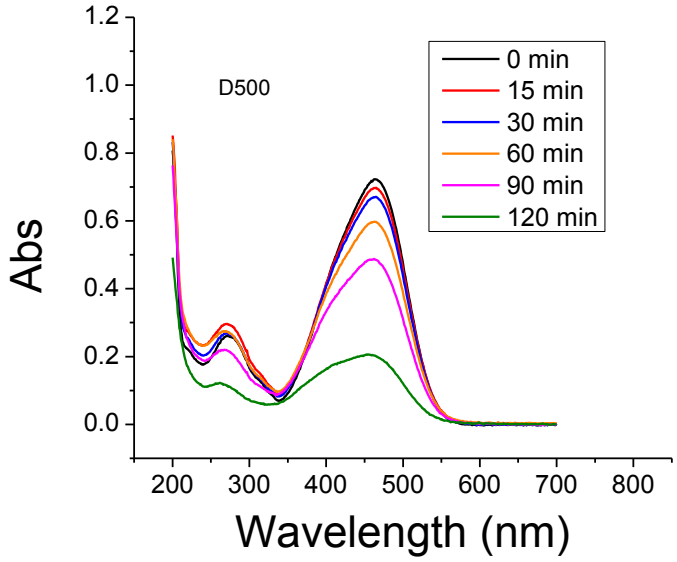

Figure S3.19 UV-Vis spectrum of methyl orange solution during the treatment by D500, showing gradual diminish of methyl orange's characteristic peak.

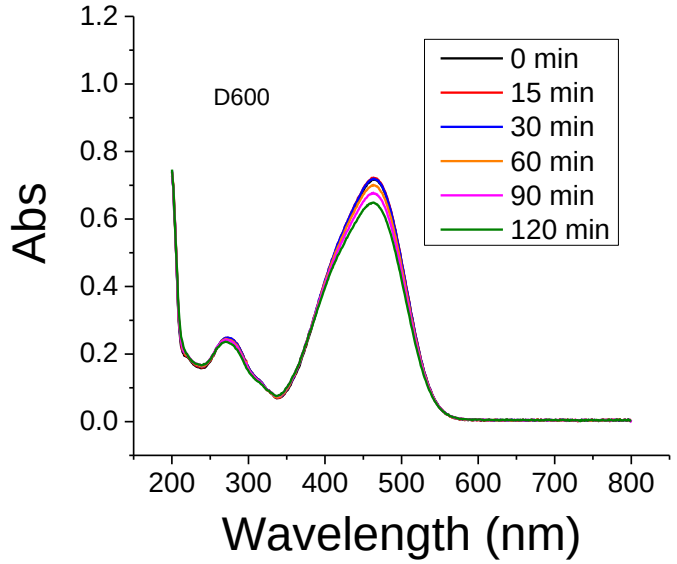

Figure S3.20 UV-Vis spectrum of methyl orange solution during the treatment by D600, showing gradual diminish of methyl orange's characteristic peak.

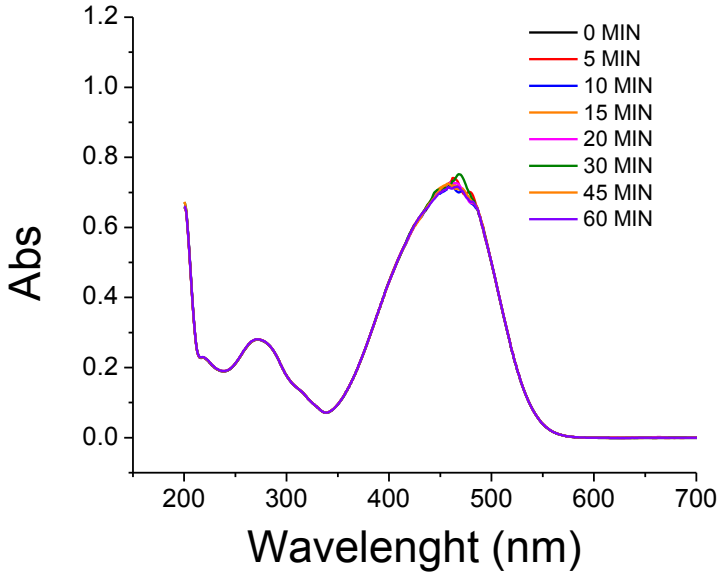

Figure S3.21 UV-Vis spectrum of the control methyl orange solution under light without any catalyst. The graph shows no detectable degradation due to the light source.

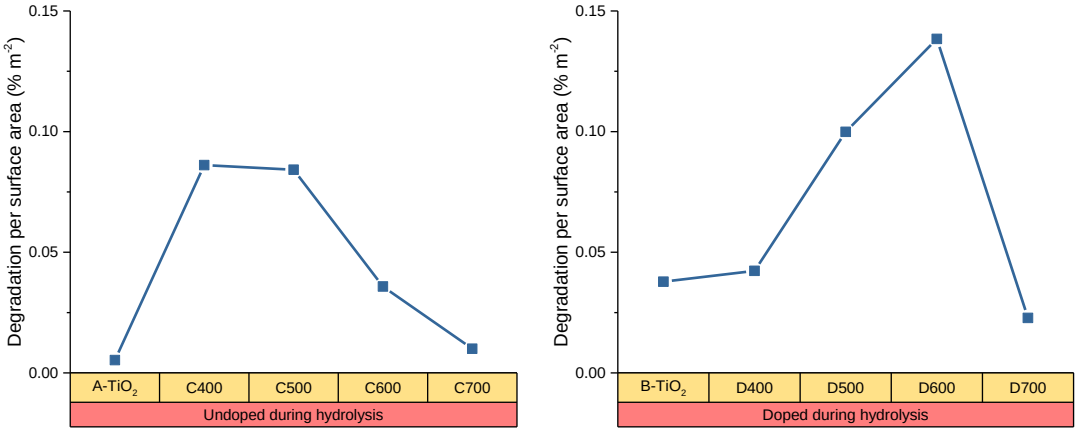

Figure S3.22 Degradation per surface area of synthesized samples.

Chapter 4: Hydrothermal synthesis of aqueous colloidally stable faceted highly active *N*-doped TiO_2 nanoparticles for wastewater treatment

4.1. Introduction

Titanium dioxide is one of most suitable materials for photocatalytic applications. High physical and chemical stability, combined with high photo-induced activities, have caused an ever-increasing interest on TiO_2 [4, 14, 55, 56]. Photocatalytic degradation of pollutants [3], artificial photosynthesis [7], superhydrophylic and self-cleaning surfaces [127], photo-induced disinfection [128], and medical applications such as drug delivery and anti-cancer materials [129] are some of the usages of TiO_2 nanoparticles. Focus of many of the studies have been on the synthesis of large surface area TiO_2, *e.g.* nanoparticles, that lead to higher rate or intensity of photo-induced phenomenon [14]. Phase composition, morphology, and particle size distribution are some of the other factors that affect the final properties of TiO_2 nanoparticles.

Studies have shown that some facets of TiO_2, such as (001), are more active than others, therefore if the synthesized nanoparticles have more of these facets (*e.g.* cubic shape), photocatalytic activity of the product would increase [21]. Moreover, it has been shown that oxidation and reduction happen on separate facets of TiO_2 [130]. Therefore, it is crucial for the synthesis procedure to be designed to suit the application of product (*e.g.* oxidation of pollutants or reduction of CO_2 in artificial photosynthesis). Regarding phase composition, titanium dioxide has three naturally accruing polymorphs: rutile, anatase and brookite. Amongst these polymorphs, anatase has been shown to be a more suitable choice for photocatalytic purposes [18, 59].

Large band-gap is one of the disadvantages of TiO_2, because it restricts the photocatalytic activity window to the UV region of light spectrum [2]. One of the main methods of inducing visible-light photo-activity in TiO_2 is doping with transition metal cations such as Fe, Cr and V [131-133], or non-metal anions like N, C, F and S [134-136]. Doping with non-metal anions in general, has been shown to have a more positive effect on visible-light photocatalytic activity of TiO_2 nanoparticles; with N having the highest potential to increase visible-light photocatalytic [2, 128].

Methods of synthesis of TiO_2 nanoparticles could be classified in two categories, namely physical and chemical methods. Chemical methods offer a more precise control over size, shape and particle size distribution [14]. Nanoparticles of TiO_2 has been synthesized using various wet chemical methods such as sol-gel [137], hydrothermal [138], solvothermal [139] and pyrolysis [140]. While sol-gel method offers a facile synthesis route, due to the required calcination step, the final product often forms large agglomerations, which reduces the available surface area. Additionally, this technique does not provide easy means of controlling shape and particle size distribution compared to other wet chemical methods [14]. In contrast, hydrothermal and solvothermal methods of synthesis, use surfactants that control the growth and allow production of desirable shapes and morphologies [21]. Shape control is specifically important in photocatalysis-based functions, because (001) facets of anatase are shown to perform remarkably better in pollutant degradation, compared to more thermodynamically stable (101) facets [141, 142].

There have been reports of the synthesis of TiO_2 nanocubes, and nanorods with dominant (001) facet using the hydrothermal method. It has been shown that the presence of F^- ions in the synthesis medium, impedes the growth of high energy (001)

facets, causing the growth to happen on (101) planes, which results in cubic or plate shaped nanoparticles, with high percentage of (001) facets [31, 143, 144].

Hazardousness of fluorides to the environment, plus low colloidal stability of hydrothermally synthesized nanoparticles, which is caused by agglomeration, has caused a shift towards more environmentally friendly organic surfactants, which do not necessarily dissolve in water. In contrast, solvothermal method uses organic surfactants dissolved in organic solvents. Surfactants react with different facets of TiO_2, allowing selective anisotropic growth of nanoparticle. Anatase nanoparticles have been synthesized with desired shape and size, by solvothermal technique, using oleic acid and oleylamine [35, 145]. However, in most cases, nanoparticles that are produced using solvothermal method are only dispersible in non-aqueous solvents such as toluene or hexane, which is problematic for their applications in wastewater treatment. *N*-doped anatase, rutile and brookite nanoparticles, with desired shape have been synthesized using different nitrogen sources such as triethylamine, triethanolamine, and urea [80, 93, 146-148].

Colloidal dispersion of TiO_2 nanoparticles is shown to improve their photocatalytic performance removing pollutants from water, relative to nanoparticles coated on a substrate [149, 150], and facilitates separation of the catalyst when the treatment is finished [151]. Colloidal stability of TiO_2 nanoparticles is also important in medicinal application, since agglomeration of nanoparticles severely impairs their function [152], and the nanoparticles must be dispersed in a biocompatible solvent [153]. However, to the best of our knowledge, there has not been a report on synthesis of aqueous colloidally stable *N*-doped TiO_2 nanoparticles, with control over size and morphology. There are reports of dispersing already synthesized and dried powders, by surface modification using polymers such as polyethylene glycol, but specially in

photocatalytic applications, the polymer would be degraded by the photocatalyst, causing loss of colloidal stability, or reduce, if not totally eliminate photocatalytic activity [34, 154, 155].

In this chapter, a systematic approach on synthesis of *N*-doped TiO_2 nanoparticles using a modified solvothermal method is reported. Aqueous colloidally stable cubic *N*-doped TiO_2 nanoparticles, were synthesized using triethylamine as both the surfactant, and the nitrogen source.

4.2. EXPERIMENTAL SECTION

Titanium tetraisopropoxide (TTIP), triethylamine (TEA), triethanolamine (TEOA), urea, phenol, chlorophenol, and pentachlorophenol were purchased from Sigma-Aldrich at the highest quality and were used without further purification. Deionized (DI, resistance >18MΩ) water was used throughout.

4.2.1. Synthesis of *N*-doped TiO_2 nanoparticles

In a typical synthesis, appropriate amount of nitrogen source (i.e. TEA, TEOA or urea), was mixed with 50 mL of a 0.5 M solution of TTIP in anhydrous ethanol. Different Ti: N molar ratios of 1:0.5 to 1:5 were utilized. This solution was transferred into a glass beaker and was placed inside a 200 mL stainless steel autoclave. 30 mL anhydrous ethanol and 1.8 mL of water were poured into the gap between the glass beaker and the autoclave. At this point the autoclave was closed and placed inside a heating mantle. The solution was heated at 160 °C or 200 °C for 24 hours without further stirring. The yellowish white precipitates were separated by centrifuging at 6,000 RCF[4], then washed three times with anhydrous ethanol by centrifuging and decantation of supernatant liquid. After final centrifuging, DI water was added to the

[4] Relative centrifugal force

washed precipitate and the suspension was sonicated for 1 hour. Synthesis parameters of all samples are listed in Table 4.1. To perform some of the characterization methods, and for purpose of measuring photocatalytic activity of the samples, colloidal samples were set to dry at room temperature, and the remaining powder was collected for further use.

4.2.2. Characterization of synthesized nanoparticle

Synthesized nanoparticles were characterized using a variety of characterization methods. Crystalline structure and phase was determined by X-ray diffraction (XRD), using a PANalytical Empyrean X-ray diffractometer and the results were analysed using HighScore Plus 4.1 software. A Joel JEM 1400 electron microscope was utilized to obtain transmission electron microscopy (TEM) images of the synthesized nanoparticles. TEM samples prepared by dropping a dilute aqueous suspension of nanoparticles on formvar TEM grids, followed by air drying. Diffuse reflectance measurements were performed using a Lambda 1050 ultraviolet-visible (UV-vis) spectrometer, with integrating sphere accessory. Omicron & Leybold MAX200 spectrometer was utilized for X-ray photo-electron spectroscopy (XPS) measurements to investigate the type and quantity of nitrogen species on the surface layer of nanoparticles; and XPSPeak 4.1 software was used to analyse the results.

4.2.3. Photocatalytic activity measurements

Visible-light photocatalytic activity of the synthesized nanoparticles was measured by photocatalytic degradation of 4-chlorophenol and pentachlorophenol (PCP). The photocatalytic reactions were performed under a 300 W Cermax Xe arc lamp (PE300BUV). UV light was filtered using a PIXELTEQ UV-IR (~390/740nm) filter, which was mounted under the lamp. For each experiment, 200 mL of 20 ppm solution of 4-chlorophenol in DI water was made, and a sample was taken from this solution,

followed by addition of 0.1 g of dried synthesized nanoparticles. This mixture was stirred for 15 min in the dark, and a sample was collected at this point. Afterwards, the reaction was carried out under illumination for 2 hours, while aliquots were being taken in time intervals. Each aliquot was centrifuged at 18,000 RCF, and the supernatant liquid was examined using UV-vis spectroscopy. This data was analysed to determine the amount of remaining pollutant, and consequently determine the progress of photocatalytic degradation over time. For Degradation of PCP, 7.5 mmol of PCP was dissolved in 50 mL of methanol. This solution was then used to make 20 ppm solution of PCP in water, and catalyst was added to this solution to reach catalyst concentration of 500 ppm. After illumination, aliquots were collected at 30 min intervals. The procedure after this is like that of degradation of 4-chlorophenol.

Table 4.1. List of Synthesized samples, their nitrogen source, synthesis temperature, and Ti: N ratio

N-Source	Sample name	Ti: N Ratio	Temperature
Undoped	TiO2160	NA	160
	TiO2200	NA	200
Triethanolamine	TEOA160_0.5	1:1/2	160
	TEOA160_1	1:1	160
	TEAO200_0.5	1:1/2	200
	TEAO200_1	1:1	200
	TEAO200_2	1:2	200
	TEAO200_5	1:5	200
Urea	UREA160_0.5	1:1/2	160
	UREA160_1	1:1	160
	UREA160_2	1:2	160
	UREA160_5	1:5	160
	UREA200_0.5	1:1/2	200
	UREA200_1	1:1	200
	UREA200_2	1:2	200
	UREA200_5	1:5	200
Triethylamine	TEA160_0.5	1:1/2	160
	TEA160_1	1:1	160
	TEA160_2	1:2	160
	TEA160_5	1:5	160
	TEA200_0.5	1:1/2	200
	TEA200_1	1:1	200
	TEA200_2	1:2	200
	TEA200_5	1:5	200

4.3. RESULTS AND DISCUSSION

As discussed in the experimental section, all samples were dispersed in water after synthesis. The suspensions were kept in a dark place, without motion for 6 months, after which precipitation was observed for some samples; however, TEA160 samples, and specifically TEA160_2, demonstrated great colloidal stability as can be seen in Figure 4.1.

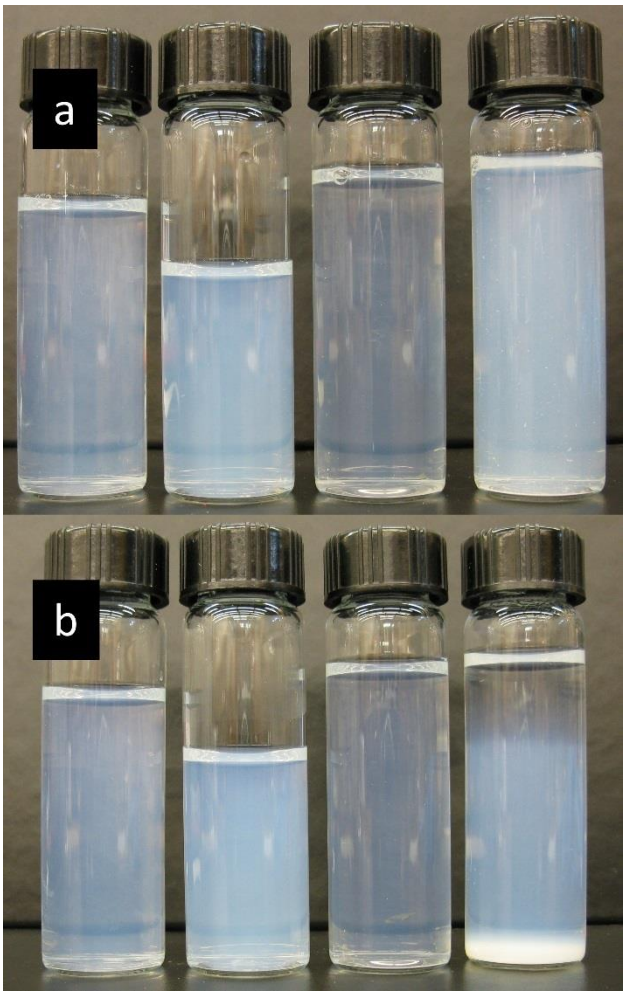

Figure 4.1 Image of TEA160 samples, a) as synthesized, b) after 6 months of storage, from right to left: TEA160_0.5, TEA160_1, TEA160_2, TEA160_5.

Figure 4.2 displays XRD pattern of samples synthesized at 200 °C with Ti: N ratio of 1:1, and an undoped sample. XRD results show that the synthesized samples are anatase,

with average crystallite size between 9.3 nm (TEA sample) to 10.5 nm (urea sample), which was measured using the Debye-Scherrer equation. While the crystallite size, obtained from XRD, does not vary drastically based on the precursors, the crystallinity is altered by this factor. By comparing the intensity of the main XRD peak of samples, it can be concluded that presence of urea increases crystallinity, while triethylamine and triethanolamine decrease crystallinity, with the former affecting the crystallinity less than the later. For the full set of results, please see the supporting information.

The increase of the crystallinity in urea samples could be due to hydrolysis of urea in high temperatures of synthesis, which leads to formation of ammonia and increase of the pH. Synthesis in alkaline conditions is shown to enhance the crystallinity of TiO_2 nanoparticles and increase the particle size [156]. The crystallinity increases and the average crystallite size decreases as the amount of urea is increased gradually in the synthesis step regardless of the synthesis temperature.

Figure 4.3 displays XRD pattern of TEAO200 samples, which shows that as TEOA concentration increases crystallinity decreases. This could be due to formation of stable Ti(IV)/TEOA complexes that delay hydrolysis and nucleation of TiO_2 resulting in lower crystallinity, especially in higher Ti: TEOA ratios [157].

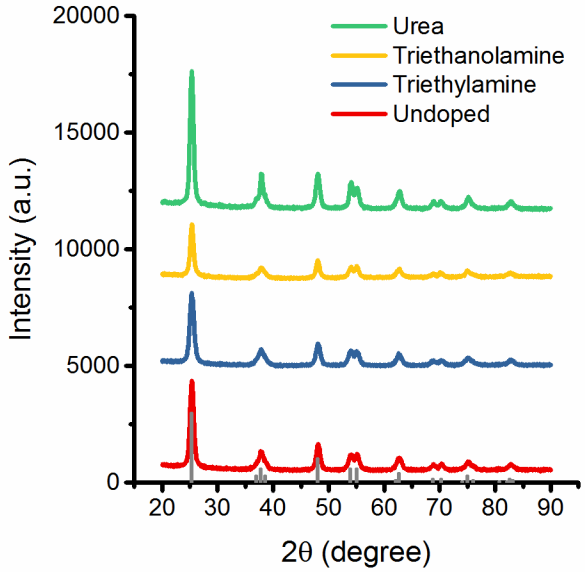

Figure 4.2. XRD pattern of synthesized samples with different nitrogen sources, plus reference peaks of anatase (PDF code 00-004-0477). All samples are synthesized at 200 °C and Ti: N ratio (if applicable) is 1:1.

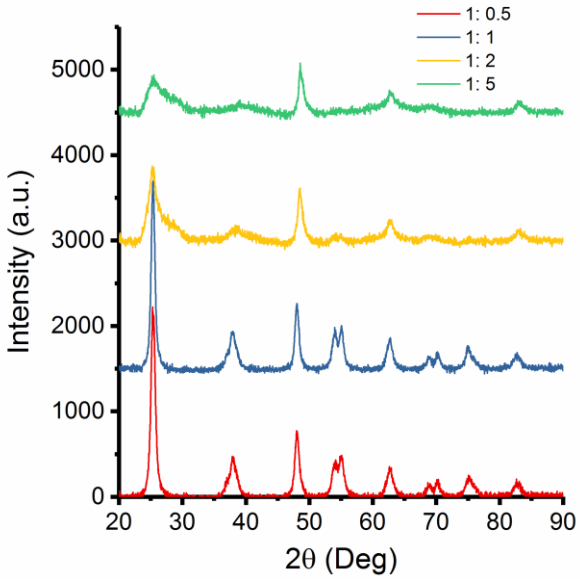

Figure 4.3. XRD pattern of TEOA200 samples, made with different ratios of Ti: TEOA, at 200 °C.

Moreover, in samples with Ti: TEOA ratios of 1:2 and 1:5, the ratio of intensities of peaks of (002) to (101) planes differs from the standard ratio of 0.28 to 0.7 for sample

TEOA200_2, and 1.25 for TEOA200_5, which could lead to presence of anisotropy in shape of these samples; this assumption was later found to be true

\using electron microscopy. It is noteworthy that the same ratio was found to be 0.27 for undoped sample TiO_2_200, which is very close to the standard data of undoped anatase TiO_2.

Compared to the undoped TiO_2 sample, TEA samples have a slightly lower crystallinity, and smaller average crystallite size. The crystallinity is highest in TEA160_5 and lowest in TEA160_2. The ratio of peak intensities of (002) to (101) planes varies as the amount of TEA changes in the samples, with TEA160_2 having the highest ratio of 0.42, and consequently the highest anisotropy in shape compared to the standard TiO_2 sample. The same behaviour was observed in samples synthesized at 200 °C. The average crystallite size is measured to be slightly smaller in these samples relative to the samples synthesized at 160 °C. The reason for this could be formation of larger number of nuclei in higher temperatures of synthesis, which leads to smaller average crystallite size.

Transmission electron microscopy was used to determine the size, particle size distribution and shape of the synthesized nanoparticles. Figure 4.4 shows TEM images of undoped TiO_2 samples, synthesized at 160 °C and 200 °C. Although the synthesized particles have various shapes, the majority seems to have an elongated octahedral morphology. While the average crystallite size does not change drastically as the hydrothermal treatment temperature increase from 160 °C to 200 °C, particle size distribution increases noticeably from a range of 13-89 nm to 9-141 nm.

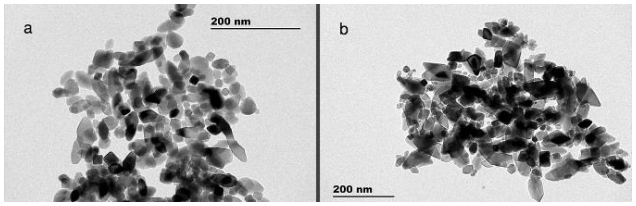

Figure 4.4. TEM images of undoped samples, a) $TiO_2$160 and b) $TiO_2$200. For particle size distribution charts see the supporting information.

Figure 4.5. displays the TEM images of TEA160 samples. The images show that presence of TEA during the synthesis, facilitates the formation of cubic nanoparticles, decreases crystallite size, and noticeably decreases the particle size distribution relative to undoped samples. Among TEA samples, TEA160_2 has the narrowest particle size distribution, and is comprised of more cubic particles than other samples, especially the ones made at 160 °C. Synthesis at 200 °C appears to promote formation of cubic particles at a higher extent than synthesis at 160 °C. However, particle size distribution as seen in Figure 4.6 has been increased relative to 160 °C samples.

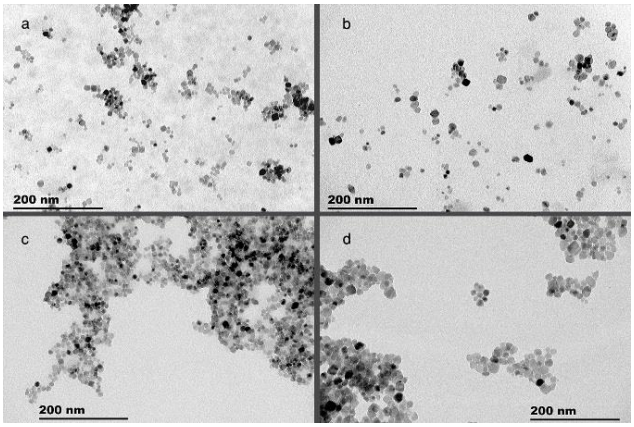

Figure 4.5. TEM image of samples synthesized at 160 °C with Ti: TEA ratios of, a) 1:0.5, b) 1:1, c) 1:2 and d) 1:5.

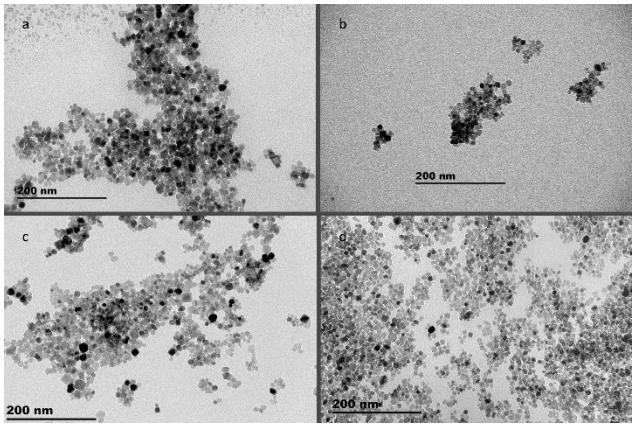

Figure 4.6. TEM image of TEA samples synthesized at 200 °C with Ti: TEA ratios of, a) 1:0.5, b) 1:1, c) 1:2 and d) 1:5.

Effect of addition of urea during the synthesis on morphology and size could be seen in Figure 4.7. Size decreases and particle size distribution gets narrower when urea is added, however at higher ratios of Ti: Urea, particularly 1:5, large particles form, and both the average particle size and particle size distribution increase. Moreover, one can conclude that presence of urea during synthesis, causes formation of octahedral shaped nanoparticles. Synthesis temperature does not seem to affect shape and morphology of urea samples considerably, however, specifically in higher ratios of Ti: urea, it seems that the presence of urea lowers the number of extremely large (<50 nm) nanoparticles.

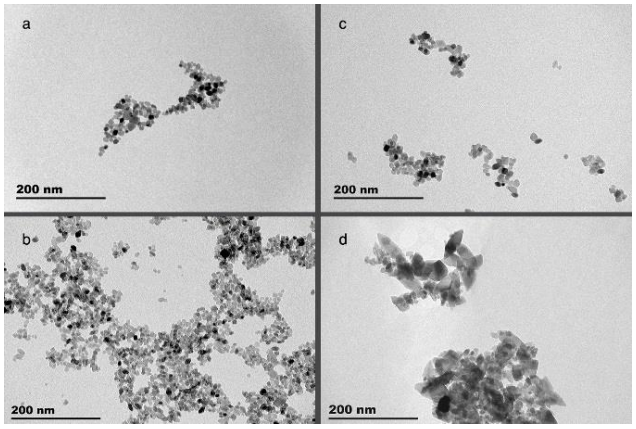

Figure 4.7. TEM image of Urea160 samples synthesized at 160 °C with Ti: Urea ratios of, a) 1:0.5, b) 1:1, c) 1:2 and d) 1:5.

Figure 4.8 shows TEM images of TEOA 160 samples. The images display an amorphous phase, which could be indicative of hydrolysis step of formation of TiO_2, in which crystalline particles have not yet formed, but there exist amorphous agglomerates that given time or temperature could grow into crystalline structures. This is in correlation with the XRD results, which state the lack of crystallinity of TEAO160 samples.

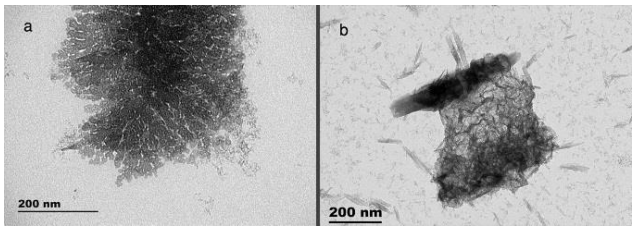

Figure 4.8. TEM image of TEOA160 samples synthesized at 160 °C with Ti: TEOA ratios of, a) 1:0.5 and b) 1:1

Increasing the synthesis temperature, however, seems to induce formation of different morphologies, regarding the Ti: TEOA ratio as shown in Figure 4.9. At low TEOA contents, synthesis results in formation of nanoparticles, and as the ratio of TEAO increases, other morphologies start to form, and number of nanoparticles decrease, until the Ti: TEOA ratio of 1:5, at which no nanoparticles where observed in TEM images.

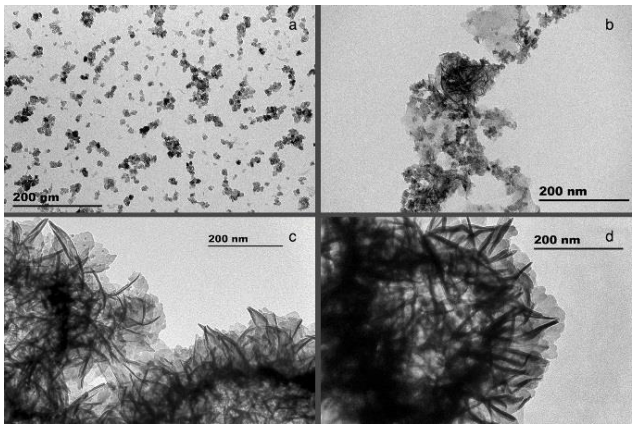

Figure 4.9 TEM image of TEOA200 samples synthesized at 200 °C with Ti: TEOA ratios of, a) 1:0.5, b) 1:1, c) 1:2, and d)1:5.

To further understand the morphology of TEOA200_2 and TEOA200_5, SEM imaging was performed on these samples. SEM images of TEOA200_5 are shown in Figure 4.10. combining SEM and TEM images, one could conclude that synthesis has resulted in hollow spheres, formed by arrangements of TiO_2 plates. This also follows XRD data, which showed anisotropy compared to standard TiO_2 peaks. The Morphology of TEOA samples makes them an excellent candidate for being coated on substrates to provide ample surface area.

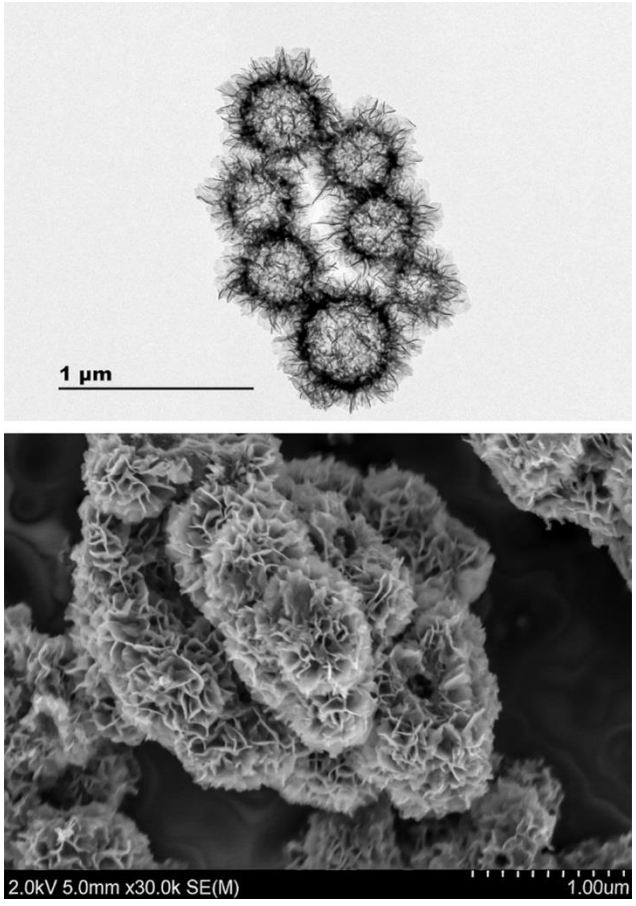

Figure 4.10 SEM image of sample TEOA200_5.

Infrared spectroscopy was used to study the presence of organic species on the synthesized, dried nanopowders. Figure 4.11 shows the FTIR spectra of TEA200 samples. The large peaks around 770 cm^{-1} and 500 cm^{-1} are the characteristic bands of anatase, which indicates Ti–O and Ti–O–Ti in TiO_4^{4-} octahedra [158]. The band at 1630 cm^{-1} is the bending of water molecules, which shows presence of adsorbed molecular water on the synthesized nanoparticles. Another adsorbed molecule is CO_2, which attributes to the peak at 2345 cm^{-1}. Peaks at 905 cm^{-1}, 1385 cm^{-1}, 2860 cm^{-1}, and 2930 cm^{-1} are the C–H bands of ethyl groups, and the peak at 1050 cm^{-1} is C–N stretch, which together indicate the presence of small amounts of triethylamine or ethanol from the synthesis step. The fact that C–H bands become more apparent as the amount of triethylamine in the synthesis increases indicates that C–H peaks come from residual triethylamine.

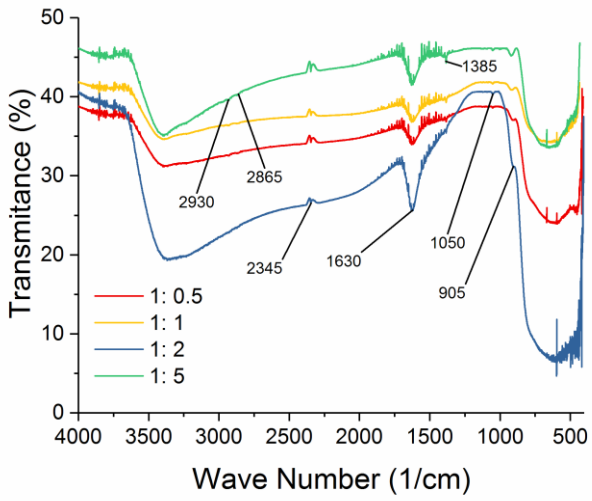

Figure 4.11. FTIR spectra of TEA200 samples.

The peak at 1120 comes from the C–N stretch, and the peaks at 2860 cm^{-1}, and 2930 cm^{-1} are the C–H bands of ethyl groups. Since both amines used in this research are tertiary amines, no N-H peak could be observed, however, a strong, broad peak could be

observed for triethanolamine samples in Figure 4.12, around 3400 cm^{-1}, representing O–H stretching.

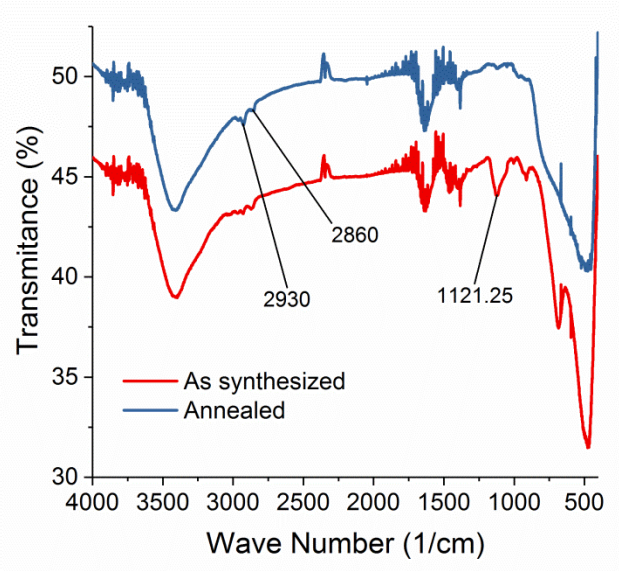

Figure 4.12 FTIR spectrum of TEAO200_5 sample before and after annealing.

To find out about the amount of doped nitrogen, and the type of nitrogen species on the synthesized nanoparticles, XPS was used. Figure 4.13 shows the N1s XPS spectra of TEA160 samples. The main nitrogen peak for these samples is located at 400.1 eV, which is a characteristic of *N*-doped TiO_2 samples prepared by wet chemical methods and is a result of NO_x (*i.e.* Ti–O–N–O) or NH_x species [26, 123]. XPS data of some samples also contain a peak at 401.8 eV that is caused by chemisorbed γ-N_2 species (*i.e.* Ti–O–N–N).

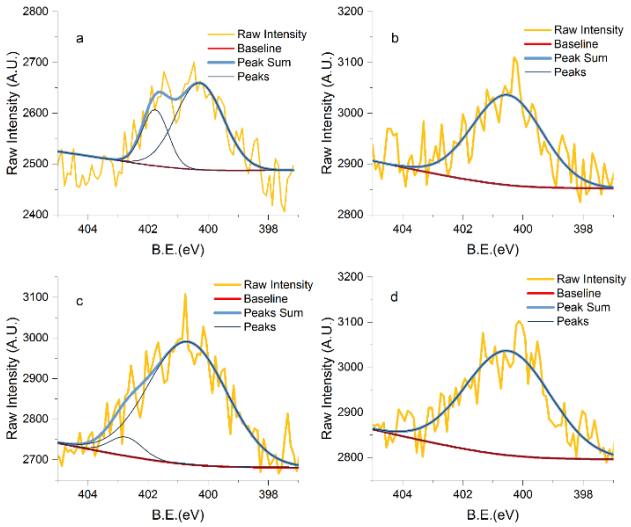

Figure 4.13 N1s XPS graph of TEA samples synthesized at 160 °C with different Ti: N ratios (a: 1: ½, b: 1:1, c: 1:2, d: 1:5).

To calculate the amount of doped nitrogen, the area under Ni 1s, and Ti 2p curves were measured by fitting the data using XPSPeak software. Background was determined using the Shirely method with 5 average points. Next, the calculated areas were corrected by dividing them by each element's relative sensitivity factor (0.42 for N1s, and 1.33 for Ti2p 3/2). The ratio between these, determines Ti: N ratio of each sample; the results of which are presented in Table 4.2. Amount of nitrogen in the sample initially increases as the nitrogen source concentration increases, however, sample TEA160_5 was shown to contain less nitrogen than TEA160_2

Table 4.2. calculated, and corrected areas of N1s and Ti2p peaks for each sample, and their respective Ti: N ratio

Sample	N1s area	Ti 2p 3/2 area	Ti: N ratio
35	458	68966	2.1
36	658	71461	2.9
37	1039	76854	4.3
38	733	70898	3.3

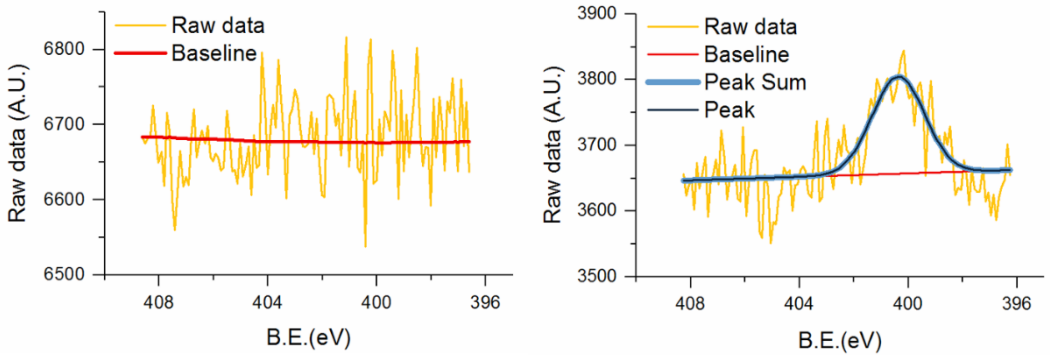

Figure 4.14 N1s XPS graph of Urea samples synthesized with Ti: N ratio of 1:5 at top: 160 °C and bottom 200 °C.

Figure 4.14 shows N1s XPS graph of samples UREA160_5 and UREA200_5. No nitrogen is doped into the sample made at 160 °C, as opposed to a doping ratio of 2.4 % for the sample made at 200 °C. Lack of doping at 160 °C, and lower doping ratio, compared to TEA samples, mean that doping with UREA needs to happen in higher temperatures, or with higher initial concentration of it.

Photocatalytic activity of synthesized samples was assessed by visible-light degradation of 4-chlorophenol. The process has been discussed in detail in the experimental section. UV-Vis spectra of collected samples could be found in supporting information. To calculate the remaining chlorophenol at each step, intensity of the absorption peak located at 225 nm of UV-Vis spectrum of aliquot samples were divided by the intensity of the same peak for the initial 4-chlorophenol solution.

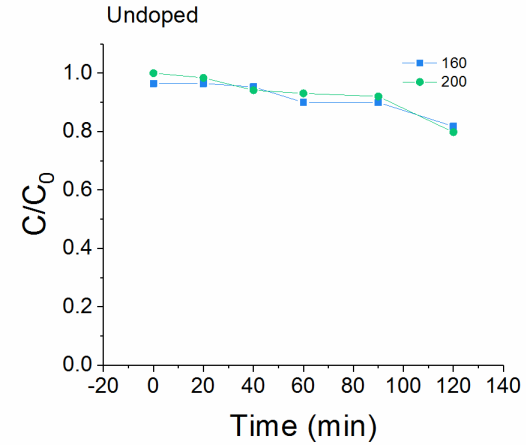

Figure 4.15 Visible-light photocatalytic degradation efficiency of 4-chlorophenol using synthesized undoped nanoparticles.

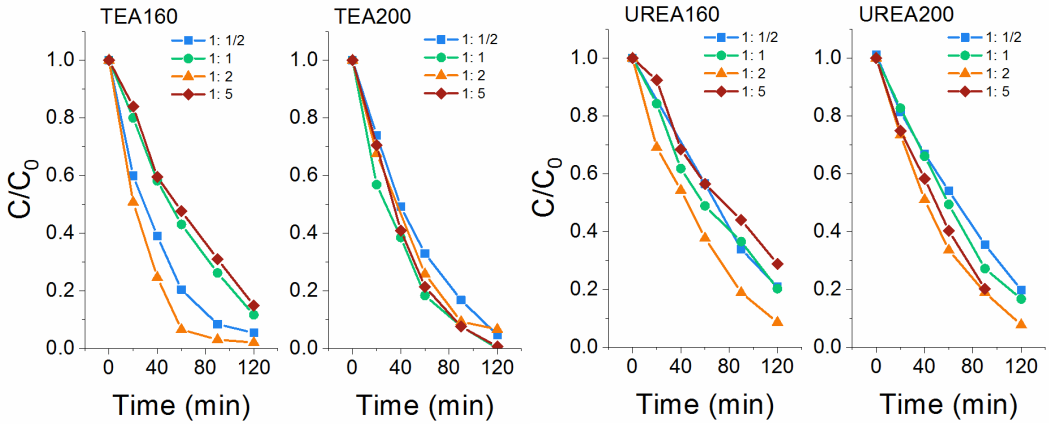

Figure 4.16 Visible-light photocatalytic degradation efficiency of 4-chlorophenol using *N*-doped nanoparticles, synthesized using TEA and urea.

The results show minute photocatalytic activity from the two undoped samples, regardless of their synthesis temperature, which demonstrates proper filtration of UV light by the applied UV filter as seen in Figure 4.15. Among synthesized samples, the ones made with TEA as the nitrogen source compound, show the highest photocatalytic activity as seen from Figure 4.16. Synthesis at 200 °C was showed to slightly decrease the activity of synthesized nanoparticles. TEA160_2 shows the highest degradation efficiency compared to all other samples and reached a degradation of 95% after 60 min.

The authors think that the reason for higher activity of TEA samples is cubic shape of these samples, which is shown to increase the photocatalytic activity of TiO_2 nanoparticles, together with their smaller average size, which leads to higher surface area. Among TEA samples, TEA160_2, has the lowest average size, smallest size distribution, and the particles are mainly cubic. Size distribution histograms for TEA160 and TEA200 samples are shown in supporting information.

It's worth mentioning that no photocatalytic activity was observed for TEOA160 samples, which is in coordination with XRD and TEM results, which show a lack of formation of a crystalline phase. However, TEOA200 samples show visible-light photocatalytic activity, and the activity decreases when the amount of TEOA mixed with precursors increases. In addition, contrary to the trend of other samples, which show high activity in the first 30 min of experiment, for TEOA200 samples, activity is minimal for the first 30-40 min, and after that the rate of change increases and almost stays constant for the rest of the experiment. The authors think that the initial low activity of these samples, is due to presence of excess amounts of TEOA on the surface, and that most of produced OH radicals are being used to degrade this initial layer, after which the particles start degrading the pollutants. The rate does not slow down like other samples simply because concentration of 4-chlorophenol stays relatively higher than other samples, at the interval of 90-120 min, therefore there is still enough pollutant available for degradation.

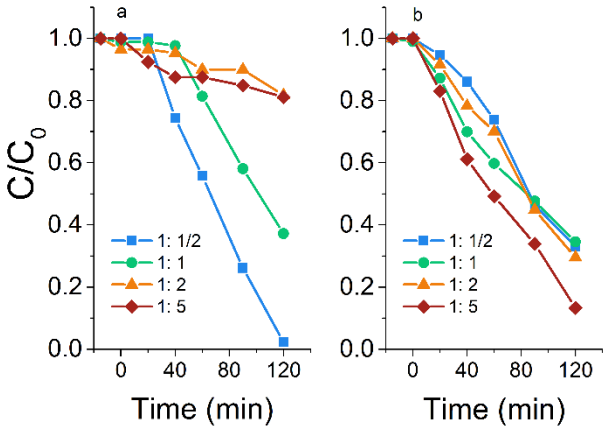

Figure 4.17 Visible-light photocatalytic degradation of TEOA200 samples, for degradation of 4-chlorophenol. a: before annealing, after annealing at 300 °C for 2 hours.

To investigate this issue better, TEOA200 samples were annealed at 300 °C for 2 hours. Next, they were analysed by FTIR spectroscopy, the results of which are shown in Figure 4.12; and their photocatalytic performance was assessed like other samples, and the results are shown in Figure 4.17. The FTIR spectrum of the annealed sample reveals significant decrease in intensity of the peak at 1120 cm^{-1}, which as discussed above, arises from C–N stretch, and therefore is a sign of removal of TEOA. First noticeable thing about annealed samples is increase of photocatalytic activity during the first 40 min of experiment, compared to very low, activity before annealing; which is a result of removal of excess TEOA. After annealing, photocatalytic activity of TEAO200_0.5 and TEAO200_1 decreased from 87% and 63% degradation at 120 min, to 67% and 53% respectively, which could be because of the decrease of surface area due to size growth that happens during annealing. On the contrary, photocatalytic activity of TEOA200_2, and TEOA200_5 improved from 19% for both samples, to degradation efficiency of 71% and 87% for TEOA200_2 and TEOA200_5 respectively. SEM images of these two samples show no visible change in morphology before and after annealing, however, they

showed higher crystallinity based on XRD. Removal of excess TEOA, and increase of crystallinity, while not affecting surface area, are the reasons annealing has caused an improve in activity of these samples. However, even after annealing, TEOA200_2 sample still shows lower photocatalytic activity than that of samples synthesized with other nitrogen source compounds. This could be due to less surface area, provided by this sample, due to its 2D morphology (a collection of ultra-thin TiO_2 pallets) relative to others, which are nanoparticles.

Additionally, TEA160_2 nanoparticles, which performed highest on degradation of 4-chlorophenol were used to degrade phenol, and PCP solutions. The results are shown in Figure 4.18. Complete degradation of a 100-ppm solution of phenol was achieved using this sample after 90 minutes. While it took longer to degrade PCP compared to 4-chlorophenol, since PCP is a harder molecule to break photocatalytically due to having higher number of chlorides. Whoever, A degradation efficiency of 97% was achieved at 180 min, which is a great visible-light performance, shows the superb capability of the synthesized nanoparticles to degrade on of the toughest pollutant molecules.

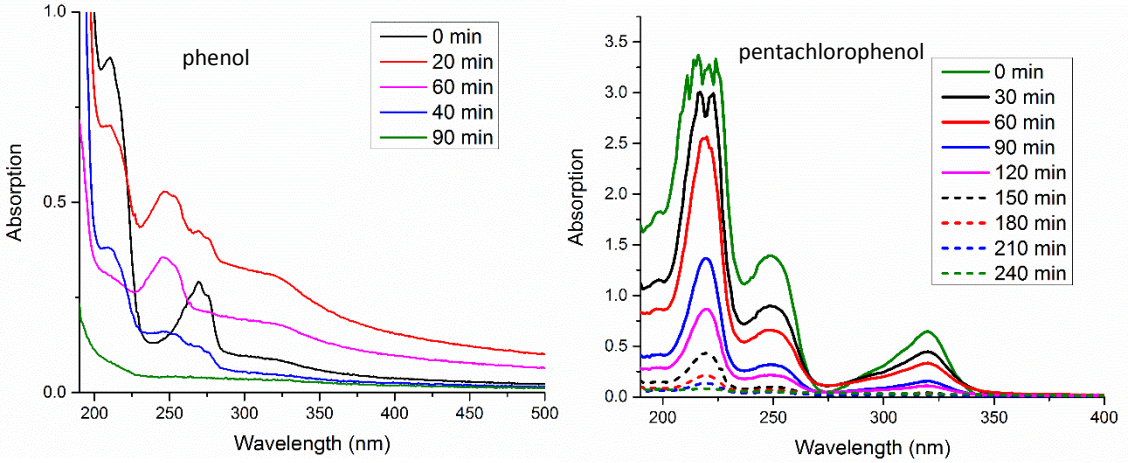

Figure 4.18 UV-Vis spectrum of initial phenol, and PCP solutions, and aliquots taken consecutively from them after illumination.

One of the concerns, involving photocatalytic pollutant degradation, is de-activation by fouling and other processes, the former which happens by physical adsorption of pollutant molecules, or reaction intermediates on catalyst, which severely lowers photocatalytic activity, ultimately rendering the catalyst inactive. To study this issue in case of this research's synthesized nanoparticles, visible-light photocatalysis degradation of 4-chlorophenol, using TEA160_2 sample was performed for 5 consecutive runs. Each trial was performed for 2 hours, taking aliquots every 30 min. After each trial, catalyst nanoparticles were collected using a centrifuge, and reused for the next trial. The results of these trials are shown in Figure 4.19. All five trials ended with complete degradation of 4-chlorophenol, however, degradation efficiency, especially during the first 60 min, is gradually decreasing after each trial. This could be due to loss of nanoparticles, during the collection step between each trial. Since each trial ended in complete degradation of the initial 4-chlorophenol, we conclude that fouling has not happened after 5 runs.

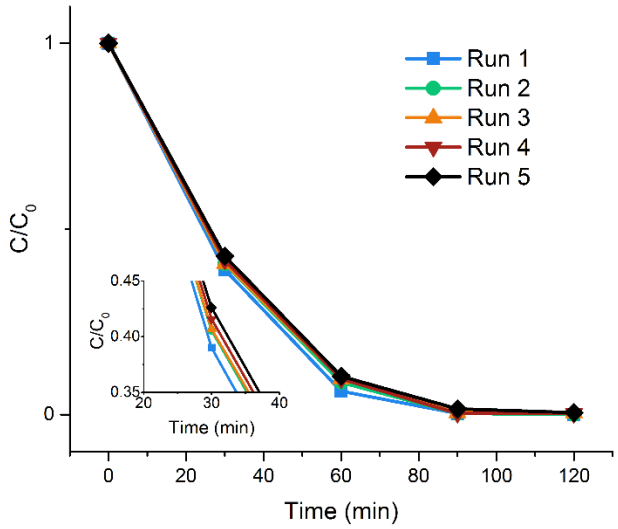

Figure 4.19 5 consecutive trials on Visible-light photocatalytic degradation of 20 ppm 4-chlorophenol, using retrieved TEA200_2 sample as the photocatalyst.

One of the challenges of industry and municipalities, which is effectiveness of the photocatalyst treating wastewater samples containing multiple types of pollutants. Since all the photocatalytic activity measurements in the dissertation have so far been performed using a single type of pollutant, a sample was obtained from sewage of Vancouver, British Columbia, and sample TEA160_2 was used to treat it. The wastewater sample contained 5 ppm TOC[5] before treatment. After 60 minutes of treatment with the photocatalyst, no TOC was detected in the sample.

4.4. Conclusion

N-doped TiO_2 nanoparticles were synthesized using a facile hydrothermal synthesis method. Nitrogen source was added not only to induce doping and visible-light photocatalytic activity, but also to serve as a surfactant, altering the shape, size, and morphology of the nanoparticles. It was shown that addition of TEA produces aqueous colloidally stable cubic nanoparticles, and size of the nanoparticles decreases as amount of triethylamine increases. TEA:Ti ratio of 2:1 produced the narrowest size distribution, resulting in mostly cubic nanoparticles.

Using TEOA as nitrogen source resulted in production of pallet shaped TiO_2, arranged in a spherical, rose-like structure, in high TEAO concentrations and synthesis temperature of 200 °C. Addition of urea, as nitrogen source, results in larger nanoparticles, with a wider size distribution compared to TEA.

Photocatalytic activity of the synthesized nanoparticles was assessed by visible-light degradation of 4-chlorophenol. Urea samples synthesized at 160 °C showed lower

[5] Total Organic Carbon

activity compared to 200 °C, which is due to lack of incorporation of nitrogen from urea at lower temperatures. Among samples, TEA samples show the highest degradation efficiency, achieving 98% degradation for a 20-ppm solution of 4-chlorophenol, with 500 ppm loading of catalyst. TEOA samples only showed lack of activity during the first 30 min of reaction, which was shown is due to presence of the remaining TEOA, which does not come off after washing. These samples show good activity after annealing under flow of air, which removes the remaining TEOA.

Visible-light photocatalytic efficiency of the best performing sample (TEA: Ti ratio of 2:1, 160 °C synthesis temperature) for degradation of other pollutants was also measured. Resulting in total degradation of phenol, from a 100-ppm solution after 90 min, and 98% removal of PCP, from a 20-ppm solution after 180 min. Moreover, our results showed no sign of deactivation, in five consecutive photocatalytic reaction runs, reusing this sample to remove 4-chlorophenol from a 20-ppm solution. Additionally, a sample of municipal wastewater was treated using the synthesized nanoparticles. The results showed total elimination of TOC from the sample after 60 minutes of treatment.

Chapter 5: Conclusions and Future Work

5.1. Conclusions

This dissertation describes synthesis methods of titanium dioxide nanoparticles, both undoped and nitrogen-doped (*N*-doped), and application of the synthesized nanoparticles in wastewater treatment. The work is focused on enhancing visible-light photocatalytic activity of TiO_2 by altering the size, shape, morphology, and dopant concentration of synthesized nanoparticles. The synthesized *N*-doped TiO_2 nanoparticles were characterized using XRD, SEM, TEM, FTIR, UV-vis, and XPS; Moreover, the effects of synthesis conditions on photocatalytic activity of synthesized nanoparticles were compared by measuring their degradation efficiency on removal of methyl orange, phenol, 4-chlorophenol, and pentachlorophenol.

Chapter three discusses a facile, inexpensive sol-gel synthesis method to produce *N*-doped TiO_2 nanoparticles, using different doping techniques (wet chemical, or dry methods), and explains the effect of doping methods on physical, and photocatalytic properties of the nanoparticles. Visible-light degradation of methyl orange was used as a measure of photocatalytic activity of produced nanoparticles.

Chapter four focuses on hydrothermal synthesis of *N*-doped colloidally stable TiO_2 nanoparticles, and possibility of using the nitrogen source compounds to not only induce *N*-doping, but also to control size and size distribution, shape, morphology, and enhance colloidal stability of synthesized nanoparticles. To assess visible-light photocatalytic activity of the produced nanoparticles, phenol, 4-chlorophenol, and pentachlorophenol were used as pollutants and the results were used to discuss the effect of synthesis conditions on properties of nanoparticles, and how they influence photocatalytic activity.

The key findings and contributions of this work are:

5.1.1. Sol-gel synthesis of *N*-doped TiO_2 nanoparticles:

Nanoparticles were synthesized by conversion of titanium tetra-isopropoxide to peroxo titanate, followed by an annealing step. Different approaches of nitrogen doping were performed, comprised of wet chemical doping (i.e. addition of ammonium hydroxide to peroxo titanate), dry doping (i.e. annealing under ammonia flow), and a combination of both methods.

5.1.1.1. Effect of wet nitrogen doping on phase, crystallinity, crystallite size, and effective surface area of the nanoparticles

Using UV-vis spectroscopy, I showed that addition of ammonium hydroxide, during the synthesis, together with other precursors induces nitrogen doping. Non-ambient XRD patterns shows other effects of ammonium hydroxide on the synthesized nanoparticles. XRD patterns and BET measurement results, shows higher crystallinity, smaller (average) crystallite size (11 nm for doped vs 16 nm for undoped), and higher surface area (131.7 m^2/g for doped vs 77.6 m^2/g for undoped) for doped nanoparticles; plus, *N*-doping increases the thermal stability of anatase, rising the anatase/rutile transformation temperature from 530 °C to 635 °C. This is due to the larger unit cell of anatase, which creates less strain due to doping. Even after annealing at 750 °C, the *N*-doped sample was still mainly comprised of anatase.

5.1.1.2. Effect of nitrogen doping method on visible-light absorption

UV-Vis spectroscopy data shows *N*-doping methods decrease the band-gap of synthesized nanoparticles from 3.2 eV to 2.6 eV, causing an absorption increase at 475 nm wavelength. This data, combined with XPS results show that as the annealing temperature under ammonia flow increases, surface visible-light absorption intensity

increases due to raise of the doped nitrogen percentage. This change is visible as the colour of synthesized nanoparticles changes as the annealing temperature increases, from a pale yellow to bright yellow, light green, dark green, and finally black.

5.1.1.3. Effect of nitrogen doping method and parameters on nitrogen species doped in synthesized nanoparticles

The XPS results show that different doping techniques, and doping parameters, while all induce nitrogen doping, each create different nitrogen species; plus, as the doping temperature increases, nitrogen content increases (from 1.7% to 27.6%). Wet chemical methods induce doping by chemisorbed γ-N_2 species (i.e. Ti-O-N-N). Dry doping methods produce NO_x or NH_x species at lower annealing temperatures (400 °C and 500 °C), while doping in higher temperatures (600 °C and 700 °C) produce substitutional nitrogen and chemisorbed γ-N_2 species. Moreover, XPS results show that increased nitrogen content at higher doping temperatures, result in formation of Ti^{3+} species and oxygen vacancies, to maintain charge neutrality. The author thinks formation of Ti^{3+} and oxygen vacancies changes the colour of the nanoparticles to black.

5.1.1.4. Effect of synthesis and doping conditions, and properties of synthesized nanoparticles on their visible photocatalytic activity

Photocatalytic degradation of methyl orange was used to determine the activity of synthesized nanoparticles. Several factors affect the degradation efficiency of the synthesized nanoparticles; among them, surface area and doping levels have the most significant effect. It was shown that wet chemically doped nanoparticles have the highest photocatalytic efficiency, and that the efficiency decreases as dry doping temperature increases. Increasing the doping temperature results in more visible-light absorption, however, it increases particle size and lowers available surface. Using degradation per

surface area, it was shown that photocatalytic activity initially increases as the nitrogen concentration increases, followed by a decline of activity at higher doping temperatures. However, it was shown that surface area affects the photocatalytic activity more intensely than dopant concentration; therefore, a sample with less dopant concentration, but larger surface area is a better photocatalyst.

5.1.2. Hydrothermal synthesis of *N*-doped TiO_2 nanoparticles

5.1.2.1. Effect of nitrogen source compound on shape of synthesized nanoparticles

Hydrothermal synthesis was used to produce ultra-small *N*-doped TiO_2 nanoparticles with high surface area, and desirable shape. Nitrogen source compounds used in the synthesis also served as surfactants to control shape of the nanoparticles. It was shown that TEA produces cubic nanoparticles, urea produces octahedron nanoparticles, and presence of TEOA results in formation of TiO_2 pallets, joined together to form spherical structures. Undoped samples produced with the same procedure in absence of nitrogen source compounds had octahedron shape.

5.1.2.2. Effect of synthesis temperature and precursors on size, size distribution and colloidal stability of synthesized nanoparticles

Nanoparticles synthesized with use of TEA have the smallest size, narrowest size distribution, and highest colloidal stability. Narrowest size distribution belonged to samples synthesized with a TEA:Ti ratio of 2:1. Moreover, it was shown that increasing synthesis temperature from 160 °C to 200 °C decreases the size distribution in TEA samples. In case of TEOA samples, at 160 °C formation of crystallite size was not observed; and at 200 °C as the concentration of TEOA increases, morphology changes from nanoparticles to 3D arranged pallets. When using urea as nitrogen source

compound, as the amount of urea increases, size and size distribution both increase. Both TEOA and urea samples have low colloidal stability, which is due to their large particle size and morphology.

5.1.2.3. Effect of synthesis conditions on visible-light photocatalytic activity of synthesized nanoparticles

Visible-light photocatalytic degradation of4-chlorophenol by synthesized nanoparticles was used to assess photocatalytic efficiency of the synthesized nanoparticles. TEA samples showed the highest efficiency among all samples, which among other factors, is mainly due to their cubic shape, small size, and narrow size distribution. For these reasons the samples made at 160 °C and 200 °C with TEA:Ti ratio of 2:1, which are mainly comprised of cubic nanoparticles, with 10 nm average particle size, and small size distribution have the highest efficiency among other TEA samples.

Additionally, it was shown for TEOA samples, made at 200 °C as the amount of TEOA increases, efficiency decreases. This is due to lower surface area, compared to nanopowders, and presence of contaminating TEOA on the surface.

5.1.2.4. Photocatalytic efficiency of synthesized nanoparticles for degradation of different phenolic compounds

Sample TEA160_2, which is the best performing sample in photocatalytic degradation of 4-chlrophenol was used to degrade phenol and PCP. The sample showed excellent degradation efficiency in case of phenol. 200 mg of dried sample was added to 200 mL of a 100-ppm phenol solution, and after 40 min of visible-light illumination, no peak of phenol was observed in UV-Vis of the solution. This is a major advancement in photocatalytic activity, compared to results obtained by other research articles. In case of PCP, 97% removal was reported after 180 min, and no peak of PCP could be detected

after 240 min; which considering the recalcitrant nature of this pollutant, is a very good result.

5.1.2.5. Fouling of synthesized nanoparticle photocatalysts

Fouling is one of the mechanisms of catalyst decay, which is a concern specifically when dealing with photocatalysts. To study the fouling behaviour of the synthesized nanoparticles, sample TEA160_2, which is the best performing sample was utilized to degrade 4-chlorophenol. Photocatalytic degradation tests were performed 10 times, using the same sample, which was collected using a centrifuge after each run. The results show that after 120 min, all runs ended with complete degradation of 4-chlorophenol, without showing any signs of fouling. However, the removal rate at the first 30 min, which is the period with the highest removal rate, were decreases about 8%. The authors think this is due to loss of particles, between runs, doing centrifuging and transferring steps.

5.2. Future work

This research has resulted in a better understanding of the effects doping technique and parameters and obtaining a facile synthesis method of *N*-doped TiO_2 nanoparticles, capable of controlling size, shape, morphology, that produces highly active and efficient photocatalysts. However, this research work could still be improved by further studies:

- Immobilization of the synthesized nanoparticles, and study on their application within a photocatalytic reactor.
- Co-doping with other dopants, including metals such as Fe, Ni, and Cu, or non-metals such as F, C, and S, and study their combined effect on properties and photocatalytic activity of synthesized nanoparticles.

- Study other photocatalytic applications of TiO_2 nanoparticles, specifically reduction of CO_2 to fuel (solar fuel conversion), and water splitting to produce H_2.
- Optimizing the conditions of photocatalytic reactions such as catalyst loading, pollutant concentration, pH, and reaction time.

Bibliography

1. Sang, L., Y. Zhao, and C. Burda, *TiO_2 nanoparticles as functional building blocks.* Chemical reviews, 2014. **114**(19): p. 9283-9318.
2. Asahi, R., et al., *Nitrogen-doped titanium dioxide as visible-light-sensitive photocatalyst: designs, developments, and prospects.* Chemical reviews, 2014. **114**(19): p. 9824-52.
3. Schneider, J., et al., *Understanding TiO_2 photocatalysis: mechanisms and materials.* Chemical reviews, 2014. **114**(19): p. 9919-9986.
4. Pelaez, M., et al., *A review on the visible light active titanium dioxide photocatalysts for environmental applications.* Applied Catalysis, B: Environmental, 2012. **125**: p. 331-349.
5. Chong, M.N., et al., *Recent developments in photocatalytic water treatment technology: a review.* Water Research, 2010. **44**(10): p. 2997-3027.
6. Izumi, Y., *Recent advances in the photocatalytic conversion of carbon dioxide to fuels with water and/or hydrogen using solar energy and beyond.* Coordination Chemistry Reviews, 2013. **257**(1): p. 171-186.
7. Ma, Y., et al., *Titanium dioxide-based nanomaterials for photocatalytic fuel generations.* Chemical reviews, 2014. **114**(19): p. 9987-10043.
8. Rengifo-Herrera, J.A. and C. Pulgarin, *Photocatalytic activity of N, S co-doped and N-doped commercial anatase TiO_2 powders towards phenol oxidation and E. coli inactivation under simulated solar light irradiation.* Solar Energy, 2010. **84**(1): p. 37-43.
9. Blanco-Galvez, J., P. Fernandez-Ibanez, and S. Malato-Rodriguez, *Solar photocatalytic detoxification and disinfection of water: Recent overview.* Journal of Solar Energy Engineering-Transactions of the Asme, 2007. **129**(1): p. 4-15.
10. Paz, Y. and A. Heller, *Photo-oxidatively self-cleaning transparent titanium dioxide films on soda lime glass: The deleterious effect of sodium contamination and its prevention.* Journal of Materials Research, 2011. **12**(10): p. 2759-2766.
11. Xin-Tong Zhang, et al., *Self-Cleaning Particle Coating with Antireflection Properties.* Chemistry of Materials, 2005.
12. Liu, K., et al., *Bio-inspired titanium dioxide materials with special wettability and their applications.* Chemical reviews, 2014. **114**(19): p. 10044-10094.
13. Fujishima, A., T.N. Rao, and D.A. Tryk, *Titanium dioxide photocatalysis.* 2000. **1**: p. 1-21.
14. Cargnello, M., T.R. Gordon, and C.B. Murray, *Solution-phase synthesis of titanium dioxide nanoparticles and nanocrystals.* Chemical reviews, 2014. **114**(19): p. 9319-9345.

15. Armstrong, A.R., et al., *TiO_2-B nanowires.* Angewandte Chemie International Edition in English, 2004. **43**(17): p. 2286-8.

16. Pottier, A., et al., *Synthesis of brookite TiO_2 nanoparticles by thermolysis of $TiCl_4$ in strongly acidic aqueous media.* Journal of Materials Chemistry, 2001. **11**(4): p. 1116-1121.

17. Gupta, S. and M. Tripathi, *A review of TiO_2 nanoparticles.* Chinese Science Bulletin, 2011. **56**(16): p. 1639-1657.

18. Luttrell, T., et al., *Why is anatase a better photocatalyst than rutile?-Model studies on epitaxial TiO_2 films.* Sci Rep, 2014. **4**: p. 4043.

19. Luttrell, T., et al., *Why is anatase a better photocatalyst than rutile?--Model studies on epitaxial TiO2 films.* Sci Rep, 2014. **4**: p. 4043.

20. Bai, Y., et al., *Titanium Dioxide Nanomaterials for Photovoltaic Applications.* Chemical reviews, 2014.

21. Liu, G., et al., *Titanium dioxide crystals with tailored facets.* Chemical reviews, 2014. **114**(19): p. 9559-612.

22. Akpan, U.G. and B.H. Hameed, *The advancements in sol-gel method of doped-TiO_2 photocatalysts.* Applied Catalysis a-General, 2010. **375**(1): p. 1-11.

23. Macwan, D.P., P.N. Dave, and S. Chaturvedi, *A review on nano-TiO_2 sol-gel type syntheses and its applications.* Journal of Materials Science, 2011. **46**(11): p. 3669-3686.

24. Cihlar, J., E. Bartonickova, and J. Cihlar, *Low-temperature sol-gel synthesis of anatase nanoparticles modified by Au, Pd and Pt and activity of TiO_2/Au, Pd, Pt photocatalysts in water splitting.* Journal of Sol-Gel Science and Technology, 2013. **65**(3): p. 430-442.

25. Wang, C.C. and J.Y. Ying, *Sol-gel synthesis and hydrothermal processing of anatase and rutile titania nanocrystals.* Chemistry of Materials, 1999. **11**(11): p. 3113-3120.

26. Asahi, R., et al., *Visible-light photocatalysis in nitrogen-doped titanium oxides.* Science, 2001. **293**(5528): p. 269-71.

27. Livraghi, S., et al., *Origin of photoactivity of nitrogen-doped titanium dioxide under visible light.* J Am Chem Soc, 2006. **128**(49): p. 15666-71.

28. Junwei Wang, et al., *An Efficient Two-Step Technique for Nitrogen-Doped Titanium Dioxide Synthesizing: Visible-Light-Induced Photodecomposition of Methylene Blue.* The Journal of Physical Chemistry C, 2006: p. 1010-1014.

29. Jagadale, T.C., et al., *N-doped TiO_2 nanoparticle based visible light photocatalyst by modified peroxide sol-gel method.* The Journal of Physical Chemistry C, 2008. **112**(37): p. 14595-14602.

30. Chemseddine, A. and T. Moritz, *Nanostructuring titania: Control over nanocrystal structure, size, shape, and organization.* European Journal of Inorganic Chemistry, 1999. **1999**(2): p. 235-245.

31. Liu, S., J. Yu, and M. Jaroniec, *Anatase TiO_2 with Dominant High-Energy {001} Facets: Synthesis, Properties, and Applications.* Chemistry of Materials, 2011. **23**(18): p. 4085-4093.

32. Yang, H.G., et al., *Solvothermal synthesis and photoreactivity of anatase TiO_2 nanosheets with dominant {001} facets.* J Am Chem Soc, 2009. **131**(11): p. 4078-4083.

33. Wang, D.H., et al., *One-step hydrothermal synthesis of N-doped TiO_2/C nanocomposites with high visible light photocatalytic activity.* Nanoscale, 2012. **4**(2): p. 576-84.

34. Hu, S.Z., et al., *Hydrothermal synthesis of well-dispersed ultrafine N-doped TiO_2 nanoparticles with enhanced photocatalytic activity under visible light.* Journal of Physics and Chemistry of Solids, 2010. **71**(3): p. 156-162.

35. Dinh, C.T., et al., *Shape-controlled synthesis of highly crystalline titania nanocrystals.* ACS nano, 2009. **3**(11): p. 3737-3743.

36. Asahi, R. and T. Morikawa, *Nitrogen complex species and its chemical nature in TiO_2 for visible-light sensitized photocatalysis.* Chemical Physics, 2007. **339**(1-3): p. 57-63.

37. Wang, X., et al., *One-dimensional titanium dioxide nanomaterials: nanowires, nanorods, and nanobelts.* Chemical reviews, 2014. **114**(19): p. 9346-9384.

38. Nakata, K. and A. Fujishima, *TiO_2 photocatalysis: Design and applications.* Journal of Photochemistry and Photobiology C: Photochemistry Reviews, 2012. **13**(3): p. 169-189.

39. Linsebigler, A.L., G.Q. Lu, and J.T. Yates, *Photocatalysis on Tio_2 Surfaces - Principles, Mechanisms, and Selected Results.* Chemical reviews, 1995. **95**(3): p. 735-758.

40. Fujishima, A., X.T. Zhang, and D.A. Tryk, *TiO_2 photocatalysis and related surface phenomena.* Surface Science Reports, 2008. **63**(12): p. 515-582.

41. Carp, O., C.L. Huisman, and A. Reller, *Photoinduced reactivity of titanium dioxide.* Progress in Solid State Chemistry, 2004. **32**(1-2): p. 33-177.

42. Pelizzetti, E. and C. Minero, *Mechanism of the photo-oxidative degradation of organic pollutants over TiO_2 particles.* Electrochimica Acta, 1993. **38**(1): p. 47-55.

43. Khataee, A.R. and M.B. Kasiri, *Photocatalytic degradation of organic dyes in the presence of nanostructured titanium dioxide: Influence of the chemical structure of dyes.* Journal of Molecular Catalysis A: Chemical, 2010. **328**(1-2): p. 8-26.

44. Yu, L., et al., *The degradation mechanism of methyl orange under photo-catalysis of TiO_2.* Physical Chemistry Chemical Physics, 2012. **14**(10): p. 3589-3595.

45. Guo, Z., R. Ma, and G. Li, *Degradation of phenol by nanomaterial TiO_2 in wastewater.* Chemical Engineering Journal, 2006. **119**(1): p. 55-59.

46. Adán, C., et al., *Structure and activity of nanosized iron-doped anatase TiO_2 catalysts for phenol photocatalytic degradation.* Applied Catalysis B: Environmental, 2007. **72**(1-2): p. 11-17.

47. Lachheb, H., et al., *Photocatalytic degradation of various types of dyes (Alizarin S, Crocein Orange G, Methyl Red, Congo Red, Methylene Blue) in water by UV-irradiated titania.* Applied Catalysis B: Environmental, 2002. **39**(1): p. 75-90.

48. Rashed, M.N. and A.A. El-Amin, *Photocatalytic degradation of methyl orange in aqueous TiO_2 under different solar irradiation sources.* International Journal of Physical Sciences, 2007. **2**(3): p. 73-81.

49. Yang, H.M., et al., *Sol-gel synthesis of TiO_2 nanoparticles and photocatalytic degradation of methyl orange in aqueous TiO_2 suspensions.* Journal of Alloys and Compounds, 2006. **413**(1-2): p. 302-306.

50. Yang, G., et al., *Preparation of highly visible-light active N-doped TiO_2 photocatalyst.* Journal of Materials Chemistry, 2010. **20**(25): p. 5301.

51. Legrini, O., E. Oliveros, and A.M. Braun, *Photochemical processes for water treatment.* Chemical reviews, 1993. **93**(2): p. 671-698.

52. Vorosmarty, C.J., et al., *Global threats to human water security and river biodiversity.* Nature, 2010. **467**(7315): p. 555-61.

53. Bahnemann, D., *Photocatalytic water treatment: solar energy applications.* Solar Energy, 2004. **77**(5): p. 445-459.

54. Malato, S., et al., *Decontamination and disinfection of water by solar photocatalysis: Recent overview and trends.* Catalysis Today, 2009. **147**(1): p. 1-59.

55. Lee, S.-Y. and S.-J. Park, *TiO_2 photocatalyst for water treatment applications.* Journal of Industrial and Engineering Chemistry, 2013. **19**(6): p. 1761-1769.

56. Prairie, M.R., et al., *An investigation of titanium dioxide photocatalysis for the treatment of water contaminated with metals and organic chemicals.* Environmental Science & Technology, 1993. **27**(9): p. 1776-1782.

57. Li, Z., S. Cong, and Y. Xu, *Brookite vs Anatase TiO_2 in the Photocatalytic Activity for Organic Degradation in Water.* Acs Catalysis, 2014. **4**(9): p. 3273-3280.

58. Shiraishi, Y., et al., *Rutile Crystallites Isolated from Degussa (Evonik) P25 TiO_2: Highly Efficient Photocatalyst for Chemoselective Hydrogenation of Nitroaromatics.* Acs Catalysis, 2013. **3**(10): p. 2318-2326.

59. Ahmed, A.Y., et al., *Photocatalytic Activities of Different Well-defined Single Crystal TiO_2 Surfaces: Anatase versus Rutile.* The Journal of Physical Chemistry Letters, 2011. **2**(19): p. 2461-2465.

60. Liu, L., et al., *Photocatalytic CO_2 Reduction with H_2O on TiO_2 Nanocrystals: Comparison of Anatase, Rutile, and Brookite Polymorphs and Exploration of Surface Chemistry.* Acs Catalysis, 2012. **2**(8): p. 1817-1828.

61. Liu, L., et al., *Engineering Coexposed {001} and {101} Facets in Oxygen-Deficient TiO_2 Nanocrystals for Enhanced CO_2 Photoreduction under Visible Light.* Acs Catalysis, 2016. **6**(2): p. 1097-1108.

62. Yaghoubi, H., et al., *Toward a Visible Light-Driven Photocatalyst: The Effect of Midgap-States-Induced Energy Gap of Undoped TiO_2 Nanoparticles.* Acs Catalysis, 2015. **5**(1): p. 327-335.

63. Park, J.H., S. Kim, and A.J. Bard, *Novel carbon-doped TiO_2 nanotube arrays with high aspect ratios for efficient solar water splitting.* Nano Lett, 2006. **6**(1): p. 24-28.

64. Li, D., et al., *Visible-light-driven photocatalysis on fluorine-doped TiO_2 powders by the creation of surface oxygen vacancies.* Chemical Physics Letters, 2005. **401**(4-6): p. 579-584.

65. Han, C., et al., *Innovative visible light-activated sulfur doped TiO_2 films for water treatment.* Applied Catalysis, B: Environmental, 2011. **107**(1-2): p. 77-87.

66. Liu, S. and X. Chen, *A visible light response TiO_2 photocatalyst realized by cationic S-doping and its application for phenol degradation.* J Hazard Mater, 2008. **152**(1): p. 48-55.

67. Subramanian, M., et al., *Effect of cobalt doping on the structural and optical properties of TiO_2 films prepared by sol–gel process.* Thin Solid Films, 2008. **516**(12): p. 3776-3782.

68. Ghicov, A., et al., *Photoresponse in the visible range from Cr doped TiO_2 nanotubes.* Chemical Physics Letters, 2007. **433**(4-6): p. 323-326.

69. Li, Y.-F., et al., *Mechanistic Study of Codoped Titania with Nonmetal and Metal Ions: A Case of C + Mo Codoped TiO_2.* Acs Catalysis, 2012. **2**(3): p. 391-398.

70. Gu, D.-E., B.-C. Yang, and Y.-D. Hu, *V and N co-doped nanocrystal anatase TiO_2 photocatalysts with enhanced photocatalytic activity under visible light irradiation.* Catalysis Communications, 2008. **9**(6): p. 1472-1476.

71. Nah, Y.C., I. Paramasivam, and P. Schmuki, *Doped TiO_2 and TiO_2 nanotubes: synthesis and applications.* Chemphyschem, 2010. **11**(13): p. 2698-713.

72. Serpone, N., *Is the band gap of pristine TiO_2 narrowed by anion- and cation-doping of titanium dioxide in second-generation photocatalysts?* The Journal of Physical Chemistry B, 2006. **110**(48): p. 24287-93.

73. Wang, J., et al., *Origin of photocatalytic activity of nitrogen-doped TiO_2 nanobelts.* J Am Chem Soc, 2009. **131**(34): p. 12290-7.

74. Verbruggen, S.W., *TiO_2 photocatalysis for the degradation of pollutants in gas phase: From morphological design to plasmonic enhancement.* Journal of

Photochemistry and Photobiology C: Photochemistry Reviews, 2015. **24**: p. 64-82.

75. Sathish, M., et al., *Synthesis, Characterization, Electronic Structure, and Photocatalytic Activity of Nitrogen-Doped TiO_2 Nanocatalyst.* Chemistry of Materials, 2005. **17**(25): p. 6349-6353.

76. Wilke, K. and H.D. Breuer, *The influence of transition metal doping on the physical and photocatalytic properties of titania.* Journal of Photochemistry and Photobiology A: Chemistry, 1999. **121**(1): p. 49-53.

77. Akpan, U.G. and B.H. Hameed, *The advancements in sol-gel method of doped-TiO_2 photocatalysts.* Applied Catalysis A: General, 2010. **375**(1): p. 1-11.

78. Crişan, M., et al., *The effects of Fe, Co and Ni dopants on TiO_2 structure of sol–gel nanopowders used as photocatalysts for environmental protection: A comparative study.* Ceramics International, 2016. **42**(2): p. 3088-3095.

79. Xie, Y., et al., *Low temperature preparation and characterization of N-doped and N-S-codoped TiO_2 by sol-gel route.* Catalysis Letters, 2007. **118**(3-4): p. 231-237.

80. Wu, D., et al., *Low temperature hydrothermal synthesis of N-doped TiO_2 photocatalyst with high visible-light activity.* Journal of Alloys and Compounds, 2010. **502**(2): p. 289-294.

81. Jiang, Z., et al., *Solvothermal synthesis of N-doped TiO_2 nanotubes for visible-light-responsive photocatalysis.* Chem Commun (Camb), 2008(47): p. 6372-4.

82. Zhang, Y.C., et al., *HNO_3-involved one-step low temperature solvothermal synthesis of N-doped TiO_2 nanocrystals for efficient photocatalytic reduction of Cr(VI) in water.* Applied Catalysis B: Environmental, 2013. **142-143**: p. 249-258.

83. Wang, Q., et al., *Synthesis of N-doped TiO_2 mesosponge by solvothermal transformation of anodic TiO_2 nanotubes and enhanced photoelectrochemical performance.* Electrochimica Acta, 2012. **62**: p. 158-162.

84. Rattanakam, R. and S. Supothina, *Visible-light-sensitive N-doped TiO_2 photocatalysts prepared by a mechanochemical method: effect of a nitrogen source.* Research on Chemical Intermediates, 2009. **35**(3): p. 263-269.

85. Kim, S.J., et al., *Intrinsic Nitrogen-doped CVD-grown TiO_2 Thin Films from All-N-coordinated Ti Precursors for Photoelectrochemical Applications.* Chemical Vapor Deposition Banner, 2013. **19**(1-3): p. 45-52.

86. Di Valentin, C., G. Pacchioni, and A. Selloni, *Origin of the different photoactivity of N-doped anatase and rutileTiO_2.* Physical Review B, 2004. **70**(8).

87. Ananpattarachai, J., P. Kajitvichyanukul, and S. Seraphin, *Visible light absorption ability and photocatalytic oxidation activity of various interstitial N-doped TiO_2 prepared from different nitrogen dopants.* J Hazard Mater, 2009. **168**(1): p. 253-61.

88. Di Valentin, C., et al., *N-doped TiO_2: Theory and experiment.* Chemical Physics, 2007. **339**(1-3): p. 44-56.

89. Di Valentin, C., et al., *Characterization of paramagnetic species in N-doped TiO_2 powders by EPR spectroscopy and DFT calculations.* The Journal of Physical Chemistry B, 2005. **109**(23): p. 11414-9.

90. Balcerski, W., S.Y. Ryu, and M.R. Hoffmann, *Visible-Light Photoactivity of Nitrogen-Doped TiO_2: Photo-oxidation of HCO_2H to CO_2 and H_2O.* The Journal of Physical Chemistry C, 2007. **111**(42): p. 15357-15362.

91. Parida, K.M. and B. Naik, *Synthesis of mesoporous $TiO_{(2-x)}N_{(x)}$ spheres by template free homogeneous co-precipitation method and their photo-catalytic activity under visible light illumination.* Journal of Colloid and Interface Science, 2009. **333**(1): p. 269-76.

92. Xu, S., et al., *Preparations and photocatalytic properties of magnetically separable nitrogen-doped TiO_2 supported on nickel ferrite.* Applied Catalysis B: Environmental, 2007. **71**(3-4): p. 177-184.

93. Cong, Y., et al., *Synthesis and Characterization of Nitrogen-Doped TiO_2 Nanophotocatalyst with High Visible Light Activity.* The Journal of Physical Chemistry C, 2007. **111**(19): p. 6976-6982.

94. Liu, S., J. Yu, and W. Wang, *Effects of annealing on the microstructures and photoactivity of fluorinated N-doped TiO_2.* Physical Chemistry Chemical Physics, 2010. **12**(38): p. 12308-15.

95. Spadavecchia, F., et al., *Time effects on the stability of the induced defects in TiO_2 nanoparticles doped by different nitrogen sources.* Journal of Nanoparticle Research, 2012. **14**(12).

96. Yamada, K., et al., *Effect of thermal treatment on photocatalytic activity of N-doped TiO_2 particles under visible light.* Thin Solid Films, 2008. **516**(21): p. 7482-7487.

97. Zhao, Y., X. Qiu, and C. Burda, *The Effects of Sintering on the Photocatalytic Activity of N-Doped TiO_2 Nanoparticles.* Chemistry of Materials, 2008. **20**(8): p. 2629-2636.

98. Lo Presti, L., et al., *Role of the Nitrogen Source in Determining Structure and Morphology of N-Doped Nanocrystalline TiO_2.* The Journal of Physical Chemistry C, 2014. **118**(9): p. 4797-4807.

99. Bolton, J.R., et al., *Figures-of-Merit for the Technical Development and Application of Advanced Oxidation Processes.* Journal of Advanced Oxidation Technologies, 1996. **1**(1).

100. Ni, M., et al., *A review and recent developments in photocatalytic water-splitting using TiO_2 for hydrogen production.* Renewable & Sustainable Energy Reviews, 2007. **11**(3): p. 401-425.

101. Fujishima, A., T.N. Rao, and D.A. Tryk, *Titanium dioxide photocatalysis.* Journal of Photochemistry and Photobiology C: Photochemistry Reviews, 2000. **1**(1): p. 1-21.

102. Zaleska, A., *Doped-TiO_2: A Review.* Recent Patents on Engineering, 2008. **2**(3): p. 157-164.

103. Lee, K., A. Mazare, and P. Schmuki, *One-dimensional titanium dioxide nanomaterials: nanotubes.* Chemical reviews, 2014. **114**(19): p. 9385-454.

104. Gombac, V., et al., *TiO_2 nanopowders doped with boron and nitrogen for photocatalytic applications.* Chemical Physics, 2007. **339**(1-3): p. 111-123.

105. Wu, Y., et al., *Enhanced Photocatalytic Activity of Nitrogen-Doped Titania by Deposited with Gold.* The Journal of Physical Chemistry C, 2009. **113**(33): p. 14689-14695.

106. Liu, C., et al., *Characterization and activity of visible-light-driven TiO_2 photocatalyst codoped with nitrogen and cerium.* Journal of Solid State Chemistry, 2008. **181**(4): p. 913-919.

107. Yang, J., et al., *IR and XPS investigation of visible-light photocatalysis—Nitrogen–carbon-doped TiO_2 film.* Applied Surface Science, 2006. **253**(4): p. 1988-1994.

108. Wei, H., et al., *Preparation and photocatalysis of TiO_2 nanoparticles co-doped with nitrogen and lanthanum.* Journal of Materials Science, 2004. **39**(4): p. 1305-1308.

109. Xie, Y., Y. Li, and X. Zhao, *Low-temperature preparation and visible-light-induced catalytic activity of anatase F–N-codoped TiO_2.* Journal of Molecular Catalysis A: Chemical, 2007. **277**(1-2): p. 119-126.

110. Joshi, M.M., et al., *Visible light induced photoreduction of methyl orange by N-doped mesoporous titania.* Applied Catalysis A: General, 2009. **357**(1): p. 26-33.

111. Wang, Y., et al., *Catalytic activity of mesoporous $TiO_{2-x}N_x$ photocatalysts for the decomposition of methyl orange under solar simulated light.* Catalysis Communications, 2009. **10**(4): p. 412-415.

112. Kontos, A.I., et al., *Nitrogen modified nanostructured titania: electronic, structural and visible-light photocatalytic properties.* Physica Status Solidi RRL: Rapid Research Letters, 2008. **2**(2): p. 83-85.

113. Liu, J., et al., *Solvothermal-induced phase transition and visible photocatalytic activity of nitrogen-doped titania.* J Hazard Mater, 2009. **163**(1): p. 273-8.

114. Khalid, N.R., et al., *Nitrogen doped TiO_2 nanoparticles decorated on graphene sheets for photocatalysis applications.* Current Applied Physics, 2012. **12**(6): p. 1485-1492.

115. Zhou, X., et al., *Effect of nitrogen-doping temperature on the structure and photocatalytic activity of the B,N-doped TiO_2.* Journal of Solid State Chemistry, 2011. **184**(1): p. 134-140.

116. Qin, H.-L., G.-B. Gu, and S. Liu, *Preparation of nitrogen-doped titania with visible-light activity and its application.* Comptes Rendus Chimie, 2008. **11**(1-2): p. 95-100.

117. Zhou, X., et al., *Preparation of nitrogen doped TiO_2 photocatalyst by oxidation of titanium nitride with H_2O_2.* Materials Research Bulletin, 2011. **46**(6): p. 840-844.

118. Shen, X.-Z., et al., *Visible-light-driven titania photocatalyst co-doped with nitrogen and ferrum.* Applied Surface Science, 2008. **254**(15): p. 4726-4731.

119. Shirley, D.A., *High-Resolution X-Ray Photoemission Spectrum of the Valence Bands of Gold.* Physical Review B, 1972. **5**(12): p. 4709-4714.

120. Brunauer, S., P.H. Emmett, and E. Teller, *Adsorption of Gases in Multimolecular Layers.* J Am Chem Soc, 1938. **60**(2): p. 309-319.

121. Borchert, H., et al., *Determination of nanocrystal sizes: a comparison of TEM, SAXS, and XRD studies of highly monodisperse $CoPt_3$ particles.* Langmuir, 2005. **21**(5): p. 1931-6.

122. Bu, X., G. Zhang, and C. Zhang, *Effect of nitrogen doping on anatase–rutile phase transformation of TiO_2.* Applied Surface Science, 2012. **258**(20): p. 7997-8001.

123. Peng, F., et al., *Preparation of nitrogen-doped titanium dioxide with visible-light photocatalytic activity using a facile hydrothermal method.* Journal of Physics and Chemistry of Solids, 2008. **69**(7): p. 1657-1664.

124. Michalow, K.A., et al., *Synthesis, characterization and electronic structure of nitrogen-doped TiO_2 nanopowder.* Catalysis Today, 2009. **144**(1-2): p. 7-12.

125. Komornicki, S., M. Radecka, and R. Sobas, *Structural, electrical and optical properties of TiO_2-WO_3 polycrystalline ceramics.* Materials Research Bulletin, 2004. **39**(13): p. 2007-2017.

126. Tauc, J., *Absorption Edge and Internal Electric Fields in Amorphous Semiconductors.* Materials Research Bulletin, 1970. **5**(8): p. 721-+.

127. Huang, J.Y., et al., *Robust superhydrophobic TiO_2 fabrics for UV shielding, self-cleaning and oil–water separation.* Journal of Materials Chemistry A, 2015. **3**(6): p. 2825-2832.

128. Pelaez, M., et al., *A review on the visible light active titanium dioxide photocatalysts for environmental applications.* Applied Catalysis B: Environmental, 2012. **125**: p. 331-349.

129. Dong, W., et al., *A performance study of enhanced visible-light-driven photocatalysis and magnetical protein separation of multifunctional yolk–shell nanostructures.* Journal of Materials Chemistry A, 2013. **1**(34): p. 10030.

130. Yu, J., et al., *Enhanced photocatalytic CO_2-reduction activity of anatase TiO_2 by coexposed {001} and {101} facets.* J Am Chem Soc, 2014. **136**(25): p. 8839-42.

131. Wang, C., et al., *Enhancing visible-light photoelectrochemical water splitting through transition-metal doped TiO_2 nanorod arrays.* Journal of Materials Chemistry A, 2014. **2**(42): p. 17820-17827.

132. Bi, Z., et al., *High performance Cr, N-codoped mesoporous TiO_2 microspheres for lithium-ion batteries.* Journal of Materials Chemistry A, 2014. **2**(6): p. 1818-1824.

133. Patel, N., et al., *Efficient photocatalytic degradation of organic water pollutants using V–N-codoped TiO_2 thin films.* Applied Catalysis B: Environmental, 2014. **150-151**: p. 74-81.

134. Ge, M., et al., *A review of one-dimensional TiO_2 nanostructured materials for environmental and energy applications.* Journal of Materials Chemistry A, 2016. **4**(18): p. 6772-6801.

135. Park, J.H., S. Kim, and A.J. Bard, *Novel carbon-doped TiO_2 nanotube arrays with high aspect ratios for efficient solar water splitting.* Nano Lett, 2006. **6**(1): p. 24-8.

136. Fang, W.Q., et al., *Fluorine-doped porous single-crystal rutile TiO_2 nanorods for enhancing photoelectrochemical water splitting.* Chemistry a European Journal, 2014. **20**(36): p. 11439-44.

137. Park, J.T., et al., *Preparation of TiO_2 spheres with hierarchical pores via grafting polymerization and sol–gel process for dye-sensitized solar cells.* Journal of Materials Chemistry, 2010. **20**(39): p. 8521.

138. Wang, Y., et al., *Microwave-assisted hydrothermal synthesis of graphene based Au–TiO_2 photocatalysts for efficient visible-light hydrogen production.* Journal of Materials Chemistry A, 2014. **2**(11): p. 3847-3855.

139. Ke, G.-J., et al., *Template-free solvothermal fabrication of hierarchical TiO_2 hollow microspheres for efficient dye-sensitized solar cells.* Journal of Materials Chemistry A, 2013. **1**(42): p. 13274.

140. Kavan, L. and M. Grätzel, *Highly efficient semiconducting TiO_2 photoelectrodes prepared by aerosol pyrolysis.* Electrochimica Acta, 1995. **40**(5): p. 643-652.

141. Jiang, Z., et al., *Solvothermal synthesis of N-doped TiO_2 nanotubes for visible-light-responsive photocatalysis.* Chem Commun (Camb), 2008(47): p. 6372-6374.

142. Ye, L., et al., *Synthesis of anatase TiO_2 nanocrystals with {101}, {001} or {010} single facets of 90% level exposure and liquid-phase photocatalytic reduction and oxidation activity orders.* Journal of Materials Chemistry A, 2013. **1**(35): p. 10532.

143. Xiang, Q., K. Lv, and J. Yu, *Pivotal role of fluorine in enhanced photocatalytic activity of anatase TiO_2 nanosheets with dominant (001) facets for the photocatalytic degradation of acetone in air.* Applied Catalysis B: Environmental, 2010. **96**(3-4): p. 557-564.

144. Zhao, X.W., et al., *Shape- and Size-Controlled Synthesis of Uniform Anatase TiO_2 Nanocuboids Enclosed by Active {100} and {001} Facets.* Advanced Functional Materials, 2011. **21**(18): p. 3554-3563.

145. Nie, S., X. Zhao, and B. Liu, *A facile hydrothermal method for the controllable synthesis of TiO_2 nanocrystals with tunable shapes.* RSC Advances, 2015. **5**(125): p. 103386-103393.

146. Xu, H. and L. Zhang, *Controllable One-Pot Synthesis and Enhanced Photocatalytic Activity of Mixed-Phase TiO_2 Nanocrystals with Tunable Brookite/Rutile Ratios.* The Journal of Physical Chemistry C, 2009. **113**(5): p. 1785-1790.

147. Hidalgo, M.C., et al., *Hydrothermal preparation of highly photoactive TiO_2 nanoparticles.* Catalysis Today, 2007. **129**(1-2): p. 50-58.

148. Colón, G., et al., *Influence of amine template on the photoactivity of TiO_2 nanoparticles obtained by hydrothermal treatment.* Applied Catalysis B: Environmental, 2008. **78**(1-2): p. 176-182.

149. Robert, D., et al., *Photocatalytic detoxification with TiO_2 supported on glass-fibre by using artificial and natural light.* Catalysis Today, 1999. **54**(2-3): p. 291-296.

150. Kim, Y.K., et al., *Enhanced photoactivity of stable colloidal TiO_2 nanoparticles prepared in water by nanosecond infrared laser pulses.* Korean Journal of Chemical Engineering, 2017. **34**(6): p. 1822-1826.

151. Fernández-Ibáñez, P., et al., *Application of the colloidal stability of TiO_2 particles for recovery and reuse in solar photocatalysis.* Water Research, 2003. **37**(13): p. 3180-3188.

152. Xie, J., et al., *The role of surface modification for TiO_2 nanoparticles in cancer cells.* Colloids Surf B: Biointerfaces, 2016. **143**: p. 148-155.

153. Yadav, T., A.A. Mungray, and A.K. Mungray, *A comparative analysis of a TiO_2 nanoparticle dispersion in various biological extracts.* RSC Advances, 2015. **5**(79): p. 64421-64432.

154. Buchalska, M., et al., *New insight into singlet oxygen generation at surface modified nanocrystalline TiO_2--the effect of near-infrared irradiation.* Dalton Transactions, 2013. **42**(26): p. 9468-75.

155. Liao, D.L., G.S. Wu, and B.Q. Liao, *Zeta potential of shape-controlled TiO_2 nanoparticles with surfactants.* Colloids and Surfaces A: Physicochemical and Engineering Aspects, 2009. **348**(1-3): p. 270-275.

156. Molea, A., et al., *Influence of pH on the formulation of TiO_2 nano-crystalline powders with high photocatalytic activity.* Powder Technology, 2014. **253**: p. 22-28.

157. Sugimoto, T., X. Zhou, and A. Muramatsu, *Synthesis of uniform anatase TiO_2 nanoparticles by gel-sol method.* Journal of Colloid and Interface Science, 2003. **259**(1): p. 43-52.

158. Zeitler, V.A. and C.A. Brown, *The Infrared Spectra of Some Ti-O-Si, Ti-O-Ti and Si-O-Si Compounds.* The Journal of Physical Chemistry, 1957. **61**(9): p. 1174-1177.